Institute of Biomechanics
Center of Biomedical Engineering
Kronesgasse 5-I
8010 Graz, Austria

Master Thesis

Constitutive Modeling of the Biomechanical Properties of Human Ventricular Myocardium Incorporating its Ultrastructure

to achieve the degree of
Master of Science

Author: Christian W. Soboll, BSc
Supervisor: Gerhard Sommer, PhD
Head of Institute: Prof. Gerhard A. Holzapfel, PhD

September 20, 2014

Contents

List of Figures

List of Tables

Abstract

Objectives. The aim of this thesis is to accomplish data preparation and analysis of human myocardium by observation of triaxial simple shearing tests. Optimization of the underlying dataset is obligatory as well as parameter fitting for existent hyperelastic materials. In addition, further models referred to dispersion of fibers, viscoelasticity and softening shall be introduced and evaluated.

Methods. The investigated heart specimens have been mounted into a triaxial shear testing device performing a simple shear loading pattern at the Institute of Biomechanics as part of the Graz, University of Technology. After preparation of data including filtering, cycle separation and decoupling of elastic and viscous stresses existing hyperelastic models are used for parameter estimation concerning perfectly aligned fiber models and dispersed fiber models. Moreover, viscoelastic models based on derivatives of invariants are introduced and propose two viscoelastic effects, i.e. 'restructuring' and 'damping'. Finally, a softening model in terms of a strain-energy reduction function dependent on loading history is established.

Results. In total, 32 hearts have been investigated of which 37 excised specimens could be used for data evaluation. Data fits for hyperelastic models show that fibers and sheets are the main load carrying elements of the myocardium. Fiber and sheet stiffness decrease with first loading but nonlinearity tend to increase initially followed by rapid decrease at higher loading peaks. This may indicate perimysial fiber rupture. The proposed viscoelastic model is able to represent the periodic response only. The 'restructuring' effect is dominant at low loading peaks whereas 'damping' effects remain constantly unchanged. Thus, 'restructuring' may indicate sliding of sheets during cardiac muscle motion. Eventually, strong softening of fiber and sheet is observed for repeated loading patterns and relatively reduces with increasing loading peaks.

Conclusion. Decoupling of elastic and viscous stresses for separate data fitting is a new approach towards myocardial tissue modeling. Approximately, we can reproduce 99.82% of the dispersed elastic and 94.31% of the viscous experimental data including 95.6% of absolute softening at endstage loading. As low shear stresses are required in order to guarantee easy motion of adjacent sheet layers, the myocardial vitality may be interpreted in terms of low stiffness, high nonlinearity, low dispersion, high restructuring and constant damping with absence of geometrical abnormalities or biological defects.

Zusammenfassung

Ziele. Das Ziel dieser Arbeit besteht in der Datenaufbereitung und Analyse von menschlichen Herzmuskelgewebedaten, welche mittels Scherversuchen unter Zuhilfenahme einer triaxialen Schertestvorrichtung gewonnen werden. Die Optimierung der zugrunde liegenden Datensätze ist obligatorisch und für die Bestimmung zuverlässiger Parameter hyperelastischer Materialien notwendig. Darüber hinaus sollen weitere Modelle, welche die Dispersion von Fasern, Viskoelastizität und Erweichung des Gewebes beschreiben können, eingeführt und ausgewertet werden.

Methoden. Die Experimentdaten werden mittels einer dreiachsigen Schertestvorrichtung, welche seitens des Instituts für Biomechanik als Teil der Technischen Universität Graz zur Verfügung gestellt wird, gewonnen. Nach Aufbereitung der Daten einschließlich Filterung, Trennung der Zyklen und Entkopplung von elastischen und viskosen Spannungen, werden die bestehenden hyperelastischen Modelle - umfassend ein perfekt ausgerichtetes Fasermodell sowie ein gestreut ausgerichtetes Fasermodell - zur Parameterschätzung verwendet. Darüber hinaus sollen viskoelastische Modelle auf Basis von zeitlichen Ableitungen der Invarianten eingeführt werden, wobei "Umstrukturierung" und "Dämpfung" grundlegende Teile des Modells bilden. Schließlich wird ein Erweichungsmodell in Bezug auf die Reduktion der Verzerrungsenergie eingeführt und abhängig von der Belastungshistorie aufgebaut.

Ergebnisse. Insgesamt wurden 32 Herzen zur Verfügung gestellt, von denen 37 verwendbare Proben exzidiert und für die Datenauswertung verwendet wurden. Die dazugehörigen hyperelastischen Daten der Modelle zeigen, dass Fasern und Faserschichten die Haupttragelemente des Herzmuskels bilden. Faser- und Faserschichtensteifigkeit nehmen ab dem ersten Belastungszyklus monoton ab. Im Gegensatz dazu steigen die Faser- und Faserschichten-Nichtlinearitäten bei höheren Belastungsspitzen anfänglich, gefolgt von einem raschen Abfall. Dies deutet möglicherweise auf einen perimysialen Faserriss hin. Das vorgeschlagene viskoelastische Modell ist in der Lage, die eingeschwungene Belastungsantwort zu repräsentieren. Die "Umstrukturierung" dominiert bei niedrigen Belastungsspitzen, wohingegen die "Dämpfung" relativ unverändert auf die Belastungsspitzen reagiert. Die "Umstrukturierung" kann als relatives Gleiten aneinander liegender Faserschichten während der Herzmuskelbewegung interpretiert werden. Schließlich wird eine starke Erweichung der Fasern und Faserschichten für wiederholte Belastungsmuster beobachtet, welche in nachfolgenden Zyklen leicht abnimmt.

Schlussfolgerungen. Die Entkopplung von elastischen und viskosen Spannungen für die getrennte Modellierung und Parameterschätzung ist der zentrale Ansatz zur Modellierung. Die elastischen Daten konnten zu 99,82% und die viskosen Daten zu 94,31% bestimmt werden, wobei eine Erweichung von 95,6% im finalen Belastungszyklus festgestellt wurde. Um eine einfache Bewegung von benachbarten Faserschichten zu garantieren, sind geringe Schubspannungen erforderlich. Demnach kann die myokardiale Vitalität im Hinblick auf geringe Steifigkeit, hohe Nichtlinearität, niedrige Dispersion, hohe Restrukturierung und konstante Dämpfung mit der Abwesenheit von geometrischen Unregelmäßigkeiten oder biologischen Defekten verstanden werden.

Acknowledgment

A master thesis may be written as one but is always a result created by a team. Every discussion, all motivating words and encouragement has helped me finish this thesis. Therefore, i would like to say thank you very much for supporting me during this year of hard work.

First of all, I have to thank the Institute of Biomechanics as part of the Graz, University of Technology for the opportunity of writing this Master Thesis. Especially, the trust of Professor Gerhard A. Holzapfel is of great importance for me and deserves cordial thanks. The field of continuum mechanics and constitutive modeling is an extraordinary interesting topic which is tremendously researched at the Institute of Biomechanics. I am glad that I have been part of this fantastic office.

In addition, great acknowledgment goes to my advisor Mr. PhD Gerhard Sommer who has been very patient and has supported me throughout the whole process in an always friendly and wise manner. It has been a fantastic year working with you being a fantastic supporter and – which matters most – a friend.

Additionally, I would like to thank my parents for their mental support throughout the whole process. It has been a hard year for me and your way of motivation and ideas on problem solving has helped me to finish this thesis happily and satisfied.

Last but not least, I may also thank my lovely girlfriend Viviane. All the words you say and all the things you do make me a better person. You ask me the right questions, you say the important things and you see solutions which i cannot. Many times we talked about personality and identities. With you if find myself in a new position of finding myself. I once told you that i feel often alone in hard situations but now I see i am not. You have given me the necessary relaxing moments, the critical reflections and objective attitude to stay motivated and focused until finishing this thesis.

Seven years of studying is a long time. All persons i have met and all discussion that have taken place made me who i am today. A person who can happily say: I did it!

1. Introduction and Objective

1.1. Motivation

'The heart has its reasons which reason knows not' (Blaise Pascal)

Introduction. Truly, the heart is one of the most astonishing creations in nature. In humanoids it pumps blood through arteries and veins with speeds more than four liters per minute, contraction times being within hundreds of a second and creating pressures in the range of 16 kPa. Basically, its structure is a four chamber architecture with a special electrical conduction system. This system guarantees an ordered stimulation of the myocardium performing a wave like contraction of atria and ventricles.

In 2010, Eurostat as part of the European Commission [16] has published a report saying ischaemic heart diseases are the number one death causes in the EU-28 countries as shown in Fig. 1.1. Major causes of death referred to Austria are cardiovascular diseases followed by malignant growth which vary by sex as stated by the Statistik Austria in 2014 [2]. Figures 1.2(a) and 1.2(b) present the main causes of death for women and men, respectively. Thus, it is important to understand not only the mechanisms of disease development and propagation but also analyzing mechanisms during life for diseased hearts. Therefore, the field of biomechanics and constitutive modeling are useful tools for understanding the effects and downsides of cardiomyopathies and hypertrophies in the human heart.

By now, a series of histological, structural and physiological studies presented the composition and function of the heart including biaxial tensile tests [7, 12, 30, 51] on myocardial tissue. As reported by Holzapfel et al. [25],

'... data from biaxial tests alone are not enough to characterize the passive response of myocardium because such data suggest that the material is transversely isotropic'.

Therefore, the aim of this thesis is to extend existing models by analyzing data collected from triaxial simple shear tests being more informational than biaxial tensile tests as already stated by Truesdell et al. [58].
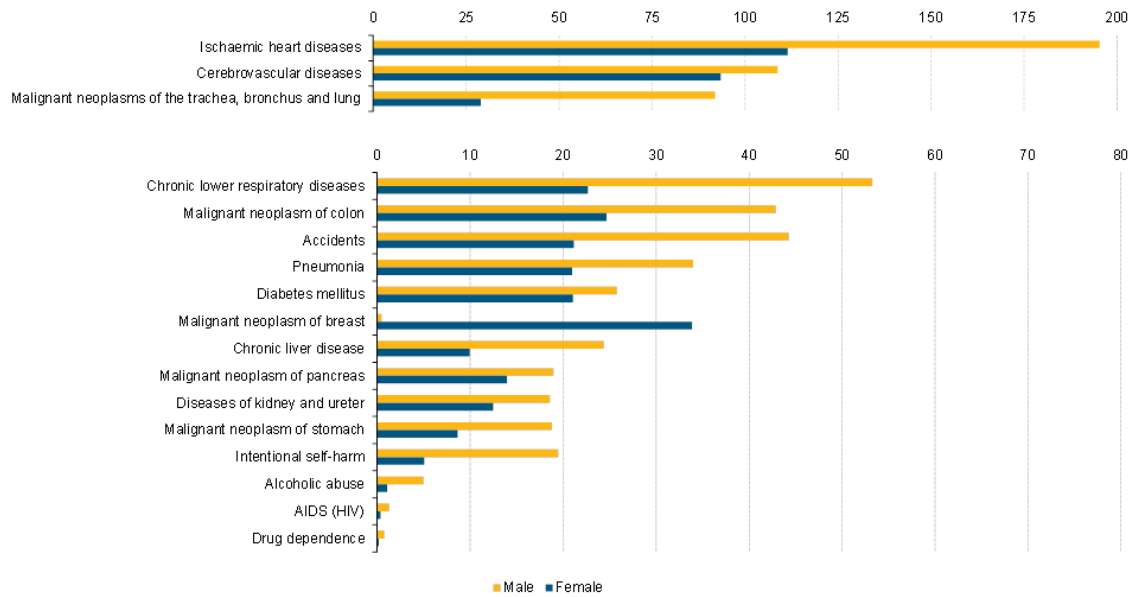
Figure 1.1.: Causes of death listed by standardized death rate per 100,000 inhabitants [16].

(a) Main causes of death for women in Austria.

(b) Main causes of death for men in Austria.
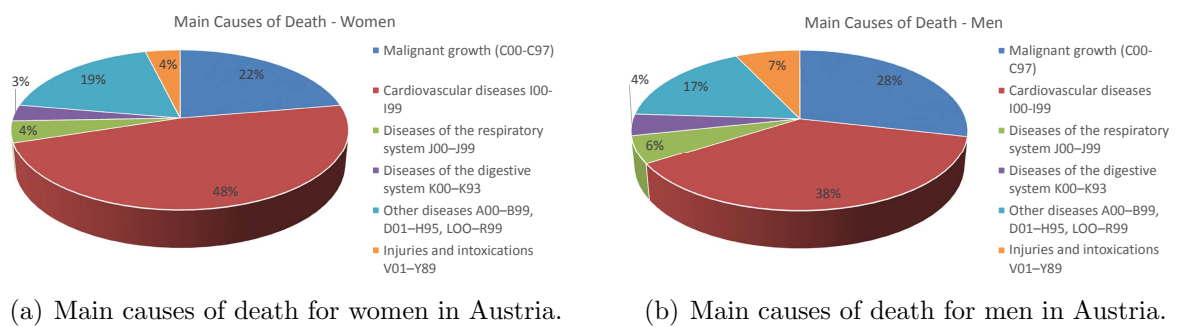
Figure 1.2.: Main causes of death per sex in Austria [2].

Objective. The objective of this master's thesis is

- the preparation of passive myocardial data for

- fitting existing hyperelastic models including

- extension of existing models considering dispersion and

- expansion of hyperelastic models with viscoelastic models.

1.2. Anatomy and Medical Background

The human heart consists of four chambers being the right atrium, right ventricle, left atrium and left ventricle. In order to guarantee controlled movement of blood a three layered muscle called myocardium is excited by the electrical conduction system consisting of the sino-atrial node, atrio-ventricular node, bundle of His, bundle branches and the Purkinje fibers. Thus, the heart more or less performs a torsional movement which ejects blood in a very efficient way. [33]

Within the focus of this thesis the left ventricle wall is made of endocardium, myocardium and epicardium. The wall is composed of a solid phase making up 20% of total volume and 80% of non-flowing fluid phase [43]. The solid phase is further separated into 70% myocytes in form of sarcomers containing three fiber types: actin, myosin and titin. The remaining portion of 30% are interstitial components, endomysial collagen type III (highly deformable) and perimysial collagen type I (high tensile strength) [46]. Fomovsky et al. [17] summarize the biomechanical importance of extracellular matrix (ECM) compounds and ascertain collagen, elastin and proteoglycans as the main load contributing elements of the ECM. Nevertheless, elastin rarely contributes to carry load within the myocardium [17]. Eventually, elastin fibers may be neglected in terms of biomechanical relevance within the scope of this thesis. In Figure 1.3 the myocyte structure is shown by Rohmer et al. [46]. Histological analysis have shown that orientation of fibers and their layered structures called sheets [27] vary from +60° to –60° through the ventricle wall [56] (see also Sec. 3.1 Fig. 3.2(a)). The mentioned sheets are approximately three to four cells thick and build a laminar structure which give the ventricle important mechanical properties [5, 27]. Recently, Ticar [57] has shown that the observed sheets seem to exceed the proposed number of cells per sheet from Rohmer et al. [46] by applying 3-D reconstruction techniques.

1.3. Mechanical Properties of Myocardium

Based on Sec. 1.2 some special biomechanical properties in ventricle wall mechanics are obvious. Due to the high water content it is said to be incompressible [59]. The complex formation of fibers, sheets and matrix components cause propagating stiffening linked with increasing loads showing nonlinear stress strain relations with strong directional
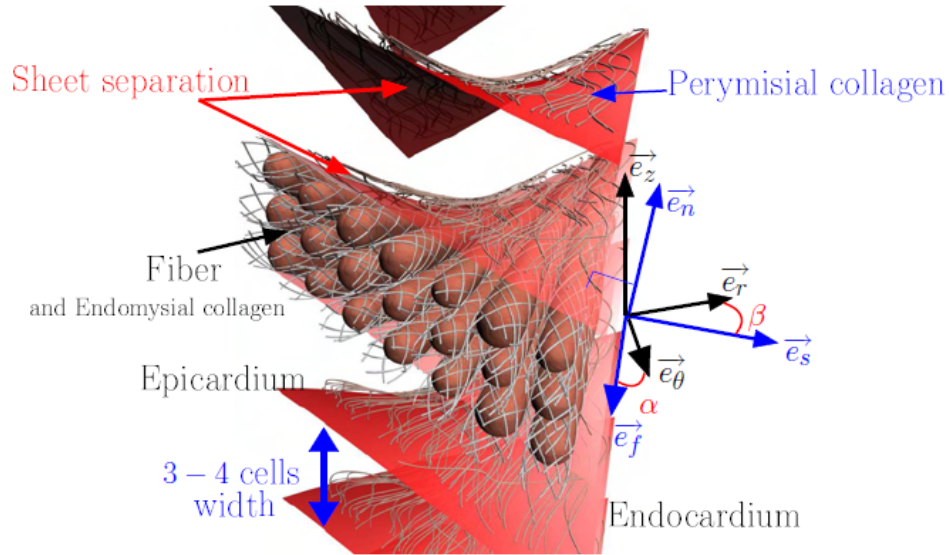
Figure 1.3.: Myocyte structure showing fibers, collagen fibers and layers of myocyte fibers organized in sheets (taken from Rohmer et al.[46]).

dependence represented by anisotropy. Furthermore, compositional differences lead to inhomogeneous material behavior.

Myocardial mechanics usually show following characteristics:

- anisotropy,
- inhomogeneity,
- non-linearity,
- quasi-incompressibility,
- multi-phasic,

    solid: myocytes, collagen, interstitial components,

    fluid: within cells,

    physicochemical: adenosine triphosphate (ATP), ions and ion-channels,

- active tissue behavior (not only when electrically stimulated).

Therefore, some simplifications for experimental setup and modeling are obligatory in terms of control and test redundancy. These are:

- transverse isotropy or orthotropy,
- layer-wise homogeneity,
- exponential behavior,
- incompressibility,
- monophasic,
- passive tissue.

2. Basics for Modeling

2.1. Continuum Mechanics

In the following section a short introduction into continuum mechanics is given based on the work of Holzapfel et al. [23].

2.1.1. Deformation Gradient and Invariants

In continuum mechanics, matter is assumed to be continuously distributed. Therefore, multiple phases can have coinciding positions. In order to describe the deformation of an arbitrary body with volume Ω and surface $\partial\Omega$ a tensor called deformation gradient $\mathbf{F}$ is introduced. Thus, we distinguish between the referential (undeformed) Ω_0 and current configuration (deformed) Ω with coordinates $\mathbf{X}(t)$ and $\mathbf{x}(\mathbf{X}, t)$, respectively. The deformation gradient is given via

$$\mathbf{F} = \mathrm{grad}(\mathbf{x}(\mathbf{X}, t)) \,. \tag{2.1}$$

In general, the deformation gradient is a non-symmetric second order tensor. For computational efficiency a symmetric deformation tensor called right Cauchy-Green tensor $\mathbf{C}$ is introduced. The symmetric tensor is given via

$$\mathbf{C} = \mathbf{F}^{\mathrm{T}}\mathbf{F} \,, \tag{2.2}$$

and is often used for modeling strain-energy functions. Regarding the scalar strain-energy function Ψ, it is necessary to find scalar quantities in order to represent the deformation gradient. Fortunately, the so-called invariants I_i are capable of describing the deformation. These invariants are independent of the selected coordinate system and, therefore, called principal scalar invariants. For a given deformation gradient $\mathbf{F}$ the corresponding eigenvectors $\hat{\mathbf{n}}_i$ can be found through solving

$$\mathbf{F}\hat{\mathbf{n}}_i = \lambda_i \hat{\mathbf{n}}_i \,. \tag{2.3}$$

The resulting characteristic polynomial for $\mathbf{F}$ is given via

$$\det(\mathbf{F} - \lambda_i \mathbf{I}) = -\lambda_i^3 + I_1\lambda_i^2 - I_2\lambda_i + I_3 \,, \tag{2.4}$$

and thus their invariants are given by

$$I_1(\mathbf{F}) = \text{tr}(\mathbf{F})\,, \tag{2.5}$$

$$I_2(\mathbf{F}) = \frac{1}{2}\left(\text{tr}(\mathbf{F})^2 + \text{tr}(\mathbf{F}^2)\right)\,, \tag{2.6}$$

$$I_3(\mathbf{F}) = \det(\mathbf{F})\,. \tag{2.7}$$

I_3 is equal to the Jacobi-determinant $J = \det(\mathbf{F})$ which describes the relative change of volume. Thus, incompressible materials force the third invariant to be unity $I_3 = J = 1$.

2.1.2. Structural Components

In order to obtain the stress tensors we need a material law describing the relation of stress and strain. The deformation gradient $\mathbf{F}$ is actually a stretch tensor. The invariants I_1 and I_2 are used as quantities for isotropic deformation whereas I_3 is used for volumetric change descriptions. Furthermore, so called pseudo-invariants can be used to describe anisotropic behavior caused by fibers, sheets or other reinforcements. Within the scope of this thesis we focus on the fourth, sixth (same as fourth with second fiber family) and eighth pseudo-invariant as these are used for modeling fibers, sheets and couplings of myocardial tissue. They are given by the direction of fibers $\mathbf{f_0}$ and sheets $\mathbf{s_0}$ in the referential configuration Ω_0 as well as their corresponding stretch parameters λ_f and λ_s via

$$I_4 = \mathbf{f_0} \cdot \mathbf{C}\mathbf{f_0} = \mathbf{C} : (\mathbf{f_0} \otimes \mathbf{f_0}) = \mathbf{C} : \mathbf{F_0} = \lambda_f^2\,, \tag{2.8}$$

$$I_6 = \mathbf{s_0} \cdot \mathbf{C}\mathbf{s_0} = \mathbf{C} : (\mathbf{s_0} \otimes \mathbf{s_0}) = \mathbf{C} : \mathbf{S_0} = \lambda_s^2\,, \tag{2.9}$$

$$I_8 = \mathbf{f_0} \cdot \mathbf{C}\mathbf{s_0} = \mathbf{C} : (\mathbf{f_0} \otimes \mathbf{s_0}) = \lambda_f\lambda_s\,, \tag{2.10}$$

where $\mathbf{F}_0$ and $\mathbf{S}_0$ are the fiber and sheet second order tensors defined in Ω_0, respectively.

These invariants assume perfect fiber alignment. In general, fibers are dispersed which means that not all fibers have the same axis of alignment as can be seen in recent studies of the myocardium, e.g. see [15, 57].

2.1.3. Use of Strain-Energy Functions

Having defined the deformation in terms of the deformation gradient $\mathbf{F}$ and its scalar invariants I_i, we have to define the definitions of stress and strain. In engineering, stress is defined as the force per unit area. When a body is loaded with force the body will deform in some way. Thus, energy is stored in the volume which we assume to be continuous. The stored energy per unit reference volume is called Helmholtz free-energy and denoted as Ψ. The Helmholtz free-energy function can be defined to be a function of $\mathbf{F}$ and its scalar invariants and forms a scalar function $\Psi = \Psi(\mathbf{F}) = \Psi(I_1, I_2, I_3, I_4, I_6, I_8)$.

If we neglect the change of area for the body, we call this the nominal stress or first Piola-Kirchhoff stress tensor $\mathbf{P}$. The first Piola-Kirchhoff stress tensor is a quantity with

its force defined in the actual configuration Ω and its area defined in the referential configuration Ω_0. Thus, the first Piola-Kirchhoff stress tensor is unsymmetrical and defined via

$$\mathbf{P} = \frac{\partial \Psi}{\partial \mathbf{F}} = \sum_i \frac{\partial \Psi}{\partial I_i} \frac{\partial I_i}{\mathbf{F}} \,. \tag{2.11}$$

Finally, the true stress tensor also called Cauchy stress tensor $\boldsymbol{\sigma}$ describes the actual stress referred to the actual surface in Ω. Using Eq. (2.11) and Nanson's formula the Cauchy stress is obtained through

$$\boldsymbol{\sigma} = J^{-1} \mathbf{P} \mathbf{F}^{\mathrm{T}} \,. \tag{2.12}$$

The strain-energy function Ψ can be composed by various energy functions as long as the laws of thermodynamics are fulfilled. The second law of thermodynamics states that energy can never be created and dissipation is either zero or positive. Neglecting thermal effects the internal dissipation is given by

$$D_{int} = \mathbf{P} : \dot{\mathbf{F}} - \dot{\Psi} \geq 0 \,. \tag{2.13}$$

If the internal dissipation is zero, the process is completely reversible without entropic effects. Hence, we find lossless Clausius-Planck equation

$$\dot{\Psi} = \mathbf{P} : \dot{\mathbf{F}} \,. \tag{2.14}$$

This relation will later be used for modeling viscoelasticity in Sec. 3.4.3 when dissipation becomes non-zero.

2.2. Parameter Fit via Objective Function Minimization

Usually, parameter fits are obtained by a given model function $\hat{y}$ with a certain number of model parameters c_i. Usually, the model function $\hat{\mathbf{y}} = f(\mathbf{c}, \mathbf{x})$ with $\mathbf{c}$ being the parameter vector with length n_p tries to reproduce the discrete experimental data $y_i[x_i]$ with n observations. After calculation of the squared error e^2 derivatives for all parameters are computed (see Eq. (2.15)). All these derivatives should yield zero in order to guarantee global or at least local error function minimum (see Eq. (2.16)). This is called minimization of least-squares.

$$e^2 = \sum_i \left(y_i[x_i] - \hat{y}(x_i) \right)^2 = ||\mathbf{y} - \hat{\mathbf{y}}||^2 \,. \tag{2.15}$$

$$\frac{\partial e^2}{\partial \mathbf{c}} \overset{!}{=} \mathbf{0} \,. \tag{2.16}$$

For nonlinear problems, Matlab$^{\circledR}$ provides integrated solvers like 'lsqcurvefit' and 'lsqnonlin'.

Unfortunately, in our experimental setup we have a series of pairwise observations which all underlie the same biomechanical framework given by the strain-energy function Ψ. Consequently, we have to use a different method for parameter estimation called 'objective function minimization'. A series of proposed models can be fitted at the same time even when different experiments are conducted as long as the underlying parameter set is identical. Thus, we create an objective function e_{obj}^2 for every experiment EXP via

$$e_{obj}^2 = \sum_{EXP} ||\mathbf{y}^{(EXP)} - \hat{\mathbf{y}}^{(EXP)}||^2 \,. \tag{2.17}$$

Based on our triaxial shear problem the objective function will have the special form given by

$$e_{obj}^2 = \sum_{EXP} \left|\left|\mathbf{e}_n^{(EXP)} \cdot \left(\boldsymbol{\sigma}^{(EXP)} - J^{-1}\mathbf{P}^{(EXP)}\mathbf{F}^{(EXP)\mathrm{T}}\right)\mathbf{e}_l^{(EXP)}\right|\right|^2 , \tag{2.18}$$

where $\mathbf{e}_n^{(EXP)}$ is the normal unity vector and $\mathbf{e}_l^{(EXP)}$ is the loading unity vector depending on the experiment. Finally, we utilize Matlab's® objective function minimization algorithm via 'fmincon' which is a constrained version of 'fminsearch'. The fundamental constraint is that all estimated parameters have to be greater or equal to zero, i.e. $\mathbf{c} \geq \mathbf{0}$.

In order to determine the 'goodness of fit' the adjusted coefficient of determination R^2 with the total sum of squares SST and total sum of residuals $SSR = e_{obj}^2$ is used which is given by

$$R^2 = \frac{n-1}{n-n_p-1}\frac{SSR}{SST} = \frac{n-1}{n-n_p-1}\frac{e_{obj}^2}{SST} \,, \tag{2.19}$$

with the total sum of squares

$$SST = \sum_{EXP} \left|\left|\mathbf{e}_n^{(EXP)} \cdot \left(\boldsymbol{\sigma}^{(EXP)} - \bar{\boldsymbol{\sigma}}^{(EXP)}\right)\mathbf{e}_l^{(EXP)}\right|\right|^2 \,. \tag{2.20}$$

3. Methods

3.1. Source of Data

Over the past couple of years, a group of persons including graduates and undergraduates have performed uniaxial, biaxial and latest triaxal tensile and shear tests including the set up of constitutive frameworks for different tissues, e.g. healthy and diseased arteries [26, 53], bones [19], cartilage [42] and hearts [14, 25]. The necessary infrastructure comprising laboratories, machines, tools and know-how is supplied by the Institute of Biomechanics at the Graz University of Technology, Austria.

The scope of this thesis lies in data analysis of triaxial shear tests of human myocardium with a device as shown in Fig. 3.1. Therefore, human myocardial tissue is excised from different locations reaching from base over equator to apex in longitudinal direction and from endocardium through myocardium to epicardium in radial direction as shown in Figs. 3.2(a) and 3.3. At these specific positions small tissue cubes with an average side length of 3 to 5mm are cut out of the myocardium. In general, the typical excision point is referred to be the left ventricular free wall (LVFW) (area '2' in Fig. 3.3(B)). If cutting is not possible due to lack of specimens or damaged wall tissues (see Kutschera [35]), it is excised from the left ventricular front wall (area '3' in Fig. 3.3(B)). Afterwards, these cubes are glued to the fixed platen of the triaxial shear testing device as shown in Fig. 3.4. The used cyanoacrylate adhesive glue (Loctite$^\circledR$: Super Kleber, Power Gel) is non-penetrating in order to prevent falsification of tissue strength, stiffness and non-linearity. In Fig. 3.4 the fixation points as well as application of load are shown. As the platens are not moved towards each other, the tissue is exposed to simple shear until reaching the shear peaks $\hat{\gamma} = 0, 0.1, .. 0.5$. Simple shear means that a combination of shear and extension is applied on the specimen causing fibers, sheets and the ground substance to be elongated. Actually, simple shear enables to build a great information basis for modeling tissue mechanics as it combines both shear and tensile stress (see Truesdell [58]).

There are six possible loading modes which are shown in Fig. 3.2(b). For better understanding, we introduce a local coordinate system with FSN-coordinates (see Fig. 3.2(a)). As the heart consists of fibers, layers of fibers called sheets and ground substance, we call the fiber direction F-coordinate, the sheet direction S-coordinate and the direction perpendicular to the fiber-sheet plane N-coordinate in the following sections with $f_0 - s_0 - n_0$ in Ω_0 and $f - s - n$ in Ω. Hence, in case of simple shearing with applying shear γ the first letter describes the direction of the mounting surface vector and the second letter the direction of applied load, e.g. FN-mode loading means that the fibers are oriented
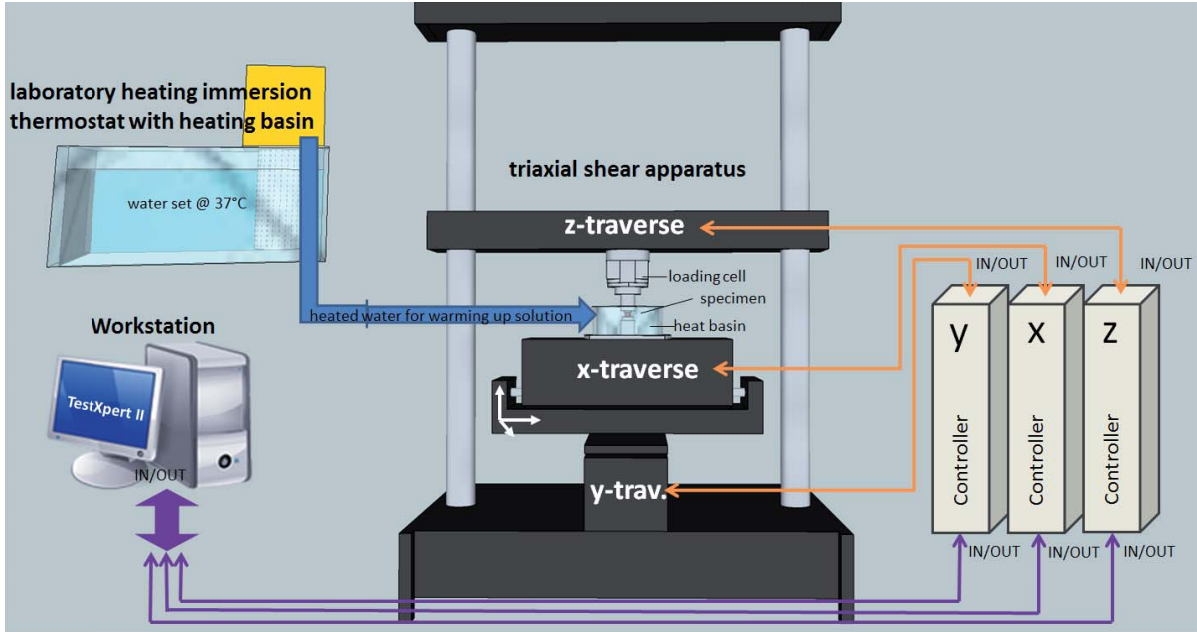
Figure 3.1.: Illustration showing the triaxial shear testing device (taken from Kutschera [35]).
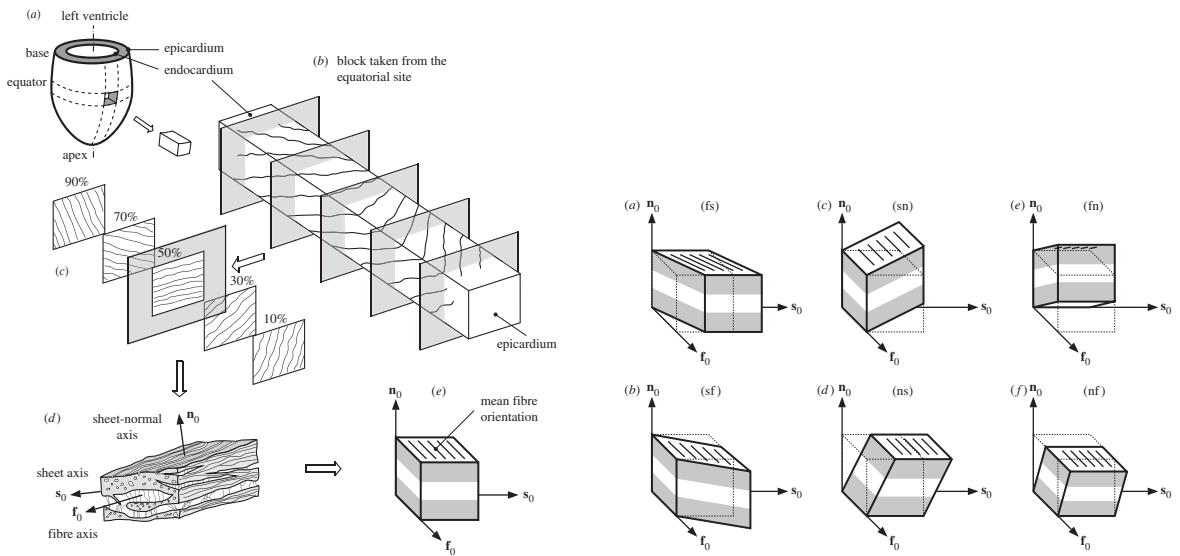
(a) Fiber and sheet orientation throughout the myocardium (taken from Holzapfel et al. [25]).

(b) All six loading modes and their orientations (taken from Holzapfel et al. [25]).

Figure 3.2.: Basic model for the myocardium providing fundamental approaches for modeling.
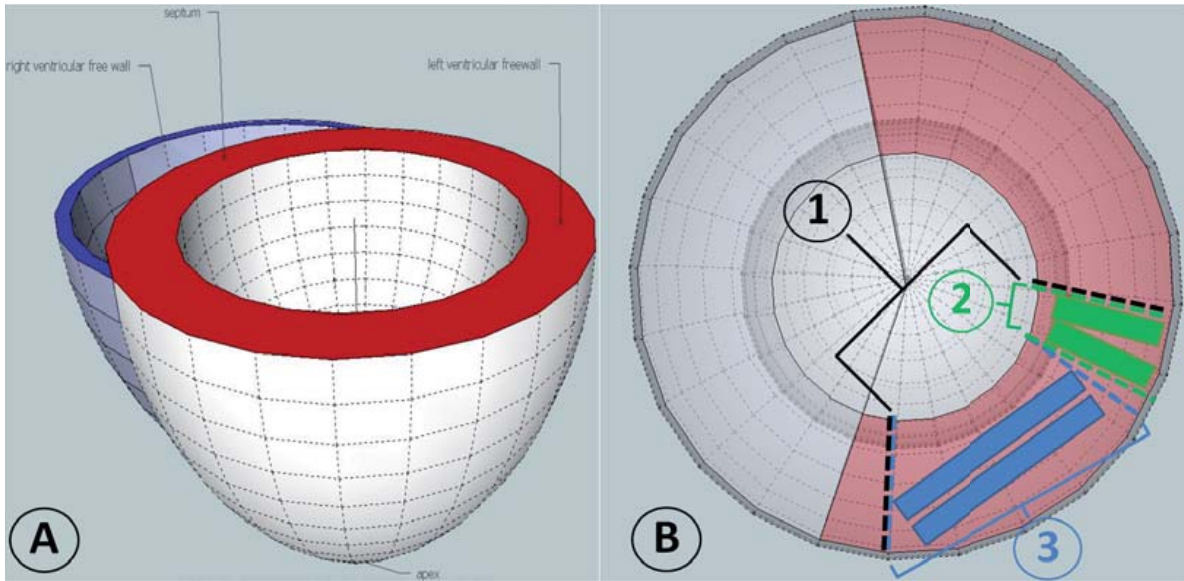
Figure 3.3.: (A): Computer model of the heart left ventricle wall and septum (red) and the right ventricle wall (blue). [35]
(B): Possible cutting position of ventricle walls by Kutschera. The red region marks the left ventricular free wall (LVFW) with possible excision slices for triaxial shear testing at region '2' and biaxial tensile testing at region '3'. [35]
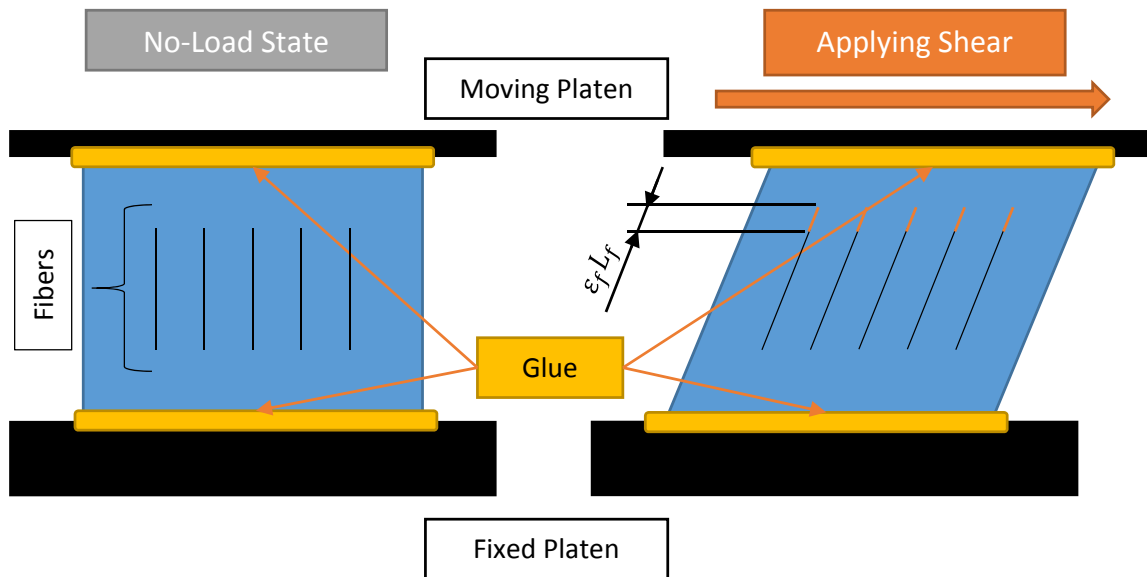
Figure 3.4.: Application of simple shear for FS-mode.

normal to the mounting platens and the load is applied normal to the fiber-sheet plane. All in all, six possible shear test loading modes can be conducted being FS, FN, SF, SN, NF and NS as shown in Fig. 3.2(b). Optimally, five tests at different shear peaks per loading mode can be performed. Hence, the total number of experiments per specimen sums up to 30 tests.

Exemplarily, in FS-mode loading we can design

$$f = f_0 \,, \tag{3.1}$$
$$s = \gamma f_0 + s_0 \,, \tag{3.2}$$
$$n = n_0 \,, \tag{3.3}$$

which defines the deformation gradient by

$$\mathbf{F} = \begin{pmatrix} 1 & 0 & 0 \\ \gamma & 1 & 0 \\ 0 & 0 & 1 \end{pmatrix} . \tag{3.4}$$

The underlying right Cauchy-Green tensor is then obtained through

$$\mathbf{C} = \begin{pmatrix} 1+\gamma^2 & \gamma & 0 \\ \gamma & 1 & 0 \\ 0 & 0 & 1 \end{pmatrix} , \tag{3.5}$$

with its most important invariants

$$\text{matrix stretch/shear...} \; I_1 = 3 + \gamma^2 \,, \tag{3.6}$$
$$\text{fiber stretch/shear...} \; I_4 = 1 + \gamma^2 \,, \tag{3.7}$$
$$\text{sheet stretch/shear...} \; I_6 = 1 \,, \tag{3.8}$$
$$\text{coupling stretch/shear...} \; I_8 = \gamma \,. \tag{3.9}$$

Thus, we see that for FS-mode loading the matrix, fibers and coupling structures are exposed to shear and stretch, respectively. Moreover, the fibers are stretched as $I_4 \geq 1$ for $\gamma \neq 0$ but not the sheets which stay undeformed and, thus, do not contribute in distribution of load.

As already mentioned, 30 tests can be carried out for every specimen. Unfortunately, if once glued, the tissue cubes cannot be used for further testing anymore. Hence, three cubes are excised in order to be exposed to shear in two loading directions for $\hat{\gamma} = 0, 0.1, ..0.5$. This may cause irregularities due to different location of specimen when conducting analysis of data.

In order to prevent tissue from drying or developing necrosis some hearts have been stored and tested in environment of cardioplegic solution (CPS), i.e. an isotonic water solution in order to prevent diffusion and osmotic processes. As the myocardium is a muscle of striated type, its main structural element is the sarcomere containing actin, myosin and titin [38]. These composites can be electromechanically activated as models

of Sachse et al. [47], Seeman et al. [50] and Tusscher et al. [60] prove. In order to obtain passive myocardial test data the usage of a substance called 2,3-butanedione monoxime (BDM) is obligatory. BDM prevents cross-bridge activation through selective inhibition of myosin adenosine triphosphatase (ATPase) (note: BDM is not a general myosin inhibitor [40]) and muscle contraction due to injury as stated by Mulieri et al. [39] as well as force inhibition as shown by Ebus et al. [10]. Remarkably, Soeno et al. [52] have reported that BDM also affects myofibrillogenesis causing reduced growth and structural differentiation.

As soft biological tissues show history depended loading behavior, preconditioning is obligatory establishing orientation of structural components within the tissue [37, 61]. Unpreconditioned soft tissues show viscoelastic unequal mechanical results when subjected to redundant loading which is unfavorable for investigation and modeling. Therefore, the last cycle of every loading pattern is used for data analysis. Eventually, preconditioning leads to repeatedly redundant hysteresis curves which is a fundamental requirement for decomposition of hysteresis stress into elastic and viscous stress parts.

Shear loads are applied sinusoidal via $\gamma = \hat{\gamma}\sin(2\pi f t)$, where $\hat{\gamma}$ is the peak of shear for the current loading cycle and f refers to the loading frequency. In order to reduce the influence of higher shear rates for constant frequency, the frequency f is adjusted so that the maximum rate of shear is held constant over a various set of tests (see Eq. (3.11)).

$$
\begin{aligned}
\dot{\gamma}(t) &= \frac{\mathrm{d}\gamma}{\mathrm{d}t} \\
&= 2\pi f \hat{\gamma}\cos(2\pi f t) \\
&= \dot{\hat{\gamma}}\cos(2\pi f t)
\end{aligned}
\tag{3.10}
$$

Thus, we define the frequency for constant rate of shear loading via

$$
f(\hat{\gamma}, \dot{\hat{\gamma}}) = \frac{\dot{\hat{\gamma}}}{2\pi\hat{\gamma}} \, ,
\tag{3.11}
$$

which defines the overall platen velocity $v(t) = \dot{\gamma}(t)h$ through

$$
v(t) = h\dot{\hat{\gamma}}\cos\left(\frac{\dot{\hat{\gamma}}}{\hat{\gamma}}t\right) \, ,
\tag{3.12}
$$

with h as the specimen height. Consequently, we keep the rate of shear consistently independent of the size of the excised myocardial cube, e.g. for a peak amount of shear $\hat{\gamma} = 0.2$, a peak rate of shear $\dot{\hat{\gamma}} = 0.02\mathrm{s}^{-1}$ and a cube height of $h = 5\mathrm{mm}$ the resulting velocity is obtained through

$$
v(t) = 6\frac{\mathrm{mm}}{\mathrm{min}}\cos\left(6\mathrm{min}^{-1}t\right) \, .
\tag{3.13}
$$

Note.   Unfortunately, the test results described in Sec. 4.1 and Fig. 4.4 show that the rate of shear has been varied between different hearts but kept constant within hearts. A possible reason for this may be fixation of velocity and determination of rate of shear via $\dot{\gamma}(t) = v(t)/h$. Hence, a direct comparison between heart viscoelasticity is not always possible.

3.2. Data Preparation

Having conducted the triaxial shear testing, the raw data needs to be prepared for fitting.

Data Preparation

1. Detection of zero crossings in order to separate preconditioning cycles from main loading cycles (see Fig. 3.5(a)).

   a) In last loading cycle (main loading cycle) traverse of shear testing device reduces speed non-sinusoidal causing nonuniform unloading cycles with reduced amount of shear stress (see blue curve in Fig 3.5(b) compared to perfect sinus (red)).

2. Smoothing of raw stress data with using Matlab$^{\circledR}$'s smooth() function with filter 'sgolay' and a span of 1/100 of signal length or at least five (see Fig. 3.5(c)).

3. Correcting offset for main loading cycle so that $\tau_{main}(\gamma = 0, \dot{\gamma} > 0) = -\tau_{main}(\gamma = 0, \dot{\gamma} < 0)$ (see Fig. 3.5(c)).

4. Separation of cycles in usually two preconditioning and one main loading cycle (defined in the header of the test file) as shown in Fig. 3.5(d).

   a) Selection of new main loading cycle as marked in Fig 3.5(a) (see 'selected' region marked with arrows) which is the negative unloading curve of cycle 2 (green cycle in Fig 3.5(d)) combined with the following positive loading and unloading as well as negative loading curves of cycle 3 (blue).

5. Determine un-/loading curve parts for upper stress parts τ_{upper} with $\dot{\gamma} > 0$ and lower stress parts τ_{lower} for $\dot{\gamma} < 0$ (see Fig. 3.5(e)).

6. Assuming $\tau = \tau_{elast} + \tau_{visco}$ holds, decouple stresses.

   (a) Elastic stress parts with $\tau_{elast} = \text{mean}(\tau_{upper}, \tau_{lower})$.

   (b) Viscous stress parts with $\tau_{visco} = \tau - \tau_{elast}$.

7. Determine derivatives for data analysis.

An example of a prepared data file including its header information and data analysis steps are shown in Appendix A.1. The corresponding data is a composition of cells and structs. A selection of the first layer of data-structure is shown in Table 3.1.

3.3. Modeling Using Existing Models

Within the last couple of decades a series of constitutive models for tissue have been designed. Those reach from simple phenomenological polynomial fits up to sophisticated hyperelastic strain-energy functions. The list of proposed models is long and reaches from isotropic models by, e.g. Fung in 1967 [18] and Demiray in 1976 [8], over transversely
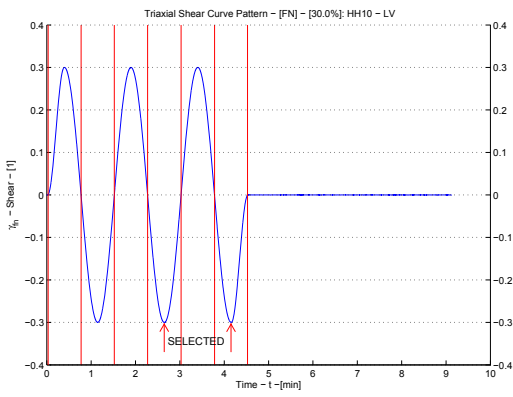
(a) Shear pattern.
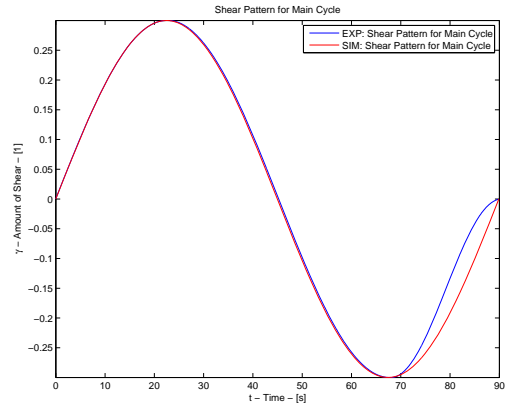
(b) Non-sinusoidal end of traverse movement for last cycle.
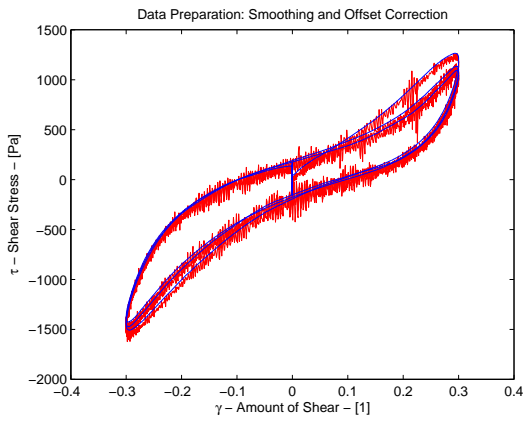
(c) Signal denoising.
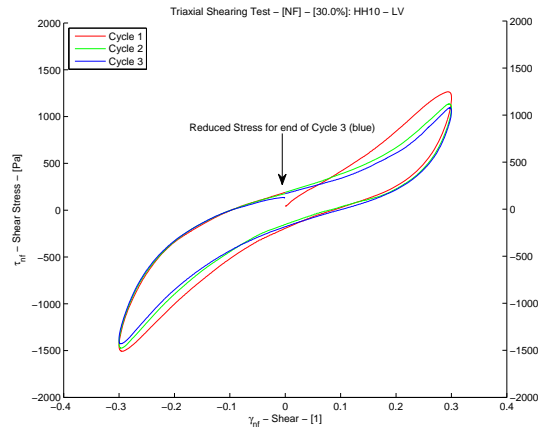
(d) Separation of loading cycles.
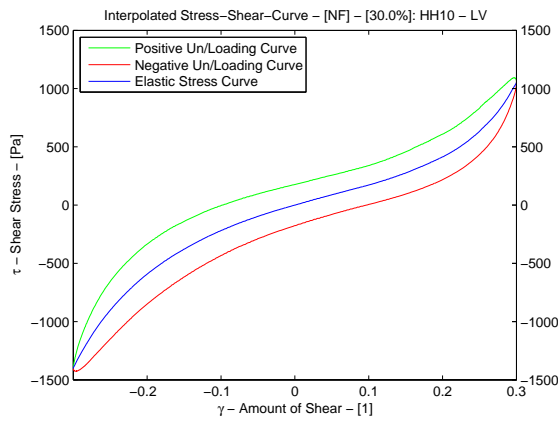
(e) Separation of elastic and viscous stresses.

Figure 3.5.: Data preparation procedure.

Table 3.1.: Data description and structure.

strain	...	defined peak amount of shear
shear	...	complete amount of shear data for all cycles
stress	...	complete shear stress data for all cycles
zcross	...	zero crossings of shear for cycle separation
peak	...	peaks of shear for loading and unloading curve separation
freq	...	determined loading frequency for main loading cycle
elastic	...	elastic components
visco	...	viscous components
selastic	...	stiffer elastic shear stress curve
svisco	...	stiffer viscous shear stress curve
felastic	...	pseudo-elastic components determined via fit of hysteresis data
lelastic	...	loading curves only and shifted to zero
damage	...	damage components obtained via felastic (optional)
relax	...	stress relaxation curves (optional)

isotropic models by, e.g. Humphrey & Yin in 1987 [29], Humphrey et al. in 1990 [28], Guccione et al. in 1991 [21] and Costa et al. in 1996 [4], up to orthotropic models by, e.g. Hunter et al. in 1997 [31], Costa et al. in 2001 [3], Schmid et al. in 2006 [48], Gasser et al. in 2006 [20] and more recently Holzapfel et al. in 2009 [25].

A shortcoming of phenomenologically motivated polynomial models are that the estimated parameter set does not have a direct biomechanical meaning. Thus, models based on building strain-energy functions provide more information referred to their parameter set.

Generally, nearly all exponential hyperelastic models are based on the work of Fung [18]. In his work, he states that the stiffness of the tissue is based on the momentary amount of applied stress (compare Fig. 4.7 in Sec. 4.1). Fung introduces a stiffness parameter a as well as a nonlinearity parameter b and suggests a relation based on the first Piola-Kirchhoff stress P_{11} and its corresponding stretch λ_{11} via

$$\frac{\mathrm{d}P_{11}}{\mathrm{d}\lambda_{11}} = a + bP_{11} \qquad \text{with} \qquad P_{11}(\lambda_{11} = 1) = 0 \,. \tag{3.14}$$

Solving this differential equation results to

$$P_{11} = \frac{a}{b} \left(e^{b(\lambda_{11} - 1)} - 1 \right) \,. \tag{3.15}$$

Fung postulates that the underlying strain-energy function written in terms of the Green-Lagrange strain tensor $\mathbf{E} = 1/2(\mathbf{C} - \mathbf{I})$ has the following form

$$\Psi(\mathbf{E}) = c \left(e^{(Q(\mathbf{E}) - 1)} - 1 \right) \,. \tag{3.16}$$

This strain-energy function can be used to obtain the symmetric second Piola-Kirchhoff stress tensor $\mathbf{S}$ via

$$\mathbf{S} = \frac{\partial \Psi(\mathbf{E})}{\partial \mathbf{E}} = c e^{(Q(\mathbf{E}) - 1)} \frac{\partial Q(\mathbf{E})}{\partial \mathbf{E}} \,. \tag{3.17}$$

Therefore, a vast variety of different strain-energy functions can be designed in order to describe the material behavior via $Q(\mathbf{E})$. In addition, we postulate based on the work of Dokos et al. [9] that shear stresses for different loading modes have to obey the following rule:

$$FS > FN > SF > SN > NF \approx NS \,. \tag{3.18}$$

This guarantees that stresses in direction of fibers or sheets are stiffer than those normal to them. This fundamental assumption is important for correct data collection of experiments.

Note. The proposed models which will be discussed in the following sections are orthotropic models. Although, isotropic and transversely isotropic models are also capable of describing the data in some way, we focus on orthotropic models only. In fact, myocardial tissue being exposed to biaxial stretching shows transversely isotropic behavior and, therefore, those models are sufficient [25] but not when it comes to triaxial simple shearing. Consequently, biaxial stress loading is an isolated experimental setup which lacks biomechanical properties of tissue being exposed to shearing and tensile loading simultaneously [25].

3.3.1. Orthotropic Hyperelastic Model with Perfect Fiber Alignment by Costa

Costa et al. [3] have designed a Fung-type model with one exponential term combining fiber, sheet and coupling effects. A lack of this model is that it uses only one stiffness parameter a and six nonlinearity parameters b. Thus, it assumes that the myocardium is a fixed structure with matrix-fiber-sheet compound which is treated as one in terms of stiffness.

The proposed strain-energy function Ψ based on the Green-Lagrange strain tensor $\mathbf{E} = 1/2(\mathbf{F}^{\mathrm{T}}\mathbf{F} - \mathbf{I})$ is given via

$$\Psi = a \left(e^{b_{ff}E_{ff}^2 + b_{ss}E_{ss}^2 + b_{nn}E_{nn}^2 + 2b_{fs}E_{fs}^2 + 2b_{fn}E_{fn}^2 + 2b_{sn}E_{sn}^2} - 1 \right) \,. \tag{3.19}$$

The resulting Cauchy-stress tensor results to

$$\boldsymbol{\sigma} = J^{-1}\mathbf{F}\frac{\partial\Psi(\mathbf{E})}{\partial\mathbf{E}}\mathbf{F}^{\mathrm{T}} = J^{-1}\mathbf{F}\sum_{i,j}\left(\frac{\partial\Psi(\mathbf{E})}{\partial E_{ij}}\underbrace{\frac{\partial E_{ij}}{\partial\mathbf{E}}}_{=\mathbf{e}_i\otimes\mathbf{e}_j}\right)\mathbf{F}^{\mathrm{T}} \,. \tag{3.20}$$

3.3.2. Orthotropic Hyperelastic Model with Perfect Fiber Alignment by Schmid

In addition to the model of Costa [3] a decoupled Fung-type exponential model has been proposed by Schmid et al. [48]. Schmid decouples the exponential terms and, therefore,

introduces stiffness parameters for fibers, sheets and coupling effects with twelve parameters in total. Thus, this model does not require fiber shear stresses being higher than sheet or normal direction stresses as proposed by Dokos et al. [9]. The underlying strain-energy function is obtained through

$$\Psi(I_1, I_4, I_6, I_8) = \frac{a_{ff}}{2}\left(e^{b_{ff}E_{ff}^2} - 1\right) + \frac{a_{fn}}{2}\left(e^{b_{fn}E_{fn}^2} - 1\right) + \frac{a_{fs}}{2}\left(e^{b_{fs}E_{fs}^2} - 1\right)$$
$$+ \frac{a_{nn}}{2}\left(e^{b_{nn}E_{nn}^2} - 1\right) + \frac{a_{ns}}{2}\left(e^{b_{ns}E_{ns}^2} - 1\right) + \frac{a_{ss}}{2}\left(e^{b_{ss}E_{ss}^2} - 1\right). \quad (3.21)$$

In fact, this model is capable of fitting experimental data which has been examined insufficiently. As the model fits every loading mode isolated and not its componential structure, all curves can be fitted separately and, therefore, fiber-sheet stresses could possible be lower than normal-sheet stresses which is physically incorrect. As the myocardium is known to show special characteristics concerning shear loading stresses, this model is overdetermined [25].

3.3.3. Orthotropic Hyperelastic Model with Perfect Fiber Alignment by Holzapfel and Ogden Using Invariants

A model suggested by Holzapfel et al. [25] describes the biomechanics of myocardium. This model is a composition of decoupled exponential terms describing the isotropic matrix, perfectly aligned fibers as well as sheets and fiber-sheet coupling. In the following sections we will refer to this model as 'ALIGNED' model. The corresponding strain-energy function is given via

$$\Psi(I_1, I_4, I_6, I_8) = \frac{a}{2b}\left(e^{b(I_1 - 3)} - 1\right)$$
$$+ \frac{a_f}{2b_f}\left(e^{b_f(I_4 - 1)^2} - 1\right)$$
$$+ \frac{a_s}{2b_s}\left(e^{b_s(I_6 - 1)^2} - 1\right)$$
$$+ \frac{a_{fs}}{2b_{fs}}\left(e^{b_{fs}I_8^2} - 1\right). \quad (3.22)$$

This model unites the biomechanics of an isotropic matrix, an orthotropic fiber reinforcement as well as an orthotropic layered sheet structure. Furthermore, shear testing of myocardium suggests orthotropic rather than transversely isotropic material behavior [25]. Note, when conducting biaxial tests the resulting experimental data can be fitted well with transversely isotropic models. This emphasizes the great capability and importance of triaxial shear tests for detailed material studies and constitutive modeling.

This model will be used for elastic stress description. It is capable of distinguishing between all modes except the NF-/NS-modes as the perimysial compounds between sheets are assumed to be part of the matrix compound [25].

3.3.4. Modeling Fiber Dispersion with Rotationally Symmetric Dispersion Using Structure Tensors

Another useful model has been proposed by Gasser et al. [20]. Although, it is meant to model arterial wall biomechanics it can be used for myocardium as well. Eriksson et al. [15] combined the model of Holzapfel and Gasser in order to unite them to an orthotropic hyperelastic model including fiber and sheet dispersion. Therefore, a dispersed structure tensor $\mathbf{H}$ is introduced.

The dispersion is modeled based on the π-periodic *von Mises* distribution $\rho(\mathbf{M})$ of fibers and sheets where $\mathbf{M}$ is an arbitrary vector in cylinder coordinates. Actually, ρ is a point-density function (PDF) describing the probability of finding fibers for certain orientations. The given cylindrical coordinate system is given by two angles Φ and Θ and the longitudinal main axis $\mathbf{e}_3$. Thus, the arbitrary tensor is obtained through

$$\mathbf{M} = \sin\Theta\cos\Phi\mathbf{e}_1 + \sin\Theta\sin\Phi\mathbf{e}_2 + \cos\Theta\mathbf{e}_3\,. \tag{3.23}$$

The structure tensor is then given via

$$\mathbf{H} = \frac{1}{4\pi}\int_{\Phi=0}^{2\pi}\int_{\Theta=0}^{\pi}\rho(\mathbf{M}(\Theta,\Phi))\mathbf{M}(\Theta,\Phi)\otimes\mathbf{M}(\Theta,\Phi)\sin(\Theta)\mathrm{d}\Theta\mathrm{d}\Phi\,. \tag{3.24}$$

Assuming the fibers are distributed rotationally symmetric around $\mathbf{e}_3$, we can eliminate Φ. This simplifies Eq. (3.24) to

$$\mathbf{H} = \frac{1}{2}\int_{\Theta=0}^{\pi}\rho(\mathbf{M}(\Theta))\mathbf{M}(\Theta)\otimes\mathbf{M}(\Theta)\sin(\Theta)\mathrm{d}\Theta\,. \tag{3.25}$$

Finally, Gasser et al. [20] derives the structure tensor by introducing the dispersion parameter $\kappa \in \{x \in \mathbf{R} | 0 \leq x \leq 1/3\}$ via

$$\mathbf{H} = \begin{pmatrix} \kappa & 0 & 0 \\ 0 & \kappa & 0 \\ 0 & 0 & 1-2\kappa \end{pmatrix} = \kappa\begin{pmatrix} 1 & 0 & 0 \\ 0 & 1 & 0 \\ 0 & 0 & 1 \end{pmatrix} + \begin{pmatrix} 0 & 0 & 0 \\ 0 & 0 & 0 \\ 0 & 0 & 1-3\kappa \end{pmatrix} = \kappa\mathbf{I} + (1-3\kappa)\mathbf{e}_3\otimes\mathbf{e}_3\,. \tag{3.26}$$

Remark. In case of fully aligned fibers $\kappa = 0$ and for completely isotropically distributed fibers $\kappa = 1/3$.

Consequently, we can replace $\mathbf{A} = \mathbf{e}_3\otimes\mathbf{e}_3$ with every direction needed. $\mathbf{A}$ is then identified as a perfectly aligned structure tensor with no dispersion at all. The dispersed invariant representing fibers I_4^* is given by

$$\begin{aligned} I_4^* &= \mathbf{C} : \mathbf{H}_F \\ &= \mathbf{C} : (\kappa_f\mathbf{I} + (1-3\kappa)\mathbf{F}_0) = \kappa_f\underbrace{\mathrm{tr}(\mathbf{C})}_{=I_1} + (1-3\kappa_f)\underbrace{\mathbf{C}:\mathbf{F}_0}_{=I_4} \\ &= \kappa_f I_1 + (1-3\kappa_f)I_4\,, \end{aligned} \tag{3.27}$$

and the dispersed invariant representing sheets I_6^* is given by

$$
\begin{aligned}
I_6^* &= \mathbf{C} : \mathbf{H}_S \\
&= \mathbf{C} : (\kappa_s \mathbf{I} + (1 - 3\kappa_s)\mathbf{S}_0) = \kappa_s \underbrace{\text{tr}(\mathbf{C})}_{=I_1} + (1 - 3\kappa_s)\underbrace{\mathbf{C} : \mathbf{S}_0}_{=I_6} \\
&= \kappa_s I_1 + (1 - 3\kappa_s)I_6 \, .
\end{aligned}
\tag{3.28}
$$

As proposed by Eriksson et al. [15] the complete strain-energy function including dispersion of fibers κ_f and sheets κ_s is given by

$$
\begin{aligned}
\Psi(I_1, I_4, I_6, I_8) = \; & \frac{a}{2b}\left(e^{b(I_1 - 3)} - 1\right) \\
&+ \frac{a_f}{2b_f}\left(e^{b_f(\kappa_f I_1 + (1 - 3\kappa_f)I_4 - 1)^2} - 1\right) \\
&+ \frac{a_s}{2b_s}\left(e^{b_s(\kappa_s I_1 + (1 - 3\kappa_s)I_6 - 1)^2} - 1\right) \\
&+ \frac{a_{fs}}{2b_{fs}}\left(e^{b_{fs}I_8^2} - 1\right) \, .
\end{aligned}
\tag{3.29}
$$

In the following sections we will refer to this model as 'KAPPA' model. Note, when setting $\kappa_f = \kappa_s = 0$ there is no dispersion at all and the model of Eriksson et al. [15] is equal to the model of Holzapfel et al [25].

3.4. Approach for New Models

Motivation. By now, a couple of hyperelastic models have been presented which describe the biomechanics of myocardium in equilibrium. Recent experiments prove that rate of shear dependencies cause viscoelastic effects and hysteresis even at low rates of shear (see [35]). Consequently, viscoelastic modeling is obligatory as viscoelastic effects show strong influence on myocardial mechanics, e.g. wall thickening [36], sliding of sheets and reformation of myocardium during systole [55] and diastole [6].

3.4.1. Orthotropic Hyperelastic Model with Perfect Fiber Alignment Including Perimysium

In order to distinguish NF-/NS-mode loading we need to add an additional term. Saying $I_9 = \mathbf{n_0} \cdot \mathbf{Cf_0}$ which is the coupling of normal and fiber direction stretch, we can formulate

an extended hyperelastic model based on Holzapfel et al. [25] via

$$
\begin{aligned}
\Psi(I_1, I_4, I_6, I_8, I_9) = {} & \frac{a}{2b}\left(e^{b(I_1-3)} - 1\right) \\
& + \frac{a_f}{2b_f}\left(e^{b_f(I_4-1)^2} - 1\right) \\
& + \frac{a_s}{2b_s}\left(e^{b_s(I_6-1)^2} - 1\right) \\
& + \frac{a_{fs}}{2b_{fs}}\left(e^{b_{fs}I_8^2} - 1\right) \\
& + \frac{a_{nf}}{2b_{nf}}\left(e^{b_{nf}I_9^2} - 1\right).
\end{aligned}
\tag{3.30}
$$

This model consists of ten parameters but most of the time NF-/NS-mode stresses are congruent. Hence, the NF-coupling invariant I_9 will be close to zero most of the time, especially when thin layers of myocardium are tested [9, 15, 25].

Note. The determination of an eight parameter model is a challenging task in terms of finding the global minimum of the objective function and is even harder when considering a ten parameter model. Eventually, at some point more parameters reduce the confidence of single parameters but do not increase confidence in a acceptable manner.

3.4.2. Hyperelastic Model with Ellipsoidal Distribution of Fibers

Recently, within his master's thesis Reinisch [45] has proposed an orthotropic fiber dispersion model including in-plane and out-of-plane dispersions κ_{ip} and κ_{op}, respectively. The structure tensor $\mathbf{H}$ is modeled via a bi-variate *von Mises* distribution and given by

$$
\mathbf{H} = \frac{1}{4\pi}\int_{\Phi=0}^{2\pi}\int_{\Theta=0}^{\pi}\rho(\mathbf{M}(\Theta, \Phi))\mathbf{M}(\Theta, \Phi)\otimes\mathbf{M}(\Theta, \Phi)\sin\Theta\,\mathrm{d}\Theta\,\mathrm{d}\Phi,
\tag{3.31}
$$

where the probability density function $\rho(\Theta, \Phi)$ of finding a certain direction of fiber orientation is obtained with a multiplicative merge of the independent in-plane and out-of-plane PDFs via $\rho = \rho_{ip}(\Phi)\rho_{op}(\Theta)$. Finally, the complete structure tensor is defined through a given fiber direction tensor $\mathbf{M_f}$ and a normal direction vector $\mathbf{M_n}$ which is orthogonal to the direction of fibers and their dispersion plane. The structure tensor is given by

$$
\mathbf{H} = 3\kappa_{ip}\kappa_{op}\mathbf{I} + \left(2\kappa_{op}(1 - 3\kappa_{ip})\right)\mathbf{M}_f\otimes\mathbf{M}_f + \left(1 - \kappa_{op}(2 + 3\kappa_{ip})\right)\mathbf{M}_n\otimes\mathbf{M}_n.
\tag{3.32}
$$

Assimilated on myocardial biomechanics two dispersion parameters per fiber- family would sum up to four dispersion parameters for fibers and sheets in total. Due to the lack of experimental data on out-of-plane dispersion for myocardial tissue and the assumption that healthy myocardium shows rotationally symmetric dispersion, this model is not further reviewed within this thesis. Note, this assumption is not fulfilled when modeling diseased tissue (see Schriefl et al. [49]).

3.4.3. Modeling Inelasticity

In the past, various groups tried to reproduce the viscoelastic effects of tissue by using iterative numerical solutions for modeling (see [3, 22, 24, 32]). Unfortunately, by doing so direct parameter estimations via objective function minimization algorithms are not applicable and, thus, data analysis fails from this point of view.

So far, we derived hyperelastic models which are based on the Green-Lagrange strain tensor $\mathbf{E}$ or the right Cauchy-Green tensor $\mathbf{C}$, its volume preserving pendant $\bar{\mathbf{C}}$ and their scalar invariants $\bar{I}_i$ $(i = 1, 2, 3, 4, 6, 8)$ only.

As the human heart muscle consists of a solid phase with different compositions of fibers, sheets and ground substance composites as well as high portion of water (nearly 80% based on Pogàtsa et al. [43], see Sec.1.2), hysteresis in stress-strain curves can be obtained (see Kutschera [35] and Sommer et al. [54]). Thus, we assume that hysteresis is a composition of elastic and viscoelastic/inelastic stress terms.

Therefore, we introduce new pseudo-invariants which are time-derivatives $\dot{\bar{I}}_i = \mathrm{d}\bar{I}_i/\mathrm{d}t$. Using these new invariants one can now include the rate of shear $\dot{\gamma}$ which employs us to model viscoelastic/inelastic behavior. In case of FS-mode shearing the deformation gradient $\mathbf{F}$ is given via

$$\bar{\mathbf{F}} = \frac{\mathbf{F}}{\mathrm{Det}(\mathbf{F})^{1/3}} = J^{-1/3}\mathbf{F} = \begin{pmatrix} 1 & 0 & 0 \\ \gamma & 1 & 0 \\ 0 & 0 & 1 \end{pmatrix}. \tag{3.33}$$

The corresponding right Cauchy-Green tensor $\bar{\mathbf{C}} = J^{-2/3}\mathbf{F}^{\mathrm{T}}\mathbf{F}$ is composed through

$$\bar{\mathbf{C}} = \begin{pmatrix} 1 + \gamma^2 & \gamma & 0 \\ \gamma & 1 & 0 \\ 0 & 0 & 1 \end{pmatrix}. \tag{3.34}$$

Furthermore, the material velocity field $\mathbf{V}(\mathbf{X}, t)$ is given via

$$\mathbf{V}(\mathbf{X}, t) = \frac{\partial}{\partial t}(\mathbf{x}(\mathbf{X}, t) - \mathbf{X}(t)). \tag{3.35}$$

Finally, the material velocity gradient $\dot{\mathbf{F}} = \mathrm{d}\mathbf{F}/\mathrm{d}t = \mathrm{grad}(\mathbf{V}(\mathbf{X}, t))$ can be used to create the time-derivative of the right Cauchy-Green tensor $\dot{\mathbf{C}} = \mathrm{d}\mathbf{C}/\mathrm{d}t$ which has the following form

$$\dot{\mathbf{C}} = \frac{\mathrm{d}\bar{\mathbf{C}}}{\mathrm{d}t} = J^{-2/3}\frac{\mathrm{d}}{\mathrm{d}t}\left(\mathbf{F}^{\mathrm{T}}\mathbf{F}\right) = J^{-2/3}\left(\dot{\mathbf{F}}^{\mathrm{T}}\mathbf{F} + \mathbf{F}^{\mathrm{T}}\dot{\mathbf{F}}\right) = \begin{pmatrix} 2\gamma\dot{\gamma} & \dot{\gamma} & 0 \\ \dot{\gamma} & 0 & 0 \\ 0 & 0 & 0 \end{pmatrix}. \tag{3.36}$$

Now, we can also define the new time-derivative invariants $\dot{\bar{I}}_i$ (see Eqs. (3.37), (3.38),

(3.39) and (3.40)).

$$\dot{\bar{I}}_1 = \frac{\mathrm{d}\bar{I}_1}{\mathrm{d}t} = \mathrm{Tr}(\dot{\bar{\mathbf{C}}})\,, \qquad \text{e.g. } \dot{\bar{I}}_{1,FS} = 2\gamma\dot{\gamma}\,, \tag{3.37}$$

$$\dot{\bar{I}}_4 = \frac{\mathrm{d}\bar{I}_4}{\mathrm{d}t} = \mathbf{f_0} \cdot \dot{\bar{\mathbf{C}}}\mathbf{f_0}\,, \qquad \text{e.g. } \dot{\bar{I}}_{4,FS} = 2\gamma\dot{\gamma}\,, \tag{3.38}$$

$$\dot{\bar{I}}_6 = \frac{\mathrm{d}\bar{I}_6}{\mathrm{d}t} = \mathbf{s_0} \cdot \dot{\bar{\mathbf{C}}}\mathbf{s_0}\,, \qquad \text{e.g. } \dot{\bar{I}}_{6,FS} = 0\,, \tag{3.39}$$

$$\dot{\bar{I}}_8 = \frac{\mathrm{d}\bar{I}_8}{\mathrm{d}t} = \mathbf{f_0} \cdot \dot{\bar{\mathbf{C}}}\mathbf{s_0}\,, \qquad \text{e.g. } \dot{\bar{I}}_{8,FS} = \dot{\gamma}\,. \tag{3.40}$$

Note. Here, we introduce a condition which arises from quasistatic shearing. Equations (3.42) and (3.43) show a condition which definition is required for further inelasticity modeling. As quasistatic loading means that low rates of shear are used for testing, the acceleration $\ddot{\gamma}$ must be set to zero. Thus, we can write

$$\ddot{\gamma} = \frac{\mathrm{d}\dot{\gamma}}{\mathrm{d}\gamma}\frac{\mathrm{d}\gamma}{\mathrm{d}t} = \dot{\gamma}\frac{\mathrm{d}\dot{\gamma}}{\mathrm{d}\gamma} \overset{!}{=} 0\,. \tag{3.41}$$

In general, $\dot{\gamma} \neq 0$ which leads to

$$\lim_{\dot{\gamma}\to 0}\left(\frac{\mathrm{d}\dot{\gamma}}{\mathrm{d}\gamma}\right) = 0\,, \text{and its tensor pendant} \tag{3.42}$$

$$\lim_{\dot{\mathbf{F}}\to\mathbf{0}}\left(\frac{\partial\dot{\mathbf{F}}}{\partial\mathbf{F}}\right) = \mathbb{O}\,. \tag{3.43}$$

This enables us to model inelasticity without knowledge of actual deformation in every element, e.g. springs or dashpots. Otherwise, we would have to use a numerical approach with including history variables of previous deformation states and a series of evolution equations as proposed by Holzapfel et al. [23].

In Fig. 3.6 the viscoelastic/inelastic stress response to simple shearing is shown. The blue curves show shearing until $\gamma = 0.1$ is reached where progressive decrease can be obtained. The next cycles at $\gamma = 0.2$-0.5 always show progressive increase of stress followed by strong decrease after reaching the previous loading stretch. This can be obtained by determination of the points of inflection. Apparently, the viscoelastic/inelastic stress response is characterized through 'restructuring' (R) and 'damping' (D). It seems that 'restructuring' occurs when fibers and sheets are reorientated during higher shear values than in previous loading cycles whereas 'damping' dominates after restructuring effects decrease and fibers as well as sheets are more detached and softened. Another reason for the restructuring effect could be declared with sliding sheets of fibers lying next to each other causing angular rotation of sheets.

The restructuring effect describes fiber realignment as well as softening processes in the myocardium after loading in one direction, e.g. FS-mode, at higher shear values than previously in transverse directions, e.g. FN-mode. As widely dispersed fibers are section-wise crooked in the no-load state, these fiber-sheet compounds block fluid flow
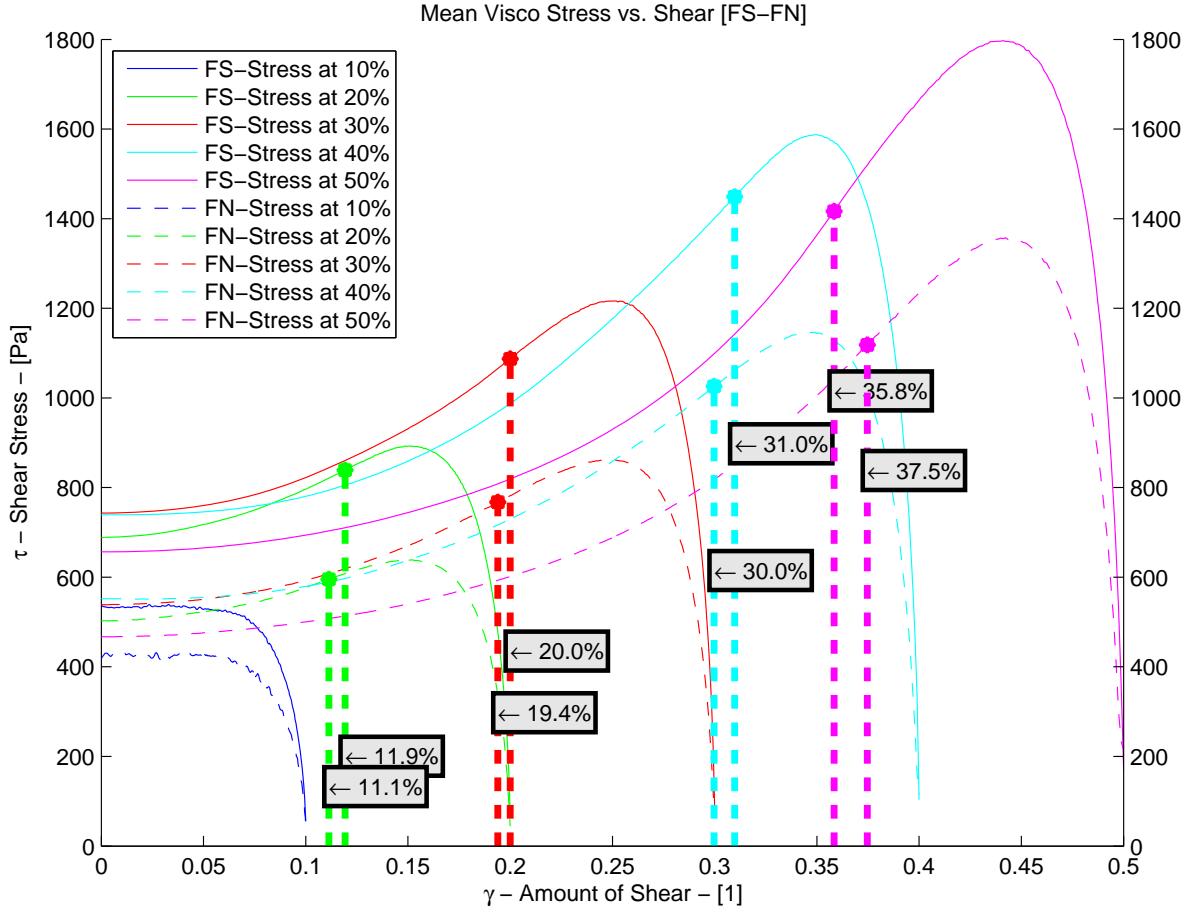
Figure 3.6.: Viscoelastic/inelastic stress response for [FS-FN]-mode at $\gamma = 0.1 - 0.5$ with marks at the points of inflection.

and thus increase stress drastically, compared to simple dashpot-damping. After a new loading cycle in transverse direction the fibers seem to be aligned and allow simple damping effects to be dominant until the previous shear load limit is reached (see points of inflection in Fig. 3.6).

Using Eq. (3.36) we create a new approach in order to model the viscoelastic/inelastic behavior via a composition of different models. As the generalized Maxwell-model cannot be composed in a simple strain-energy function form, we use a theoretical approach for describing the periodic viscoelastic/inelastic response. Eventually, the theoretical framework is given via Eq. (3.44).

Note. The viscoelastic/inelastic stress response models are defined through periodic equations only. As the experiments are carried out nearly quasi-static, we neglect transient solution terms of the proposed differential equations in the following models.

Figures 3.7(a) and 3.7(b) are sketches of obtained plots during triaxial shear testing. These employ us to build up general differential equations for modeling inelasticity. In Figure 3.8 the complete model is shown. The isochoric part Ψ_{isoc} is split up in an elastic
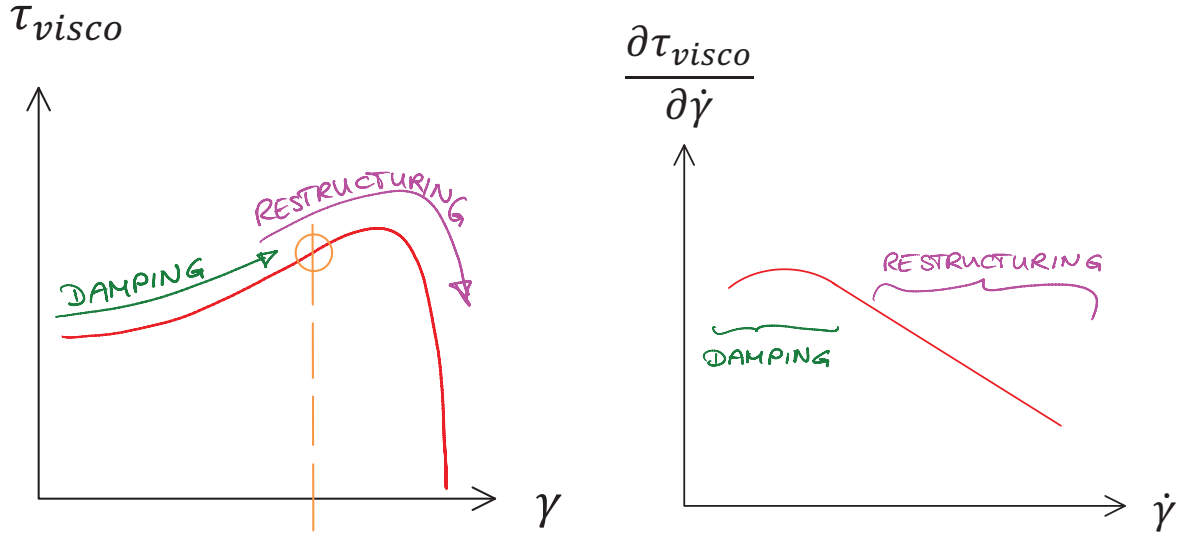
(a) Viscoelastic/inelastic stress response scheme showing damping and restructuring effects.

(b) Viscoelastic/inelastic damping $\mu = \mathrm{d}\tau_{visco}/\mathrm{d}\dot\gamma$ response scheme showing damping and restructuring effects.

Figure 3.7.: Schemes for modeling viscoelastic/inelastic stress response for quasistatic loading.

Ψ_{elast} and an viscoelastic/inelastic Ψ_{inel} energy part. Furthermore, the elastic part is defined via three terms merging an isotropic Ψ_{isot}, a fiber-fabric Ψ_{ff} and a fiber-sheet coupling Ψ_{coup} energy part. Finally, the viscoelastic/inelastic part contains of a damping and a restructuring energy term (see Eqs. (3.45), (3.46) and (3.47)).

$$\Psi(J, \bar{I}_1, \bar{I}_4, \bar{I}_6, \bar{I}_8, \dot{\bar{I}}_1, \dot{\bar{I}}_4, \dot{\bar{I}}_6, \dot{\bar{I}}_8) = \Psi_{vol}(J) + \Psi_{isoc}(\bar{I}_1, \bar{I}_4, \bar{I}_6, \bar{I}_8, \dot{\bar{I}}_1, \dot{\bar{I}}_4, \dot{\bar{I}}_6, \dot{\bar{I}}_8) \tag{3.44}$$

In detail, the energy parts are designed via

$$\Psi_{isoc} = \Psi_{elast} + \Psi_{inel}\,, \tag{3.45}$$

$$\Psi_{elast} = \Psi_{isot}^{(m)} + \sum_{i=f,s} \Psi_{ff}^{(i)} + \Psi_{coup}^{(fs)} \quad \text{and} \tag{3.46}$$

$$\Psi_{inel} = \Psi_{inel}^{(R)} + \int \dot{\Psi}_{inel}^{(D)}\,\mathrm{d}t\,. \tag{3.47}$$

Finally, we need to define the form of the invariants and their derivatives as well as the dissipative strain-power function $\dot{\Psi}_{inel}$ and recall the Clausius-Planck [23] equation

$$D_{int} = \mathbf{P} : \dot{\mathbf{F}} - \dot{\Psi}\,. \tag{3.48}$$

When considering a complete irreversible process, we postulate that the rate of mechanically reversible work $\dot{\Psi} = 0$ and the dissipation is given by

$$D_{int}^{(D)} = \mathbf{P}_{inel}^{(D)} : \dot{\mathbf{F}} = \dot{\Psi}_{inel}^{(D)}\,. \tag{3.49}$$
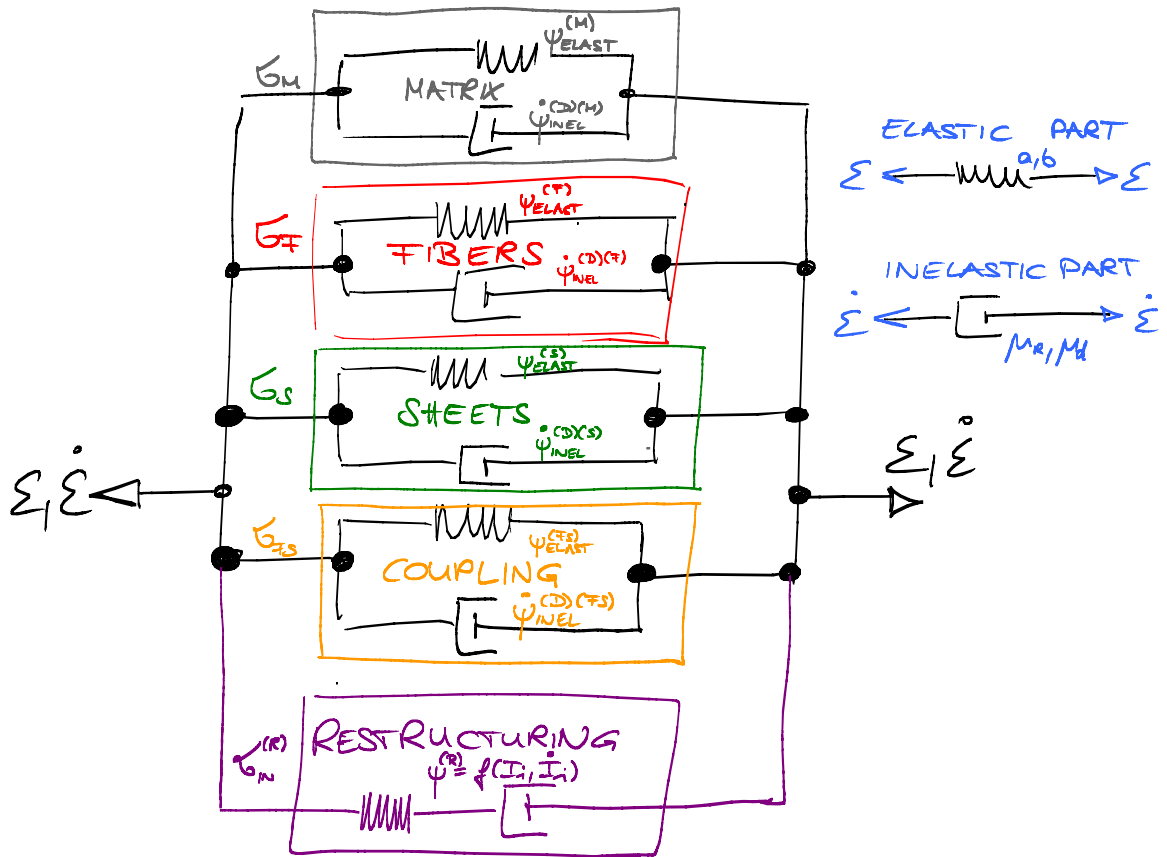
Figure 3.8.: Sketch of the approach for modeling elastic and viscoelastic/inelastic behavior.

Hence, we call this the damping strain-power function $\dot{\Psi}_{inel}^{(D)}$. In general, it is not possible to determine the stress tensor from the power function and the material velocity gradient itself. In order to solve this problem, we define the damping effects as the viscoelastic/inelastic first Piola-Kirchhoff stress tensor $\mathbf{P}_{inel}$ and the viscoelastic/inelastic strain-power function $\dot{\Psi}_{inel}$ by using Eq. (3.43) through

$$
\begin{aligned}
\mathbf{P}_{inel} &= \frac{\partial \Psi_{inel}^{(R)}(\bar{I}_1, \bar{I}_4, \bar{I}_6, \bar{I}_8, \dot{\bar{I}}_1, \dot{\bar{I}}_4, \dot{\bar{I}}_6, \dot{\bar{I}}_8)}{\partial \mathbf{F}} + \frac{\partial \dot{\Psi}_{inel}^{(D)}(\dot{\bar{I}}_1, \dot{\bar{I}}_4, \dot{\bar{I}}_6, \dot{\bar{I}}_8)}{\partial \dot{\mathbf{F}}} \\
&= \sum_i \left[\left(\frac{\partial \Psi_{inel}^{(R)}(\bar{I}_i, \dot{\bar{I}}_i)}{\partial \bar{I}_i} + \frac{\partial \Psi_{inel}^{(R)}(\bar{I}_i, \dot{\bar{I}}_i)}{\partial \dot{\bar{I}}_i} \underbrace{\frac{\partial \dot{\bar{I}}_i}{\partial \bar{I}_i}}_{=0} \right) \frac{\partial \bar{I}_i}{\partial \mathbf{F}} + \frac{\partial \dot{\Psi}_{inel}^{(D)}(\dot{\bar{I}}_i)}{\partial \dot{\bar{I}}_i} \frac{\partial \dot{\bar{I}}_i}{\partial \dot{\mathbf{F}}} \right] \\
&= \sum_i \left(\frac{\partial \Psi_{inel}^{(R)}(\bar{I}_i, \dot{\bar{I}}_i)}{\partial \bar{I}_i} \frac{\partial \bar{I}_i}{\partial \mathbf{F}} + \frac{\partial \dot{\Psi}_{inel}^{(D)}(\dot{\bar{I}}_i)}{\partial \dot{\bar{I}}_i} \frac{\partial \dot{\bar{I}}_i}{\partial \dot{\mathbf{F}}} \right).
\end{aligned}
\tag{3.50}
$$

Equation (3.50) shows that the viscoelastic/inelastic response is decoupled into two separate terms where $\Psi_{inel}^{(R)}$ describes the fiber-sheet reorientation through previous stretching cycles and $\dot{\Psi}_{inel}^{(D)}$ describes the damping effects which cause stress through viscoelastic effects.

This influences the way we define the strain-power functions in order to have reasonable results. The complete Cauchy stress tensor with Eqs. (3.36) and (3.50) has the following form

$$
\boldsymbol{\sigma} = \frac{2}{J} \mathbf{F} \left(\frac{\partial \Psi_{vol}(J)}{\partial \mathbf{C}} + \frac{\partial \Psi_{elast}(\bar{I}_i)}{\partial \mathbf{C}} + \frac{\partial \Psi_{inel}^{(R)}(\bar{I}_i, \dot{\bar{I}}_i)}{\partial \mathbf{C}} + \frac{\partial \dot{\Psi}_{inel}^{(D)}(\dot{\bar{I}}_i)}{\partial \dot{\mathbf{C}}} \right) \mathbf{F}^{\mathrm{T}},
\tag{3.51}
$$

where $\Psi_{vol}(J) = p(J-1)$ describes the incompressibility constraint with the Lagrange multiplier p which may be interpreted as isotropic pressure.

After these definitions, we can now create new strain-energy functions $\Psi_{inel}^{(R)}$ as well as strain-power functions $\dot{\Psi}_{inel}^{(D)}$ by looking at Figs. 3.7(a) and 3.7(b).

The damping effects can be described through

$$
\tau_{inel,i}^{(D)} = \mu_i^{(D)} \dot{\gamma}_i, \qquad i = m, f, s, fs,
$$

$$
\begin{aligned}
\dot{\Psi}_{inel}^{(D)} &= \sum_{i=m,f,s,fs} \tau_{inel,i}^{(D)} \dot{\gamma}_i \\
&= \sum_{i=m,f,s,fs} \mu_i^{(D)} \dot{\gamma}_i^{\,2},
\end{aligned}
\tag{3.52}
$$

with following abbreviations: 'm' for matrix, 'f' for fiber, 's' for sheet, and 'fs' for fiber-sheet coupling. Here, every direction of rate of shear $\dot{\gamma}_i$ is linked to a certain stress term $\tau_{inel,i}^{(D)}$. In case of FS-mode loading the 'm', 'f' and 'fs' components are active.

The proposed power function has to fulfill the second law of thermodynamics which is proved via

$$\Delta = \tau_{inel}^{(D)}\dot{\gamma} = \underbrace{\mu^{(D)}}_{\geq 0}\underbrace{\dot{\gamma}^2}_{\geq 0} \geq 0 \,. \tag{3.53}$$

Figure 3.12(a) proves that the dissipation for different amounts of peak shear and direction of applied loads is always positive (using values from Table 4.8).

Therefore, the damping power function $\dot{\Psi}_{inel}^{(D)}$ is defined as

$$\dot{\Psi}_{inel}^{(D)} = \frac{1}{4}\left(\frac{\mu_m^{(D)}}{2}\frac{\dot{\bar{I}}_1^{\,2}}{\bar{I}_1 - 3} + \frac{\mu_f^{(D)}}{2}\frac{\dot{\bar{I}}_4^{\,2}}{\bar{I}_1 - 3} + \frac{\mu_s^{(D)}}{2}\frac{\dot{\bar{I}}_6^{\,2}}{\bar{I}_1 - 3} + \frac{\mu_{fs}^{(D)}}{2}\dot{\bar{I}}_8^{\,2}\right) , \tag{3.54}$$

where $\mu_i^{(D)}$ $(i = m, f, s, fs)$ are shear viscosity damping constants with unit $[\mu_i^{(D)}] = \mathrm{Pa\,s}$.

Note. The definition of invariants $\dot{\bar{I}}_i$ requires normalization of time-invariants one, four and six by the isotropic deformation $(\bar{I}_1 - 3)$. As the damping effects are described through rate of shear only, the normalization in FS-mode is given via

$$\frac{\dot{\bar{I}}_{1,FS}^{\,2}}{\bar{I}_{1,FS} - 3} = \frac{4\gamma_{FS}^2\dot{\gamma}_{FS}^2}{3 + \gamma_{FS}^2 - 3} = 4\dot{\gamma}_{FS}^2 \,. \tag{3.55}$$

Thus, the viscoelastic/inelastic shear response for FS-mode loading is given via

$$\tau_{inel,FS}^{(D)} = \dot{\gamma}_{FS}\left(\mu_m^{(D)} + \mu_f^{(D)} + \mu_{fs}^{(D)}\right) \,. \tag{3.56}$$

In Equation (3.56) the viscosity constants are additive and, therefore, simultaneous fitting by using objective function minimization algorithms are obligatory.

The restructuring effects can be derived when looking at Fig. 3.7(b) and the viscoelastic/inelastic stress curves. In order to isolate the restructuring effect from the damping effect, we use the following approach to eliminate the damping shear stress $\tau_{inel}^{(D)}$ from the total viscous shear stress τ_{inel}. This is achieved through using the previously defined simple Eq. (3.52) for simple damping via $\tau_{inel}^{(D)} = \mu_p^{(D)}\dot{\gamma}$ with $\mu_p^{(D)}$ being a permanent shear viscosity constant now. As the restructuring effect disappears at zero shear, we obtain

$$\tau_{inel} = \tau_{inel}^{(D)} + \tau_{inel}^{(R)} \,, \tag{3.57}$$

$$\tau_{inel}^{(D)} = \mu_p^{(D)}\dot{\gamma} \,, \tag{3.58}$$

$$\mu_p^{(D)} = \left.\frac{\tau_{inel}}{\dot{\gamma}}\right|_{\gamma=0} \,. \tag{3.59}$$

This gives us the restructuring shear stress for any given data via

$$\tau_{inel}^{(R)} = \tau_{inel} - \left.\frac{\tau_{inel}}{\dot{\gamma}}\right|_{\gamma=0}\dot{\gamma} \,. \tag{3.60}$$

The resulting decoupling of restructuring and damping stress is shown in Fig. 3.10. If we compare the restructuring viscosity with the viscoelastic damping curve in Fig. 3.9(b), we can find that the initial damping effect for low rates of shear is eliminated from the restructuring viscosity graph in Fig. 3.10. Hence, we assume that the viscosity is a function of the shear rate itself, and thus we introduce Eq. (3.61) in order to show that the restructuring is characterized through the permanent shear viscosity constant $\mu_p^{(R)}$ and an internal restructuring viscosity parameter $\mu_r^{(R)}$.

$$\frac{\mathrm{d}\tau_{inel}^{(R)\,\prime}}{\mathrm{d}\dot{\gamma}} = \mu_p^{(R)} + \mu_r^{(R)}\dot{\gamma} \qquad \text{and its solution} \tag{3.61}$$

$$\tau_{inel}^{(R)\,\prime} = \mu_p^{(R)}\dot{\gamma} + \mu_r^{(R)}\frac{\dot{\gamma}^2}{2}\,. \tag{3.62}$$

As the damping effects are already described well through Eq. (3.52), we reduce Eq. (3.62) by the permanent viscosity constant $\mu_p^{(R)}$ which simplifies Eq. (3.62) to

$$\tau_{inel}^{(R)\,\prime} = \mu_r^{(R)}\frac{\dot{\gamma}^2}{2}\,. \tag{3.63}$$

In addition, we know from observing Figs. 3.9(a) and 3.10 that the inelasticity module due to restructuring $\mathrm{d}\tau_{inel}^{(R)}/\mathrm{d}\gamma$ is nearly linear dependent of amount of shear γ and shows strong gradients towards the peaks of shear $\hat{\gamma}$ which is shown in the upper diagram in Fig. 3.9(a). Further investigation of Fig. 3.10 gives information about the pure restructuring stiffness behavior of the myocardium. Apparently, restructuring effects show directional dependencies and increasing stiffness for higher amount of shear. Therefore, we introduce a polynomial approach with odd powers in order to preserve symmetry.

This leads to an initial simple cubic spring model which always works against direction of applied shear via

$$\frac{\mathrm{d}\tau_{inel}^{(R)\,\prime\prime}}{\mathrm{d}\gamma} = c_r^{(R)}\gamma^3 \qquad \text{and its solution} \tag{3.64}$$

$$\tau_{inel}^{(R)\,\prime\prime} = c_r^{(R)}\frac{\gamma^4}{4}\,. \tag{3.65}$$

As the restructuring effect is modeled as a pseudo Maxwell material (see Fig. 3.8) the stress balance criterion $\tau_{inel}^{(R)} = \tau_{inel}^{(dashpot)\,\prime}(\gamma_d) = \tau_{inel}^{(spring)\,\prime\prime}(\gamma_s)$ has to be fulfilled. As we do not know the actual values of shear for the dashpot γ_d and spring γ_s for every moment, we postulate the geometric mean of stresses $\tau_{inel}^{(R)} = \sqrt{\tau_{inel}^{(R)\,\prime}\tau_{inel}^{(R)\,\prime\prime}}$ in order to obtain the combined strain-energy function. Hence, we model the 'restructuring' as a pseudo-Maxwell material for which dashpot and spring have same amount of shear and rate of shear in the periodic solution range ($\gamma_{dashpot} = \gamma_{spring}$ and $\dot{\gamma}_{dashpot} = \dot{\gamma}_{spring}$). As $\mathrm{d}\dot{\gamma}/\mathrm{d}\gamma = 0$, we assume that the rate of shear is assumed to be constant $\dot{\gamma} = \text{const}$. Using this trick we can derive the restructuring strain-energy $\Psi_{inel}^{(R)}$ simply via integration. Paradoxically, the derived strain-energy function is only useful for deriving the shear
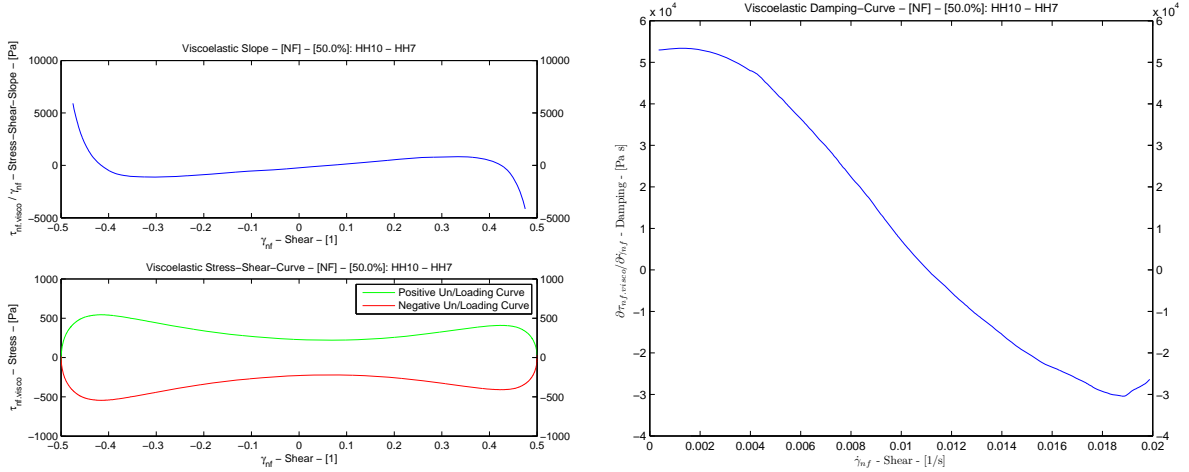
(a) Viscoelastic shear stress τ_{visco} and slope $\mathrm{d}\tau_{visco}/\mathrm{d}\gamma$.

(b) Viscoelastic damping curve.

Figure 3.9.: Viscoelastic shear stress τ_{visco} and slope $\mathrm{d}\tau_{visco}/\mathrm{d}\gamma$ for [NF]-mode at $\gamma = 0.5$.

stresses $\tau_{inel}^{(R)}$ but not for determination of the true strain-energy. In fact, we cannot derive the true strain-energy function for the pseudo Maxwell-material but a theoretical approach for calculation of stresses. We simply build a single equation in order to design a theoretical approach for defining $\Psi_{inel}^{(R)}$ in terms of the momentary amount of shear γ and the previous loading peak Γ as

$$
\begin{aligned}
\Psi_{inel}^{(R)} &= \int_{\Gamma}^{\gamma} \sqrt{\tau_{inel}^{(R)}{}' \tau_{inel}^{(R)}{}''}\,\mathrm{d}\widetilde{\gamma} \\
&= \int_{\Gamma}^{\gamma} \sqrt{\frac{1}{8}\mu_r^{(R)} c_r^{(R)} \widetilde{\gamma}^4 (\dot{\gamma})^2}\,\mathrm{d}\widetilde{\gamma}\,, \qquad \text{with} \qquad \mu_i^{(R)} = \sqrt{\frac{1}{8}c_r^{(R)}\mu_r^{(R)}} \\
&= \int_{\Gamma}^{\gamma} \left(\mu_i^{(R)}\widetilde{\gamma}^2 \dot{\gamma} \right)\,\mathrm{d}\widetilde{\gamma} \\
&= \frac{1}{3}\mu_i^{(R)}\left(\widetilde{\gamma}^3 \dot{\gamma}\big|_{\Gamma}^{\gamma} - \int_{\Gamma}^{\gamma} \left(\widetilde{\gamma}^3 \underbrace{\frac{\mathrm{d}\dot{\gamma}}{\mathrm{d}\widetilde{\gamma}}}_{=0} \right)\mathrm{d}\widetilde{\gamma} \right) \qquad \text{(see Eq. (3.42))} \\
&= \frac{1}{3}\mu_i^{(R)}\left(\gamma^3 - \Gamma^3 \right)\dot{\gamma} \\
&= \frac{1}{3}\mu_i^{(R)}\gamma^3\dot{\gamma} - \Psi_{inel}^{(R)}(\Gamma)\,.
\end{aligned}
\tag{3.66}
$$

Apparently, the restructuring effect is history dependent. The underlying mechanism of restructuring is shown in Fig. 3.11. Restructuring is an history dependent effect based on the current and referential configuration of momentary and preceding loading cycles, respectively. Thus, the restructuring follows a continuous changing configuration via $\Omega_0 \to \Omega' \to \Omega'' \to \Omega_0'$.

Equation (3.66) enables us to build a general approach for model the restructuring effect
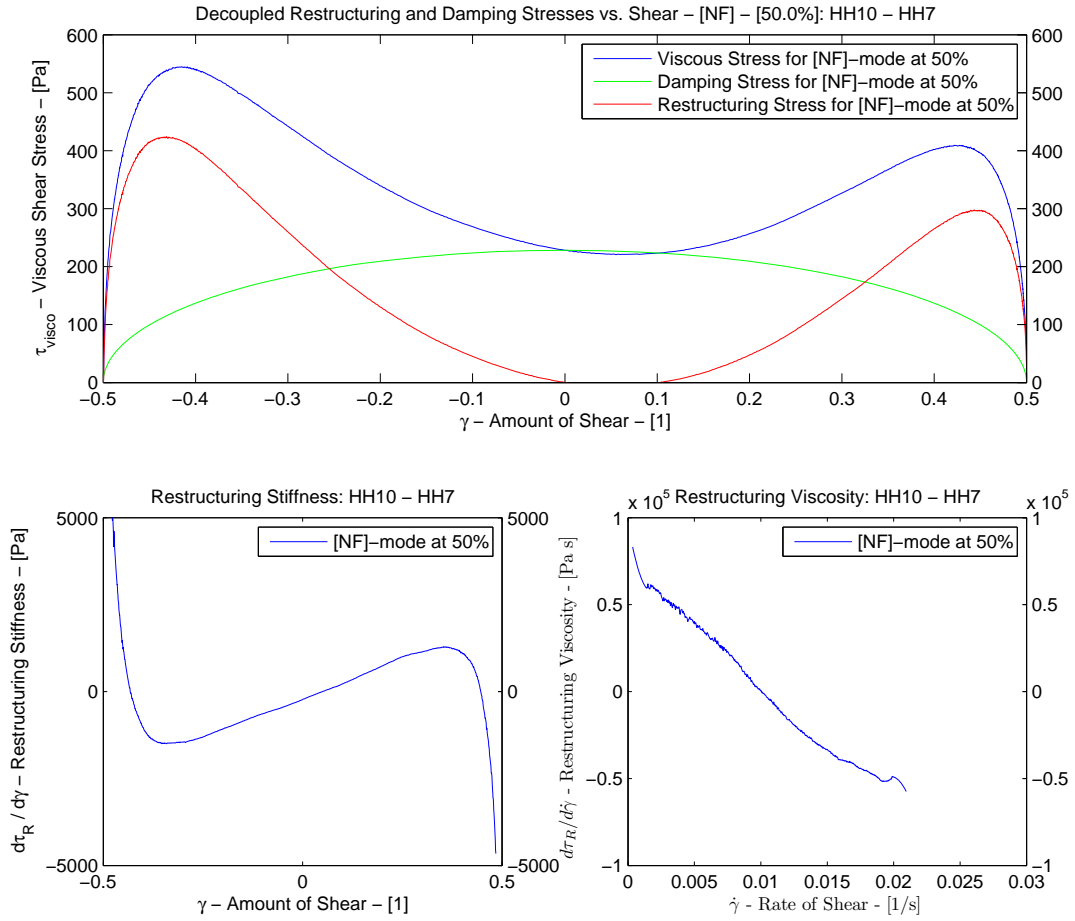
Figure 3.10.: Restructuring shear stress extracted $\tau_{visco}^{(R)}$ and slope $\mathrm{d}\tau_{visco}/\mathrm{d}\gamma$ for [NF]-mode at $\gamma = 0.5$.
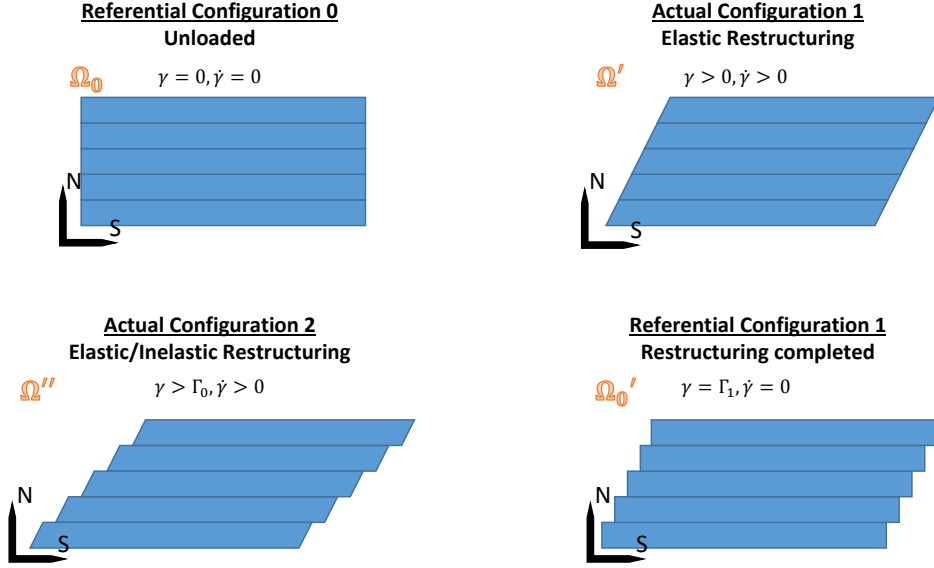
Figure 3.11.: Scheme of 'restructuring' during different loading patterns.

with introducing the rate dependent stiffness $E_i^{(R)}$ which defines the total restructuring stress via

$$
\begin{aligned}
\tau_{inel}^{(R)} &= \frac{\partial \Psi_{inel}^{(R)}}{\partial \gamma} = \mu_i^{(R)} \gamma^2 \dot{\gamma} \\
&= \underbrace{\left(\mu_i^{(R)} \dot{\gamma} \right)}_{E_i^{(R)} = f(\dot{\gamma})} \gamma^2 = E_i^{(R)}(\dot{\gamma})\, \gamma^2 \,.
\end{aligned}
\tag{3.67}
$$

Summed up, we designed a quadratic spring with a rate dependent stiffness $E_i^{(R)}$. Furthermore, the theoretical approach for the viscoelastic/inelastic restructuring strain energy $\Psi_{inel}^{(R)}$ cannot become negative neither for loading nor for unloading cycles. For the first loading cycle $\Psi_{inel}^{(R)}$ is positive due to $\gamma\dot{\gamma} > 0$ with $\Gamma = 0$ and for the first unloading cycle ($\gamma\dot{\gamma} < 0$ and $\gamma < \Gamma$) the restructuring strain-energy $\Psi_{inel}^{(R)} = \frac{1}{3}\mu_i^{(R)} \left(\gamma^3 - \Gamma^3 \right) \dot{\gamma}$ is also positive because $(\gamma^3 - \Gamma^3)\dot{\gamma} \geq 0$. In fact, we neglect that the rate of shear also influences the integration term. Fortunately, through integration and derivation by $\mathrm{d}\gamma$ we do not loose any information. In order to prove that the restructuring strain-energy is always positive we use the second law of thermodynamics. The dissipation for the pseudo Maxwell-material is given via

$$
\begin{aligned}
\Delta &= \tau_{inel}^{(R)} \dot{\gamma} \\
&= \underbrace{\mu_i^{(R)}}_{\geq 0} \underbrace{\gamma^2}_{\geq 0} \underbrace{\dot{\gamma}^2}_{\geq 0} \geq 0 \,.
\end{aligned}
\tag{3.68}
$$

Consequently, the total restructuring energy for sinusoidal application of shear is shown

(a) Dissipation for FS-mode loading.

(b) True restructuring energy for FS-mode loading.
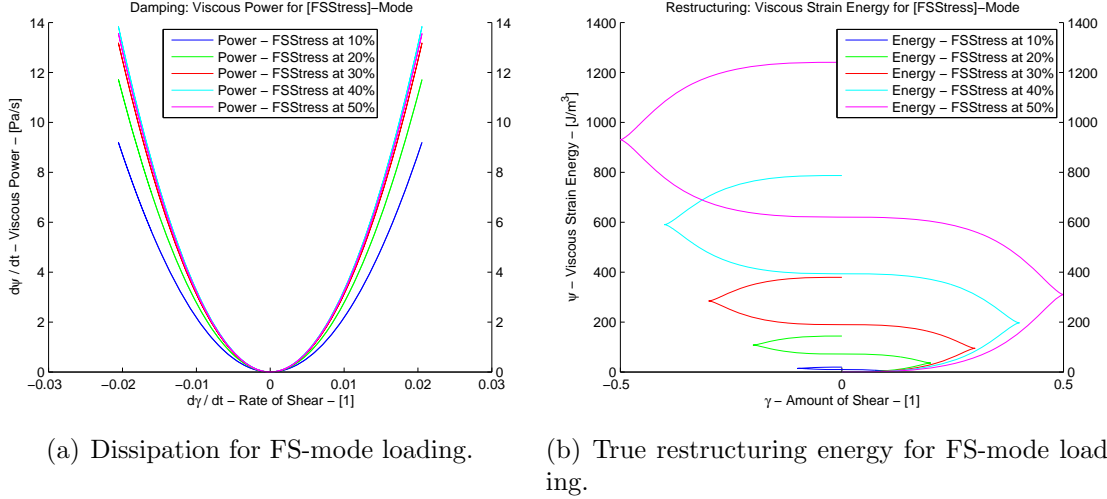
Figure 3.12.: Prove for fulfilled second law of thermodynamics saying $\Delta \geq 0$.

in Fig. 3.12(b) (parameters taken from Table 4.8) and can be calculated via

$$\Psi_{inel,true}^{(R)}(t) = \int \left(\mu^{(R)} \gamma^2 \dot{\gamma}^2 \right) \mathrm{d}t \,. \tag{3.69}$$

This means that during loading cycles the tissue is restructured and needs energy to do so but for unloading cycles the restructured tissue has a new referential configuration which is considered with $\Psi_{inel}^{(R)}(\Gamma)$. This may results from sliding sheets next to each other reducing the necessary amount of energy for unloading. The total amount of energy in fact can also never be negative as the restructuring effect adds up to the total strain energy $\Psi_{isoc} = \Psi_{elast} + \Psi_{inel}^{(R)} + \Psi_{inel}^{(D)}$.

Consequently, the viscoelastic/inelastic strain-energy function $\Psi_{inel}^{(R)}$ is a polynomial function of γ and $\dot{\gamma}$. A general form can be written as

$$\begin{aligned}
\Psi_{inel}^{(R)} &= \frac{1}{N} \sum_{i=m,f,s,fs} \mu_i^{(R)} \left\{ (\bar{I}_i - a_i)^{n_i} \frac{\mathrm{d}}{\mathrm{d}t} \left[(\bar{I}_i - a_i)^{n_i} \right] \right\} \\
&= \frac{1}{N} \sum_{i=m,f,s,fs} \mu_i^{(R)} \left[n_i (\bar{I}_i - a_i)^{(2n_i - 1)} \dot{\bar{I}}_i \right] .
\end{aligned} \tag{3.70}$$

A specific form of the restructuring model with $I_m = I_1$, $I_f = I_4$, $I_s = I_6$, $I_{fs} = I_8$ as well as $a_i = (3, 1, 1, 0)$, $n_i = (1, 2, 2, 2)$ and $N = 4$ is given through

$$\Psi_{inel}^{(R)} = \frac{1}{4} \left(\mu_m^{(R)} (\bar{I}_1 - 3) \dot{\bar{I}}_1 + 2\mu_f^{(R)} (\bar{I}_4 - 1)^3 \dot{\bar{I}}_4 + 2\mu_s^{(R)} (\bar{I}_6 - 1)^3 \dot{\bar{I}}_6 + 2\mu_{fs}^{(R)} (\bar{I}_8)^3 \dot{\bar{I}}_8 \right) . \tag{3.71}$$

Using this strain-energy function we can derive the shear stress for FS-mode with

$$\tau_{inel,FS}^{(R)} = \frac{1}{2} \gamma_{FS}^2 \dot{\gamma}_{FS} \left(2\mu_m^{(R)} + 12\gamma_{FS}^4 \mu_f^{(R)} + 3\mu_{fs}^{(R)} \right) . \tag{3.72}$$

Summed up, we can combine both restructuring and simple-damping models from Eq. (3.54) to which we will refer to as 'ResDamp-MaFiSh' (Restructuring-Damping including matrix-fiber-sheet coupling) in the following sections, with following characteristics:

- restructuring
  - fiber orientation influences damping effects
  - sliding of fibers and sheets next to each other cause reconfiguration
  - $\rightarrow$ damping effects are distorted and lowered during 'restructuring'
- damping
  - fibers are oriented
  - caused by the sliding of sheets next to each other
  - $\rightarrow$ linear 'damping' approach

3.4.4. General Model for Viscoelasticity/Inelasticity

In Sec. 3.4.3 we have obtained a special approach for modeling the viscoelstic/inelastic effects of myocardial tissue. Based on Eq. (3.54) the damping power function $\dot{\Psi}_{inel}^{(D)}$ can be generalized by using exponential functions rather than polynomials. Therefore, we introduce the time-pseudo invariant $\dot{\bar{I}}_1^*$ including its normalization by

$$\dot{\bar{I}}_i^* = \frac{1}{2}\frac{\dot{\bar{I}}_i}{\sqrt{\bar{I}_1 - 3}} \, . \tag{3.73}$$

A proposal for the damping effects is given by an exponential strain-power function model using a viscous nonlinearity parameter $b_i^{(D)}$ defined by

$$\begin{aligned}
\dot{\Psi}_{inel}^{(D)} = {} & \frac{\mu_m^{(D)}}{2b_m^{(D)}}\left[\exp\left(b_m^{(D)}\dot{\bar{I}}_1^{*2}\right) - 1\right] \\
& + \frac{\mu_f^{(D)}}{2b_f^{(D)}}\left[\exp\left(b_f^{(D)}\dot{\bar{I}}_4^{*2}\right) - 1\right] \\
& + \frac{\mu_s^{(D)}}{2b_s^{(D)}}\left[\exp\left(b_s^{(D)}\dot{\bar{I}}_6^{*2}\right) - 1\right] \\
& + \frac{\mu_{fs}^{(D)}}{2b_{fs}^{(D)}}\left[\exp\left(b_{fs}^{(D)}\dot{\bar{I}}_8^{2}\right) - 1\right] \, .
\end{aligned} \tag{3.74}$$

Note. Applying derivatives $\partial\dot{\Psi}_{inel}^{(D)}/\partial\dot{\mathbf{C}}$ and setting $b_i^{(D)} = 0$ will result to the same stresses as proposed via the 'Simple-Damping' model given via Eq. (3.54).

Furthermore, a general model representing the restructuring terms can be created via

$$
\begin{aligned}
\Psi_{inel}^{(R)} = {} & \frac{\mu_m^{(R)}}{4b_m^{(R)}} \dot{\bar{I}}_1 \left\{ \exp\left[b_m^{(R)}(I_1 - 3) \right] - 1 \right\} \\
& + \frac{\mu_f^{(R)}}{4b_f^{(R)}} \dot{\bar{I}}_4 \left\{ \exp\left[b_f^{(R)}(I_4 - 1)^2 \right] - 1 \right\} \\
& + \frac{\mu_s^{(R)}}{4b_s^{(R)}} \dot{\bar{I}}_6 \left\{ \exp\left[b_s^{(R)}(I_6 - 1)^2 \right] - 1 \right\} \\
& + \frac{\mu_{fs}^{(R)}}{4b_{fs}^{(R)}} \dot{\bar{I}}_8 \left\{ \exp\left[b_{fs}^{(R)} I_8^2 \right] - 1 \right\} .
\end{aligned}
\tag{3.75}
$$

Both Eqs. (3.74) and (3.75) are based on the same mechanics as their simple versions proposed in Sec. 3.4.3. Unfortunately, neither of those two models can describe the viscoelastic/inelastic behavior isolated but only both of them united can describe the viscoelastic/inelastic biomechanics of myocardium. The major problem is that the combined model has 16 parameters in total. Therefore, it will be nearly impossible to find a unique parameter set marking the global minimum by using an objective function minimization algorithm. Consequently, we keep focus on the simple versions of the 'damping' and 'restructuring' effects as proposed in Sec. 3.4.3.

3.5. Modeling of Tissue-Softening

Emery et al. [11] has suggested that displacement of adjacent muscle layers as well as disruption of perimysial collagen fibers could be possible causes for softening. In order to evaluate the relative softening $\zeta^{(R)}$ we introduce the following algorithm.

Determination of relative softening

1. Fit mean of preconditioned experimental data for every loading cycle $i = 1, 2, .. 5$ with reference to loading cycles $\hat{\gamma} = 0.1, 0.2, .., 0.5$.

2. Create simulation stress data τ_i with fitted parameters from all loading cycles i but stop at $\hat{\gamma} = 0.1$.

3. Calculate temporary softening $z_{i+1}(\gamma) = (1 - \tau_{i+1}(\gamma)/\tau_i(\gamma))$ for $\gamma = 0 - 0.1$ and every loading mode FS, FN, SF, SN, NF and NS.

4. Compute softening $\zeta_{i+1}^{(R)} = \bar{z}_{i+1}(\gamma)$ for every loading mode FS, FN, SF, SN, NF and NS.

The relative softening shows how softening propagates referred to the first main loading cycle. Nevertheless, the first main loading cycle has precursive preconditioning cycles and, thus, the first main loading cycle is already affected by reorientation and softening. Consequently, we need to determine the initial state of tissue.

The absolute softening $\zeta^{(A)}$ can be obtained by comparing the mean elastic stresses for all cycles $\hat{\gamma} = 0.1, 0.2, .., 0.5$ in the range of $|\gamma| \leq 0.1$. Therefore, the mean of elastic stresses is fitted with the 'ALIGNED' and 'KAPPA' models which build the basis for determination of the absolute softening. The absolute softening is modeled via an exponential function representing the reduction of an unsoftened strain- energy function Ψ_0 via including a history parameter Γ [23]. For simplification we apply a multiplicative term reading $\Psi = [1 - \zeta^{(A)}(\Gamma)]\Psi_0$. The absolute isotropic softening $\zeta_{iso}^{(A)}$ is modeled as a simple exponential function with softening parameter s per loading cycle step through

$$\zeta_{iso}^{(A)}(\Gamma) = 1 - e^{-s\Gamma} \,. \tag{3.76}$$

Note. The given softening function describes the isotropic softening for the current loading peak $\hat{\gamma}$ with preceding preconditioning at same loading peaks. Consequently, the history variable Γ is equal to the current loading peak $\hat{\gamma}$ for this special loading pattern.

The Cauchy stress tensor including softening effects is given by

$$
\begin{aligned}
\boldsymbol{\sigma}_\Gamma &= 2J^{-1}\mathbf{F}\frac{\Psi(\mathbf{C}, \Gamma)}{\mathbf{C}}\mathbf{F}^{\mathrm{T}} \\
&= \underbrace{2J^{-1}\mathbf{F}\frac{\Psi_0(\mathbf{C})}{\mathbf{C}}\mathbf{F}^{\mathrm{T}}}_{=\boldsymbol{\sigma}_0}\left[1 - \zeta_{iso}^{(A)}(\Gamma)\right] \\
&= \boldsymbol{\sigma}_0 e^{-s\Gamma} \,.
\end{aligned}
\tag{3.77}
$$

Finally, we obtain the absolute softening as special form of relative softening of tissue regarding an unstressed tissue as reference with

$$\boldsymbol{\sigma}_\Gamma \boldsymbol{\sigma}_0^{-1} = \mathbf{I}\left[1 - \zeta_{iso}^{(A)}(\Gamma)\right] \,. \tag{3.78}$$

Assuming, we know the unsoftened Cauchy stress tensor $\boldsymbol{\sigma}_0$ and the current Cauchy stress tensor $\boldsymbol{\sigma}_\Gamma$ one can derive the isotropic softening function via

$$\zeta_{iso}^{(A)}(\Gamma) = 1 - \frac{1}{3}\left(\boldsymbol{\sigma}_\Gamma \boldsymbol{\sigma}_0^{-1} : \mathbf{I}\right) = 1 - \frac{1}{3}\mathrm{tr}(\boldsymbol{\sigma}_\Gamma \boldsymbol{\sigma}_0^{-1}) \,. \tag{3.79}$$

Hence, we modify Eq. (3.79) to describe the relative softening using $\boldsymbol{\sigma}_1$ via

$$\zeta_{iso}^{(R)}(\Gamma) = 1 - \frac{1}{3}\left(\boldsymbol{\sigma}_\Gamma \boldsymbol{\sigma}_1^{-1} : \mathbf{I}\right) = 1 - \frac{1}{3}\mathrm{tr}(\boldsymbol{\sigma}_\Gamma \boldsymbol{\sigma}_1^{-1}) \,. \tag{3.80}$$

Following Eqs. (3.79) and (3.80) modeling of softening requires several tests at different loads in order to design softening functions. Within the scope of this thesis, we focus on modeling softening via Eq. (3.77).

As this approach on determination of softening fails when $\boldsymbol{\sigma}$ is unknown or only elements are known, we simplify the testing scenario and assume identical softening for every loading mode FS, FN, SF, SN, NF and NS at same Γ. Hence, we find the following algorithm for modeling softening via

Determination of absolute softening

1. Fit mean of elastic experimental data for every loading cycle $i = 1, 2, .. 5$ with reference to loading cycles $\hat{\gamma} = 0.1, 0.2, .., 0.5$ with model 'KAPPA'.

2. Create simulation stress data τ_i^l with fitted parameters from all loading cycles i but stop at $\hat{\gamma} = 0.1$ for all loading modes $l =$ FS, FN, SF, SN, NF and NS.

3. Calculate mean via $\tau^l(\Gamma) = \text{Mean}_i(\tau_i^l(\gamma))$ for $\gamma = 0 - 0.1$ at history shear Γ and every loading mode $l =$ FS, FN, SF, SN, NF and NS.

4. Calculate mean of all loading modes $\bar{\tau}(\Gamma) = \text{Mean}_l(\tau^l(\Gamma))$

5. Apply nonlinear fit (using NLINFIT() in Matlab®) on $\bar{\tau}(\Gamma)$ with function $\bar{\tau}(\Gamma) = \bar{\tau}(0)\exp(-s\Gamma)$ and determine unsoftened stress $\bar{\tau}(\Gamma = 0)$ and softening parameter s.

6. Normalize and find softening function $\zeta^{(A)}(\Gamma) = 1 - \bar{\tau}(\Gamma)/\bar{\tau}(0)$.

If wished, step 4 can be omitted and thus we can determine the softening for all loading modes l.

4. Results

4.1. Data Analysis

All in all, 32 different hearts have been investigated undergoing 37 tests with BDM myosin ATPase inactivation conditions and 10 tests without inactivation. In total, $N_{TOT} = N_{BDM} + N_{BDM,bad} + N_{NOBDM} = 426 + 69 + 134 = 629$ files of triaxial shear data have been analyzed. A test is defined through the identifier of the heart (HH## ... human heart plus id), location of extracted specimen (ventricle type: RV/LV, radial location: endocardial/myocardial/epicardial and longitudinal direction: base/equator/apex), type of loading (FN, FS, SF, SN, NF or NS) and peak of shear ($\hat{\gamma} = 10\% - 50\%$).

In general, two different testing results can be obtained. Some initial test have been carried without the usage of BDM-inactivation which leads to activated myocardial stiffening. In Figure 4.1 the influence of inactivation is shown where Figs. 4.1(a) and 4.1(b) correspond to the active and passive mechanical stress response to simple shear, respectively. No usage of BDM leads to massive increase in stiffness and hysteresis which is unfavorable for passive myocardial testing aims as all proposed models neglect the electromechanical activation in the tissue. In addition, in Figs. 4.2 and 4.3 the influence of BDM-usage on viscous strain-energy is shown for BDM-inactivated and no usage of BDM, respectively. The suggested trend lines in the diagrams show that due to BDM-inactivation no direct coupling between viscous strain-energy and rate of shear is present. In contrast, no BDM-usage shows a connection of decreasing viscous strain-energy with higher rates of shear. In summary, hysteresis is unaffected by rate of shear for BDM-inactivated myocardial tissue but this seems not to be the case for non-inactivated myocardial tissue. A reason for this may be the fact that activated actin-myosin networks react to faster movement with contraction causing the whole myocardium to behave more elastic and less viscous. Therefore, we concentrate on the BDM-inactivated hearts for testing and modeling.

In Fig. 4.4 for all BDM-inactivated hearts the performed test scenarios are shown. Most tests have been carried out with same peak rates $\dot{\hat{\gamma}}$ of shear within same hearts but differ between hearts. Fortunately, modeling is based on actual values of amount of shear and momentary rate of shear whereas design of complete simulation cycles are based on the average rate of shear over all hearts in order to construct a complete simulation cycle (see Sec. 3.4.3).

In Table 4.1 the number of tests per BDM-treated heart are shown. Normally, for every heart six tests should be carried out containing all six loading modes. For hearts HH11,
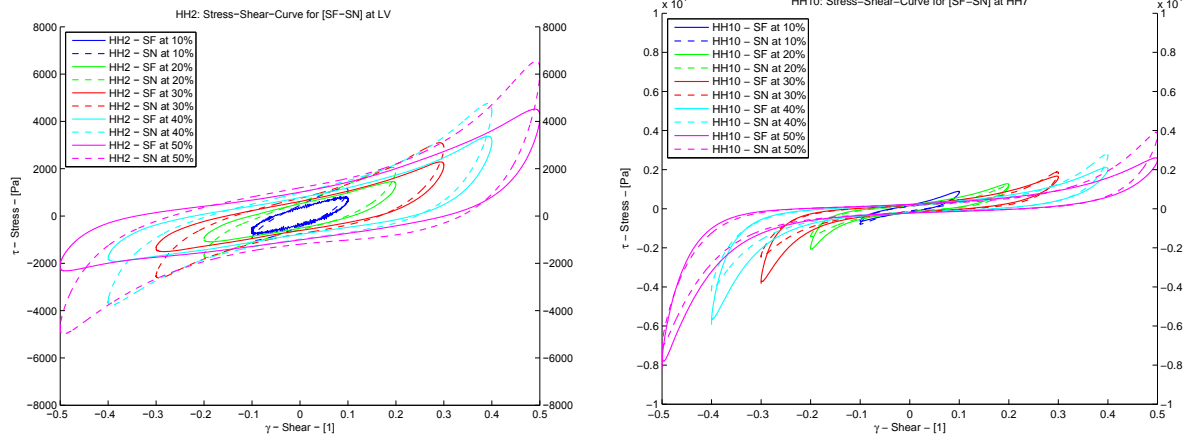
(a) HH2 shear hysteresis without BDM-inactivation.

(b) HH10 shear hysteresis with BDM-inactivation.

Figure 4.1.: Comparison between without and with BDM-inactivation.
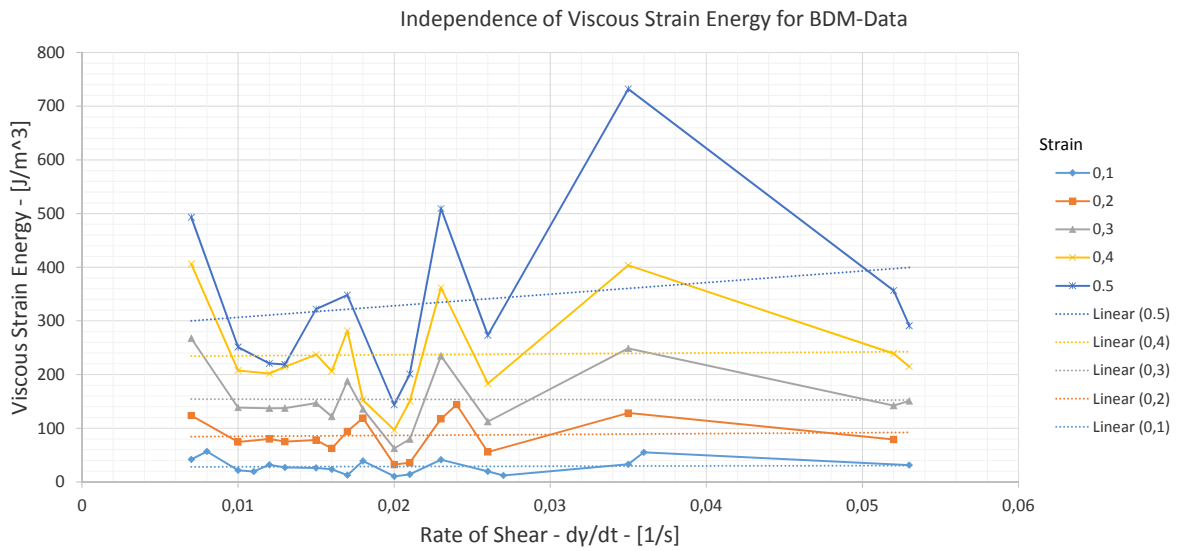
Figure 4.2.: Viscous strain-energy versus rate of shear with usage of BDM.
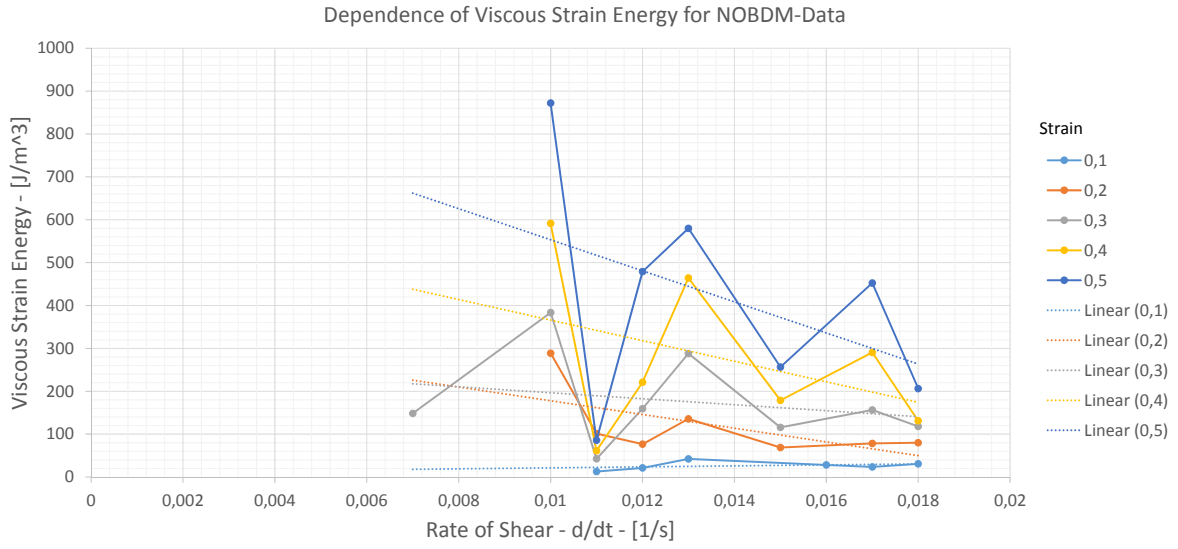
Figure 4.3.: Viscous strain-energy versus rate of shear without usage of BDM.
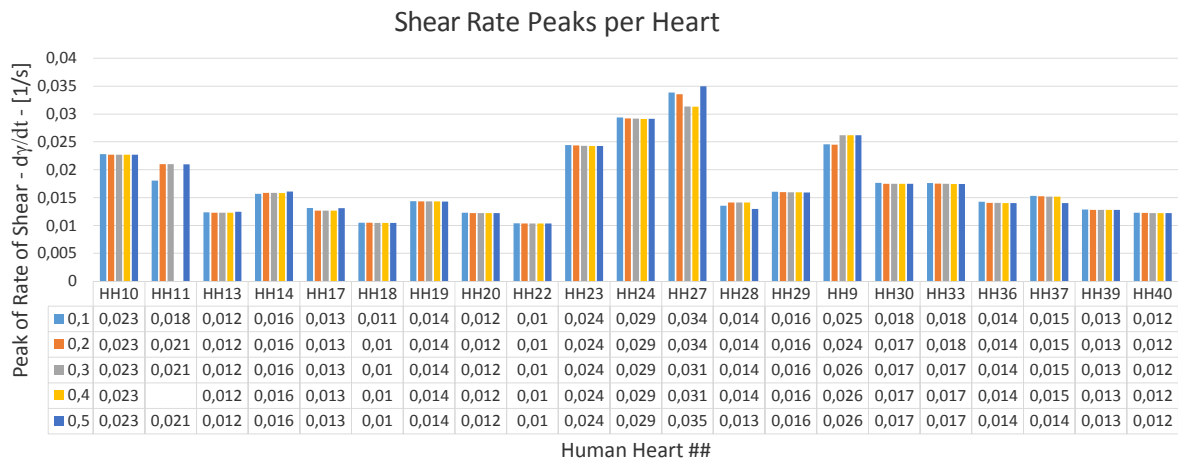
Figure 4.4.: Peak values of shear-rate $\dot{\hat{\gamma}}$ for every BDM-inactivated heart.

Table 4.1.: Number of performed tests for every human heart identifier (HH##).

Peak Strain γ	0.1	0.2	0.3	0.4	0.5	Total
HH10	6	6	6	6	6	30
HH11	4	2	2		2	10
HH13	10	10	10	10	8	48
HH14	7	8	8	8	7	38
HH17	10	12	12	12	2	48
HH18	6	6	6	6	4	28
HH19	6	6	6	6	6	30
HH20	6	6	6	6	6	30
HH22	6	6	6	6	6	30
HH23	6	6	6	6	6	30
HH24	6	6	6	6	6	30
HH27	12	12	12	12	6	54
HH28	18	24	24	24	16	106
HH29	24	24	24	24	18	114
HH30	6	6	6	6	4	28
HH33	12	12	12	12	12	60
HH36	4	4	4	4	4	20
HH37	6	6	6	6	4	28
HH39	6	6	6	6	6	30
HH40	6	6	6	6	6	30
HH9	6	6	6	6	6	30
Total	173	180	180	178	141	852

HH17, HH18, HH30, HH36 and HH37 this could not be realized because of problems during testing, e.g. collision with objects, rupture, program errors or problems with machine calibration.

Unfortunately, only eleven hearts are appropriate for modeling itself due to a various number of failures during testing. In some cases, the [NF-NS] stresses are showing higher stress values than in the [FN-FS]-directions which is impossible from a mathematical and biomechanical based point of view. All proposed models shall fulfill the condition

$$\sigma_{FS} > \sigma_{FN} > \sigma_{SF} > \sigma_{SN} > \sigma_{NF} = \sigma_{NS}, \qquad (4.1)$$

as proposed by Dokos et al. [9] (see Fig. 4.15). Therefore, the remaining appropriate hearts for modeling are HH10, HH29_SEP_1, HH36 and HH39 as well as HH11 (SF/SN-switch), HH14 (SF/SN-switch), HH24 (SF/SN-switch), HH28_SEP_1 (FS/FN-switch), HH29_LV_2 (SF/SN-switch), HH30 (FS/FN-switch) and HH33_LV (FS/FN-switch) where sometimes switching X/Y-modes is necessary to fulfill Eq. 4.1.
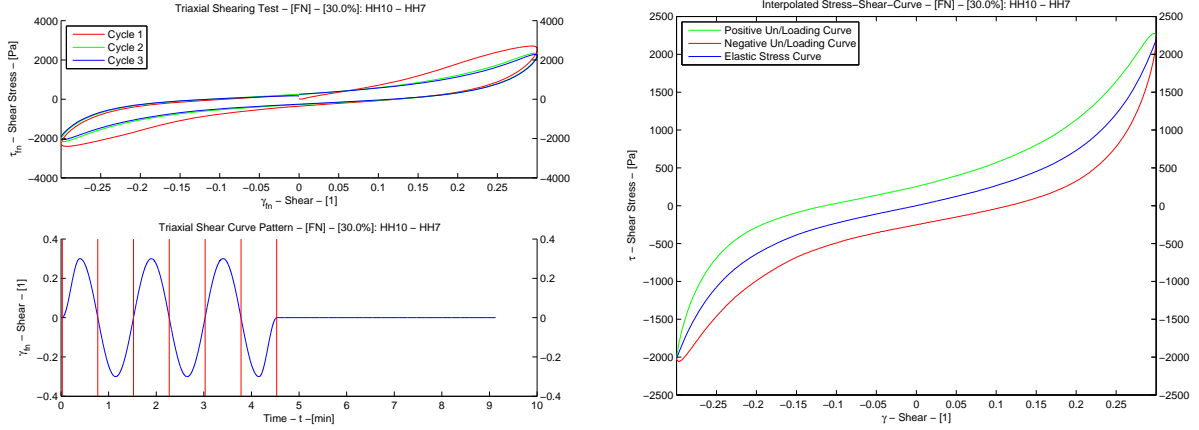
(a) Loading pattern for triaxial shear testing with two preconditioning cycles (red, green) and one main loading cycle (blue).

(b) Main loading cycle decoupled into elastic (blue) as well as upper (green) and lower (red) shear stress curves.

Figure 4.5.: Shear stress curves and loading pattern for HH10 at $\gamma = 0.3$

After reading and preparing all data files, data fitting can be used for the elastic and viscous stress parts. In Figures 4.5, 4.6, 4.7 and 4.8 exemplary plots for HH10 are shown. Viscoelastic slopes as well as elastic stiffness plots emphasize that myocardial tissue shows strong non-linearities. A procedure called preconditioning helps to limit the possible bias through microstructural disorder of tissue components. The difference of preconditioned versus unpreconditioned tissue is shown in Fig. 4.9 where preconditioned tissue is initially less stiffer and shows higher nonlinearity. Note, main loading cycle curves do not start from origin as the corresponding rate of shear is non-zero. Interestingly, stresses vary for positive ($\gamma > 0$) and negative ($\gamma < 0$) loading directions and are usually not symmetrically distributed, e.g. see Fig. 4.1(b). This phenomenon may result from imperfections in cube geometry causing a parallelepiped-like geometry. Thus, when load is applied the tissue could be compressed initially until the amount of shear is high enough to flip the geometry of the imperfect cube. At that moment, fibers are initially unstretched which may be the cause for unsymmetric stress curves. In order to correct this directional dependency the mean for positive and negative stress curves is computed. Attempts with using the stiffer curves resulted in selective data collection and is not applicable for data modeling and fitting as perfect cube geometries without prestretch or residual stresses are assumed.

Eventually, the difference between viscous and elastic stress terms can be found via observation of strain-energy curves. In Figs. 4.8(a) and 4.8(b) the strain-energy trend for $\Delta\gamma > 0$ is shown for viscous and elastic stresses, respectively. Remarkably, the viscous energy gradient $\Delta\Psi_{visco}$ is always positive for both unloading (red) and loading cycles (green) which means that energy is always consumed and never stored. This emphasizes the pure dissipative character of viscous stresses within the myocardium. In contrast, the elastic energy gradient $\Delta\Psi_{elast}$ is negative for unloading cycles as the tissue releases
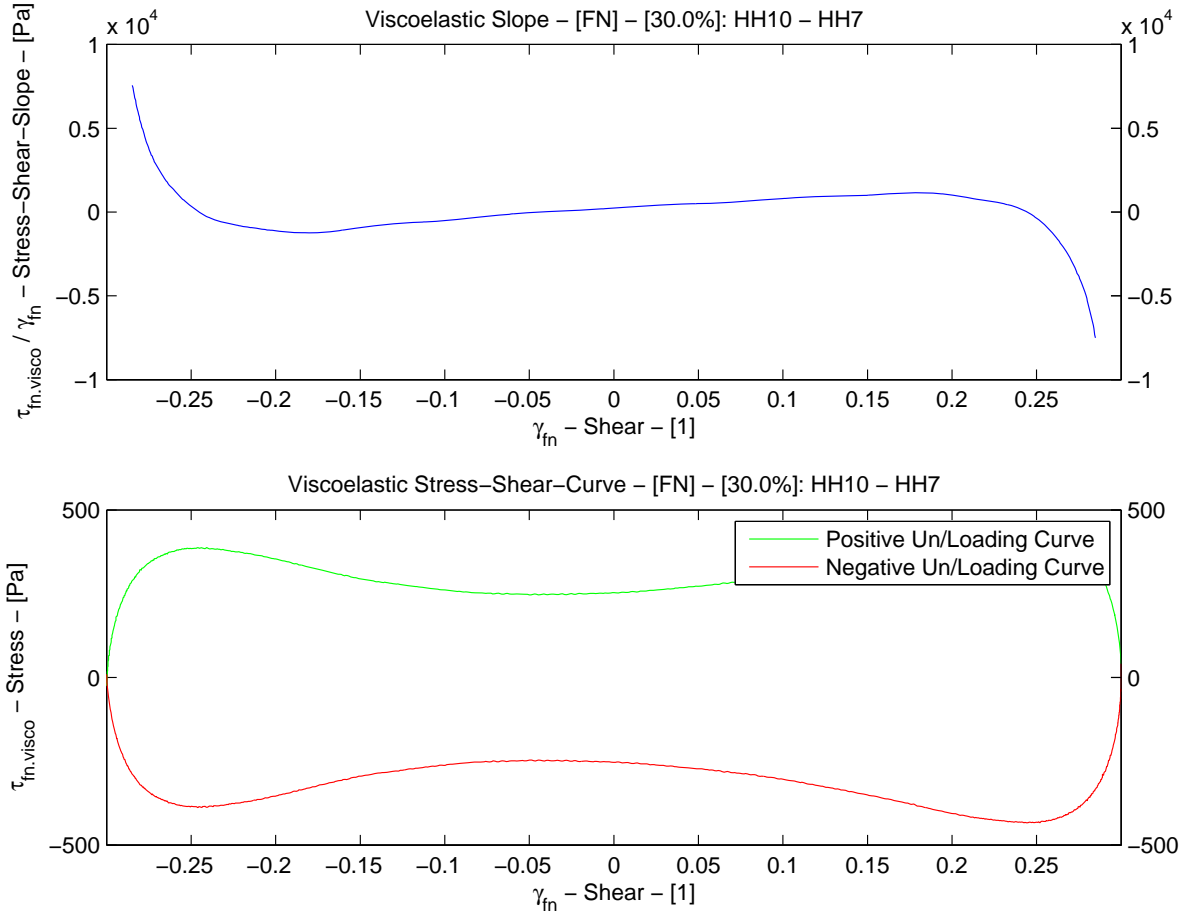
Figure 4.6.: Viscoelastic slopes (stiffness) for HH10 in FN-mode at $\gamma = 0.3$.
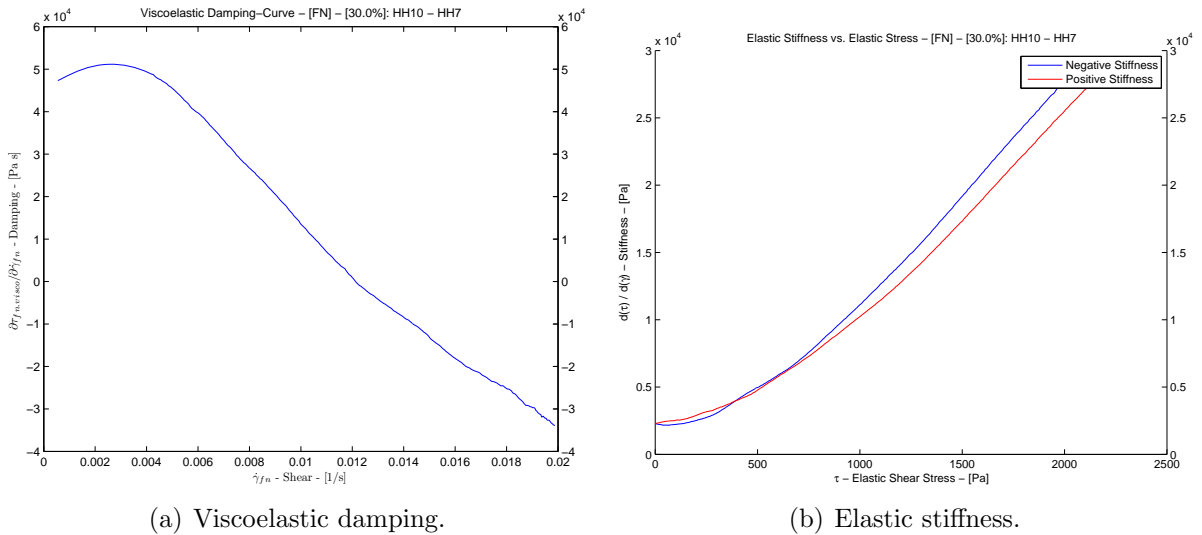
(a) Viscoelastic damping.

(b) Elastic stiffness.

Figure 4.7.: Viscous and elastic effects for HH10 in FN-mode at $\gamma = 0.3$.

(a) Viscous strain-energy.

(b) Elastic strain-energy.
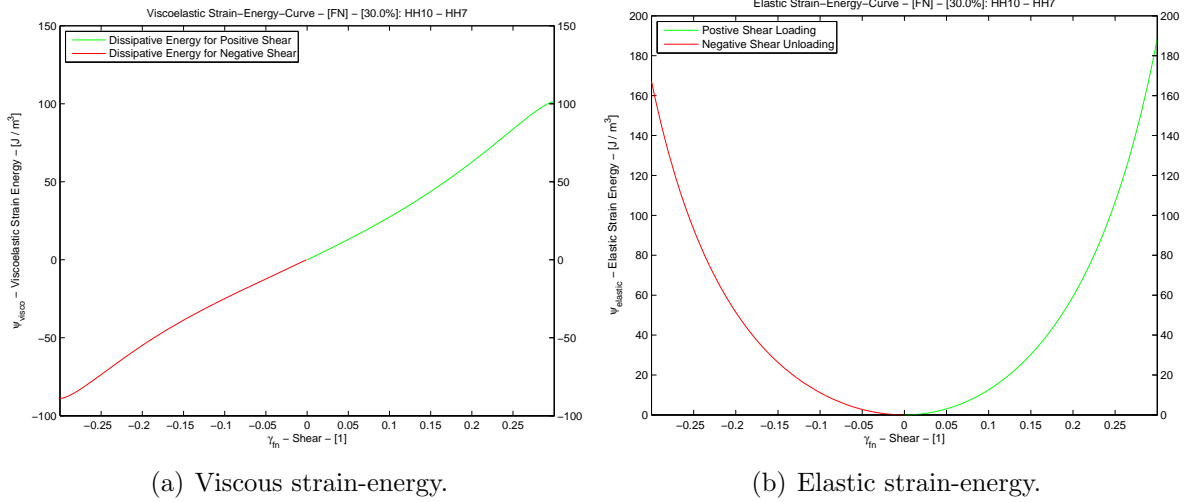
Figure 4.8.: Amount of strain-energy for HH10 in FN-mode at $\gamma = 0.3$.

stored energy from a previous loading cycle and vice versa.

Note.   In Fig. 4.8(a) the strain-energy becomes negative for negative amounts of shear. The reason for that comes per definition of the initial state reading $\Psi(\gamma = 0) = 0$. In fact, energy as well as dissipation are always positive.

Finally, we deduce that the mean elastic stresses for all observed hearts increase with higher amounts of shear (see Fig. 4.10). Differences arising from varying loading modes are obvious although the trends of stress increase resemble. When investigating the mean viscous stresses versus amount of shear these trends are only slightly to not present (see Fig. 4.11).

The resulting curves after data preparation and creating the mean of all eleven heart datasets we use the following hysteresis data for fitting (see Figs. 4.12(a), 4.12(b) and 4.12(c)). Decoupling of elastic and viscous stresses are shown in Figs. 4.13(a), 4.13(b), 4.13(c), 4.13(d), 4.13(e) and 4.13(f). As proposed by Dokos et al. [9] $FS > FN$, $SF > SN$ and $NF \approx NS$.

4.2. Parameter Fits for Existing Models

4.2.1. Hyperelastic Exponential Model Proposed by Costa

In Table 4.2 the parameter fits for the model proposed by Costa et al. [3] is listed. As the model is a single exponential function it lacks stiffness parameters for different compounds like ground substance, fibers, sheets or coupling effects. Thus, anisotropic effects are mainly described via various nonlinearity parameters b (see Fig. 4.14(a)). During the first loading cycle with $\hat{\gamma} = 0.1$ Costa's model proposes very high tissue
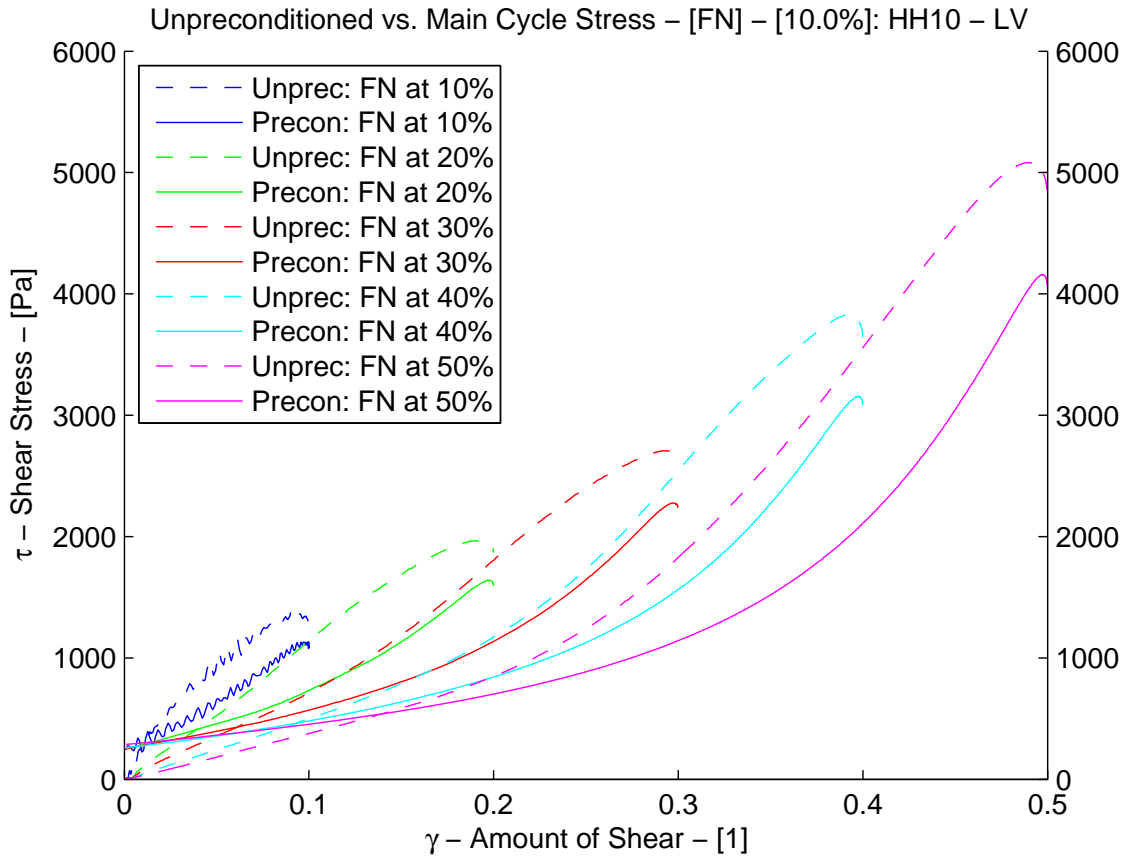
Figure 4.9.: Unpreconditioned versus main cycle stresses.
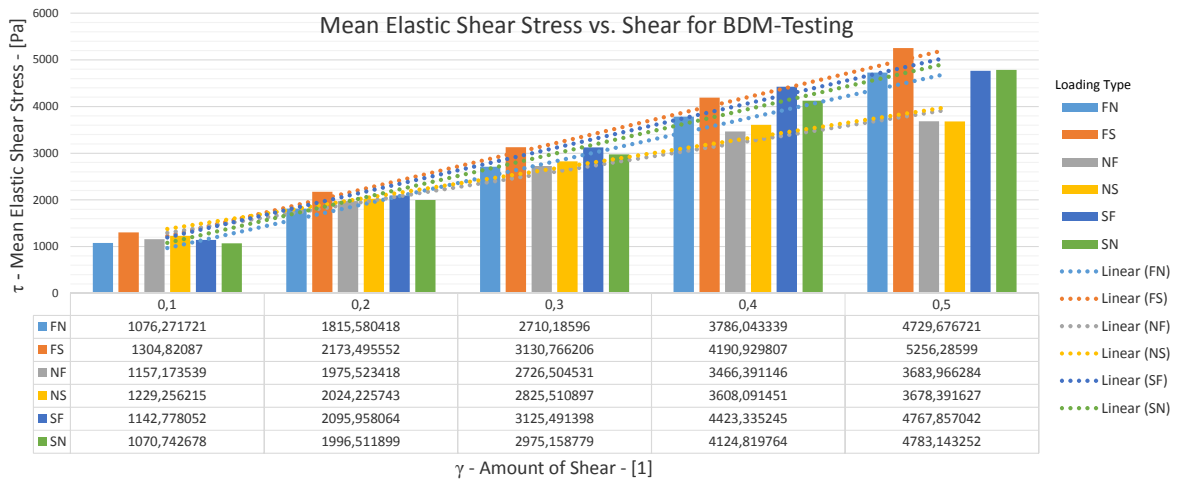
Figure 4.10.: Comparison of elastic shear stresses summarized for all hearts at different 'amount of shear'.
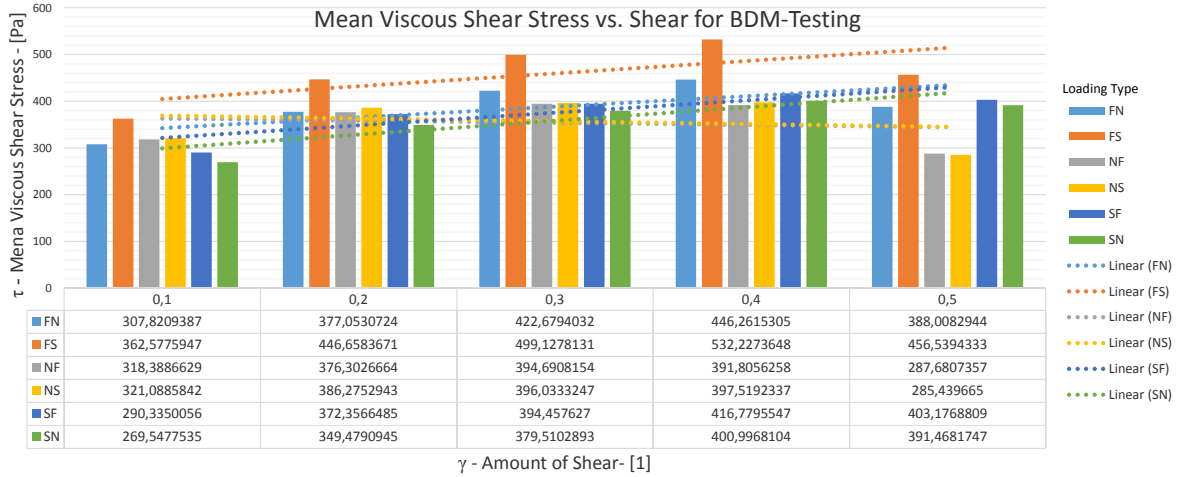
Figure 4.11.: Comparison of viscous shear stresses summarized for all hearts at different 'amount of shear'.

stiffness and low nonlinearities which changes for higher shear ranges to the opposite. As the drop from the first loading cycle the upcoming cycles is very high, the model seems to overestimate stiffness for low shear regions.

4.2.2. Hyperelastic Exponential Model Proposed by Schmid

In contrast to the Costa's model Schmid et al. [48] proposed a decoupled exponential function including stiffness parameters for different loading directions. As a matter of fact, Schmid's model also overestimates the stiffness parameters for the first loading cycle and shows nearly no nonlinearity (see Table 4.2). For the upcoming loading cycles Schmid's model shows little improvements over Costa's model (compare R^2 and see Fig. 4.14(b)). Nevertheless, the number of parameters makes data fitting difficult. In addition, the model does not directly assign parameters to tissue components but directions of applied load.

4.2.3. Hyperelastic Exponential Model with Perfect Fiber Alignment 'ALIGNED' by Holzapfel

The perfectly aligned fiber model is modeled as suggested by Holzapfel et al. [25]. In order to verify the given model, we try to reproduce the data fit parameters of the data from Dokos et al. [9]. In Table 4.3 we compare the fit results proposed by Holzapfel with the conducted fit as part of this thesis. Obviously, all parameters are similar except the matrix stiffness constant a. Investigations of the initial total stiffness $c_{it} = \mathrm{d}\tau/\mathrm{d}\gamma$ at zero strain $\gamma = 0$ shows that the stiffness term itself lies in the range of thousands of Pascals. Therefore, we conclude that the parameter a is properly fitted and the model is appropriate for further investigations and expansions. In fact, the initial total stiffness c_{it} also
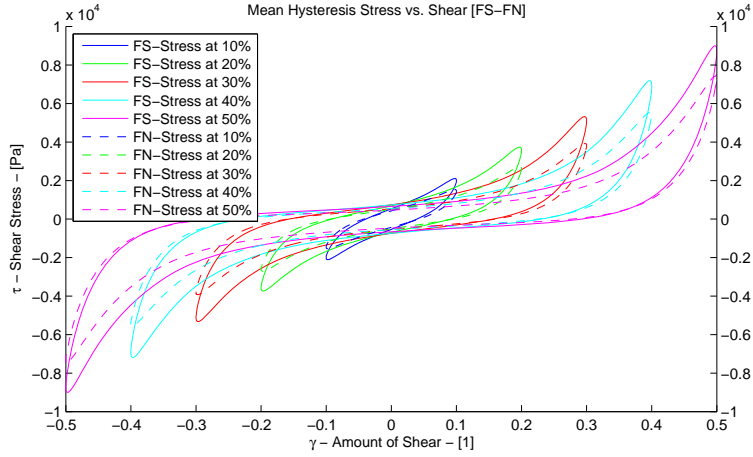
(a) Mean hysteresis curve for FS/FN-mode.
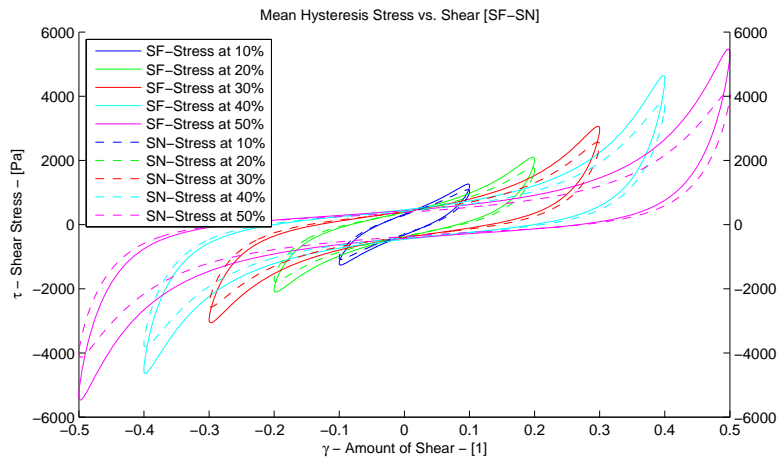
(b) Mean hysteresis curve for SF/SN-mode.
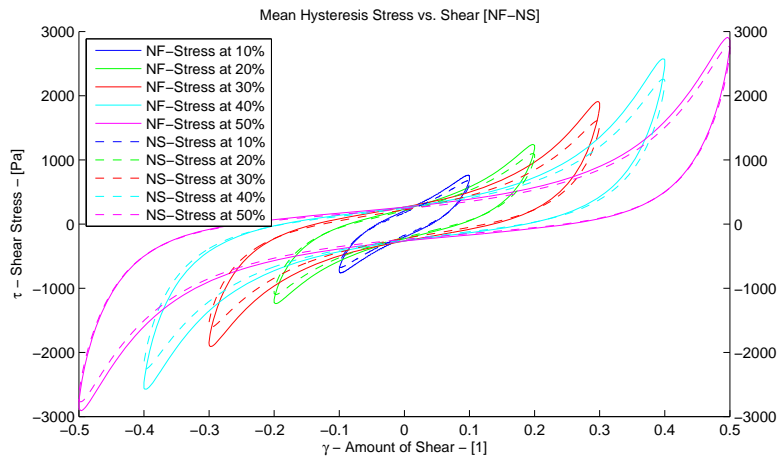
(c) Mean hysteresis curve for NF/NS-mode.

Figure 4.12.: Mean hysteresis curves used for fitting.
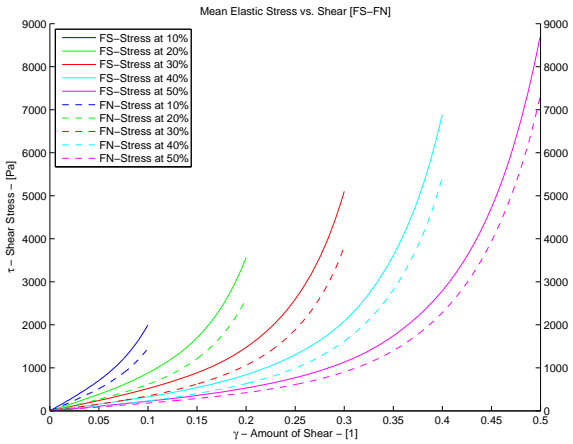
(a) Elastic FN/FS-stress.
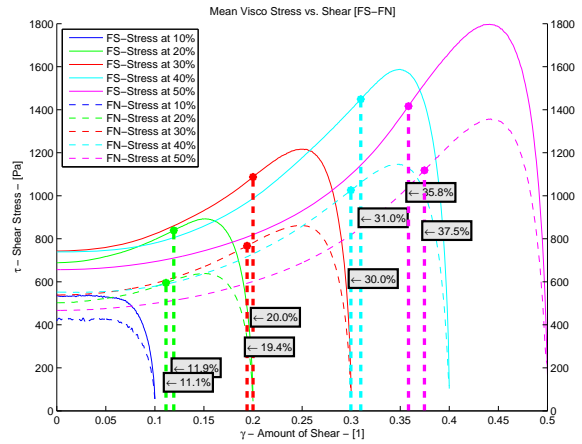
(b) Viscous FN/FS-stress.
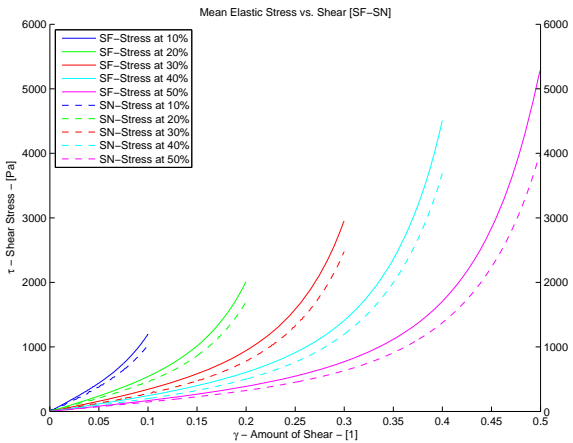
(c) Elastic SF/SN-stress.
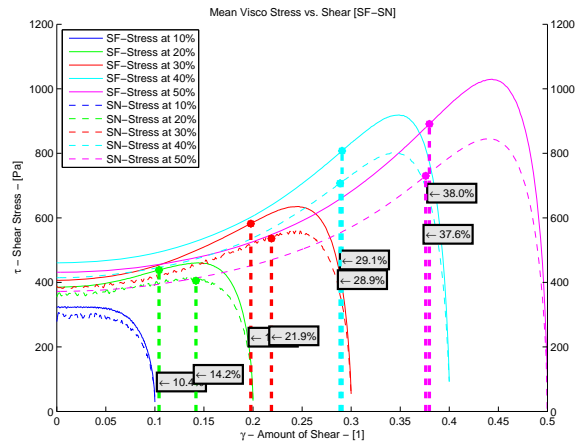
(d) Viscous SF/SN-stress.
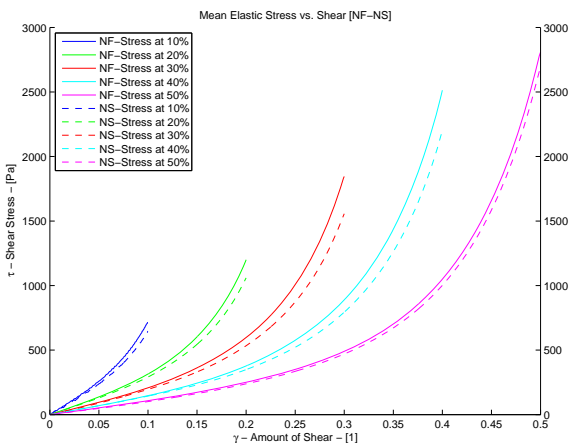
(e) Elastic NF/NS-stress.
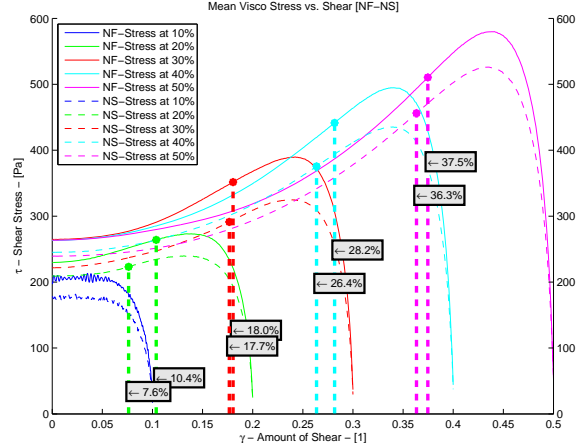
(f) Viscous NF/NS-stress.

Figure 4.13.: Elastic and viscous stress for mean of data.
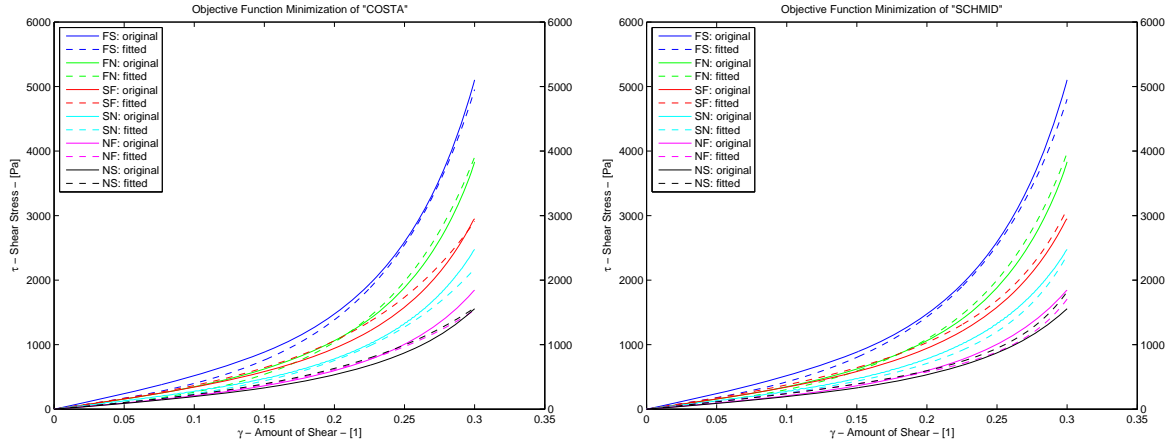
(a) Mean data fit for model 'COSTA' for $\hat{\gamma} = 0.3$. (b) Mean data fit for model 'SCHMID' for $\hat{\gamma} = 0.3$.

Figure 4.14.: Data fit curves for orthotropic models of Costa et al. [3] and Schmid et al. [48].

Table 4.2.: Parameter fit for model 'COSTA' and 'SCHMID'.

	Unit	SCHMID					COSTA				
$\hat{\gamma}$	[1]	0.1	0.2	0.3	0.4	0.5	0.1	0.2	0.3	0.4	0.5
R^2	[%]	96.95	98.27	99.03	99.53	99.72	97.09	98.51	99.08	99.61	99.90
a	[kPa]	321.9	1.446	0.696	0.565	0.550	-	-	-	-	-
a_{ff}	[kPa]	-	-	-	-	-	563.2	1.720	0.498	0.384	0.382
b_{ff}	[1]	6.410	302.3	188.8	100.9	57.42	3.621	262.8	277.3	145.6	77.37
a_{fs}	[kPa]	-	-	-	-	-	379.1	0.548	0.367	0.196	0.137
b_{fs}	[1]	0.029	3.630	4.641	3.682	2.451	0.051	19.46	18.43	21.97	20.21
a_{fn}	[kPa]	-	-	-	-	-	303.9	211.8	102.3	0.264	0.171
b_{fn}	[1]	0.019	2.055	2.778	2.445	1.666	0.040	0.032	0.046	12.47	13.12
a_{ss}	[kPa]	-	-	-	-	-	0.026	0.056	0.099	0.114	0.081
b_{ss}	[1]	1.759	122.2	101.6	68.79	38.20	15190	1794	461.1	196.2	106.2
a_{sn}	[kPa]	-	-	-	-	-	0.144	0.345	0.514	0.229	0.179
b_{sn}	[1]	0.020	2.255	2.883	2.412	1.509	78.96	19.57	8.730	14.11	12.84
a_{nn}	[kPa]	-	-	-	-	-	0	0.003	0.033	0.035	0.031
b_{nn}	[1]	0	55.29	64.76	44.18	27.05	0	0	626.9	246.1	121.1
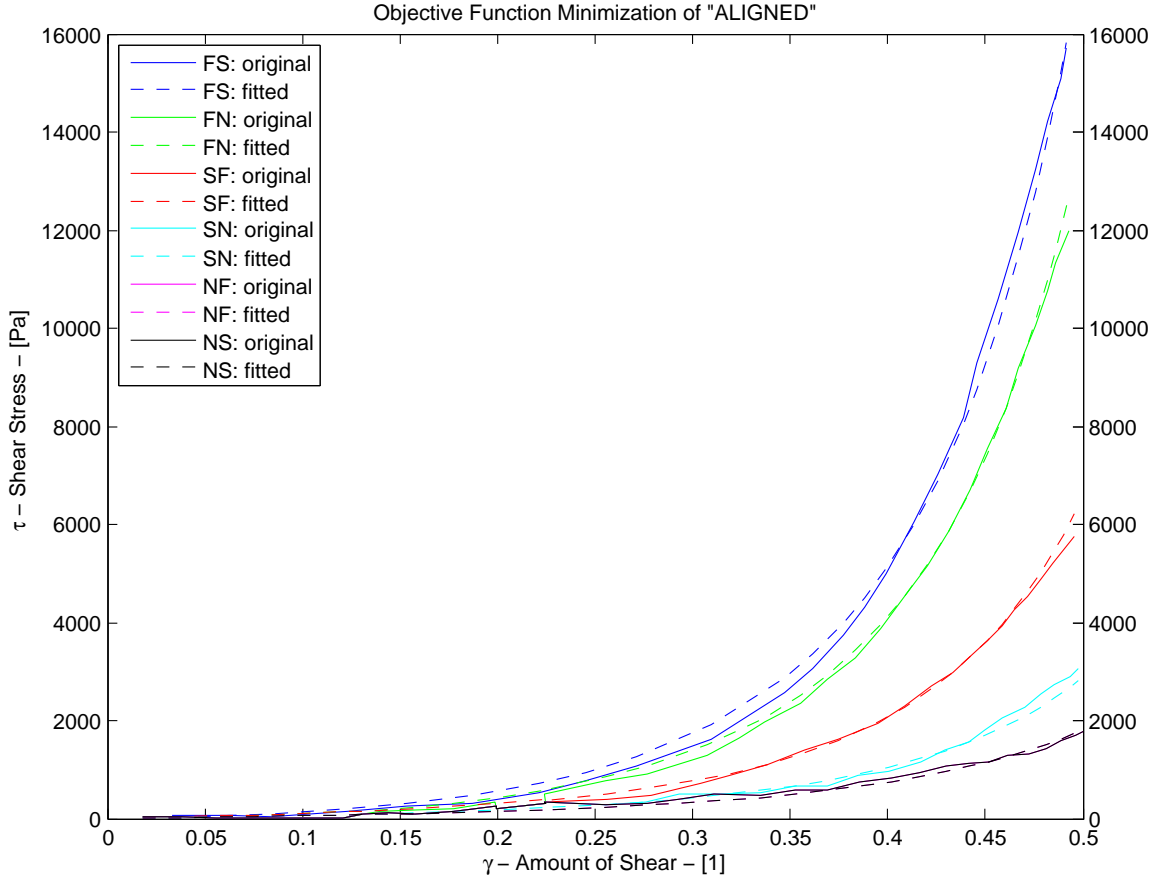
Figure 4.15.: Elastic parameter fit for model 'ALIGNED' of data from Dokos et al.[9]

shows a very interesting effect called 'strain-softening' which is discussed in Sec. 4.4. The fit for our mean data is listed in Table 4.4. The obtained parameters show an interesting trend when compared for rising $\hat{\gamma}$. All stiffness parameters decrease rapidly especially fiber and sheet stiffnesses due to 'strain-softening'. Initially, nonlinearity increases until reaching $\gamma = 0.3$ but diminishes as soon as the coupling nonlinearity occurs.

Note. If the nonlinearity parameter is zero, tissue will behave mostly linear. In fact, at small amounts of shear experiments prove that the tissue shows small nonlinearities which increase with increasing shear.

4.2.4. Hyperelastic Exponential Model Considering Rotationally Symmetric Dispersion 'KAPPA'

Eriksson [13] shows possible values for dispersion of fibers and sheets by investigating data from Karlon et al. [34] and Kovel [6] via using the *von Mises* point density function (PDF) and a structure tensor approach. Eriksson states, that the dispersion of healthy and diseased fibers is $\kappa_f^{(H)} = 0.00765$ and $\kappa_f^{(D)} = 0.08856$, respectively. The sheet dis-

Table 4.3.: Verification data fit for model 'ALIGNED' with data from Dokos et al. [9] and model fit from Holzapfel et al. [25] (called 'VERIFIC').

Model	R^2	a	b	a_f	b_f	a_s	b_s	a_{fs}	b_{fs}
-	[%]	[kPa]	[1]	[kPa]	[1]	[kPa]	[1]	[kPa]	[1]
ALIGNED	99.71	0.564	7.452	17.16	16.74	1.620	15.31	0.393	11.73
VERIFIC	-	0.059	8.023	18.47	16.02	2.481	11.12	0.216	11.44

Table 4.4.: Mean elastic stress-shear data fit for model 'ALIGNED'.

Shear	R^2	a	b	a_f	b_f	a_s	b_s	a_{fs}	b_{fs}
$\hat{\gamma}$	[%]	[kPa]	[1]	[kPa]	[1]	[kPa]	[1]	[kPa]	[1]
0.1	96.96	6.178	0	506.4	0	102.8	4969	3.362	0
0.2	98.24	3.106	12.53	101.7	22.90	16.65	477.4	2.123	5.669
0.3	98.94	2.002	10.72	25.94	66.37	3.595	170.2	1.294	7.470
0.4	99.52	1.411	8.453	10.42	36.74	2.179	63.82	0.683	7.825
0.5	99.82	0.945	6.733	5.712	19.59	0.622	36.85	0.382	7.226
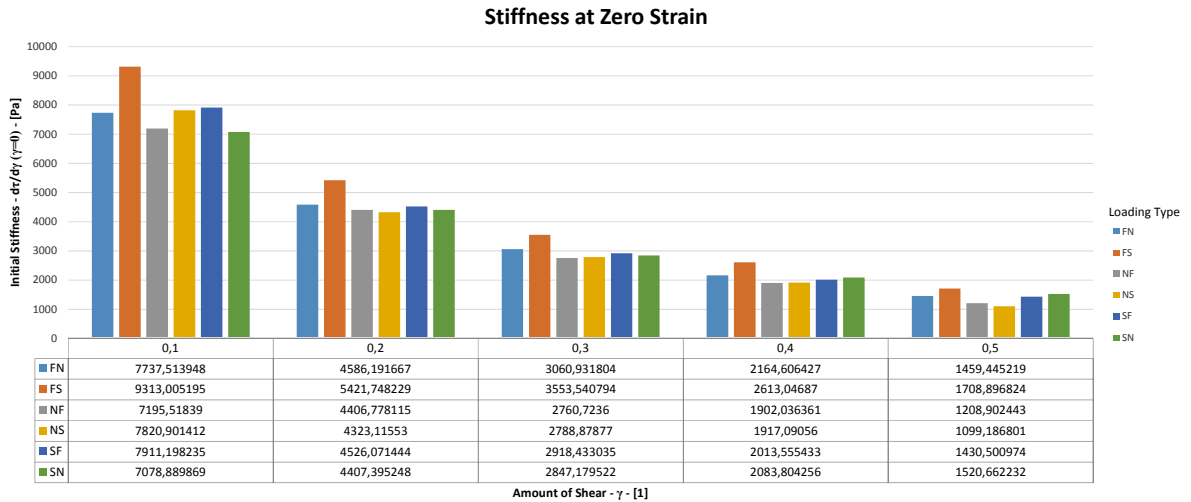
Figure 4.16.: Initial total stiffness $\mathrm{d}\tau/\mathrm{d}\gamma$ of complete myocardium at zero strain $\gamma = 0$.
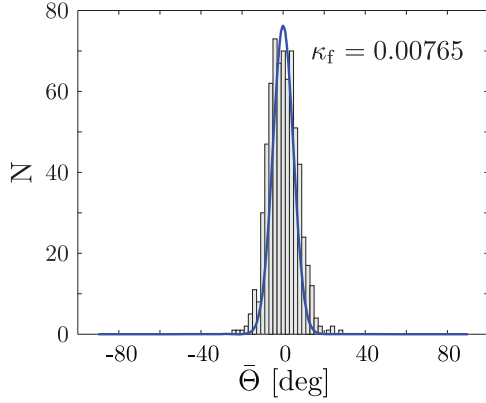
(a) Healthy fiber dispersion (taken from Eriksson et al. [13]).
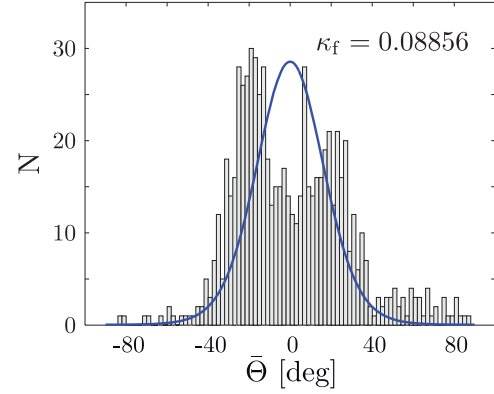
(b) Diseased fiber dispersion (taken from Eriksson et al. [13]).
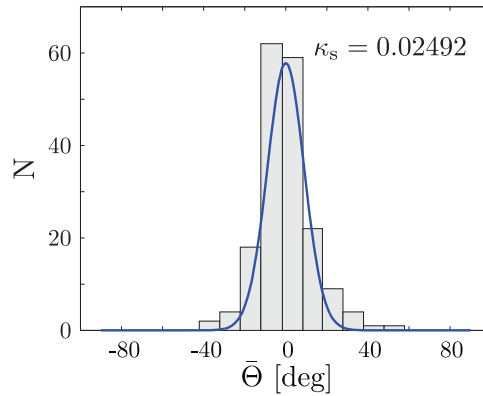
(c) Healthy sheet dispersion (taken from Eriksson et al. [13]).

Figure 4.17.: Fiber dispersion fit of *von Mises* PDF used by Eriksson [13] applied on data from [6, 34].

persion is stated to reach $\kappa_s = 0.02492$. Apparently, diseased myocardium shows higher fiber dispersion (more than ten times higher) [13]. In Figs. 4.17(a), 4.17(b) and 4.17(c) Eriksson shows how the *von Mises* PDF is used to determine the dispersion. Notably, diseased fiber distribution seems to have multiple means of fiber directions.

The obtained parameter fit is given in Table 4.5 for dispersions $\kappa_f = 0.00765$ and $\kappa_s = 0.02492$ as well as with recently determined dispersion values of human non-diseased myocardium at the institute being $\kappa_f = 0.08$ and $\kappa_s = 0.09$. As mentioned in Sec. 4.2.3, softening is obvious with increasing shear. Interestingly, dispersion reduces stiffness of matrix compound but increases stiffnesses of fibers and sheets. This means, that diseased myocardial tissue should show higher dispersion linked with higher fiber and sheet stiffness making the myocardium less vital and elastic. Another interesting fact is that stiffnesses decrease steadily but nonlinearities increase until $\hat{\gamma} = 0.3$ and decrease afterwards. Apparently, the tissue initially increases nonlinearity to compensate

Table 4.5.: Mean elastic stress-shear data fit for model 'KAPPA'.

Shear	R^2	a	b	a_f	b_f	a_s	b_s	a_{fs}	b_{fs}
$\hat{\gamma}$	[%]	[kPa]	[1]	[kPa]	[1]	[kPa]	[1]	[kPa]	[1]
$\kappa_f = 0.00765$ & $\kappa_s = 0.02492$									
10%	96.96	6.177	0	522.2	0	113.8	5502	3.362	0
20%	98.24	3.106	12.52	104.9	23.65	18.45	528.8	2.123	5.669
30%	98.94	2.002	10.72	26.75	68.45	3.983	188.5	1.294	7.469
40%	99.52	1.411	8.452	10.75	37.89	2.414	70.69	0.683	7.825
50%	99.82	0.945	6.733	5.891	20.21	0.689	40.82	0.382	7.226
$\kappa_f = 0.08$ & $\kappa_s = 0.09$									
10%	96.95	6.123	0	720.4	0	152.8	7158	3.377	0
20%	98.24	3.103	12.06	145.1	35.47	24.80	717.8	2.124	5.647
30%	98.93	1.997	10.63	36.99	94.10	5.331	254.8	1.296	7.444
40%	99.52	1.406	8.424	14.84	52.02	3.237	95.25	0.685	7.798
50%	99.82	0.941	6.725	8.138	27.72	0.920	55.02	0.383	7.206

the softening effect but at some point the tissue starts to fail. Maybe, decreasing stiffness and nonlinearity marks the beginning of irreversible tissue damage. In Fig. 4.18 the relative parameter change to its maximum per peak amount of shear cycle is drawn. Fiber and sheets stiffness seem to be affected by softening in the same manner whereas coupling and matrix softening reduces slower. Nonlinearity increases for matrix, fibers and sheets nearly identically although coupling effects show shifted increase. Paradoxically, the coupling nonlinearity seems to occur when all other parameters decrease.

In Table 4.6 modeling results of 'ALIGNED' and 'KAPPA' fits are compared via

$$r_i^{(a)} = 1 - \frac{a_i^{(ALIGNED)}}{a_i^{(KAPPA)}}, \tag{4.2}$$

$$r_i^{(b)} = 1 - \frac{b_i^{(ALIGNED)}}{b_i^{(KAPPA)}}. \tag{4.3}$$

Relative stiffness parameters seem to show approximately equal changes and equal changes are seen for nonlinearity. In average, fiber stiffness increases by approximately $\sim 3\%$ and sheet stiffness increases by $\sim 9\%$ for the given dispersion from Eriksson et al. [13]. This is not surprising as sheet dispersion given is about three times higher than fibers dispersion. Ground substance and coupling parameters show slightly decreased values due to fibers and sheets taking care of isotropic functions.

In general, a simulation of changed dispersion parameters and how different combinations of fiber and sheet dispersion influence stiffness a_i and nonlinearity parameters b_i is shown in Figs. 4.19 and 4.20. As already stated, matrix stiffness and nonlinearity decreases with higher dispersion as fibers and sheets take its place. Fiber stiffness and nonlinearity increases linearly with increasing fiber dispersion but remains nearly unaffected by sheet dispersion. Identical observations can be made for sheet stiffness
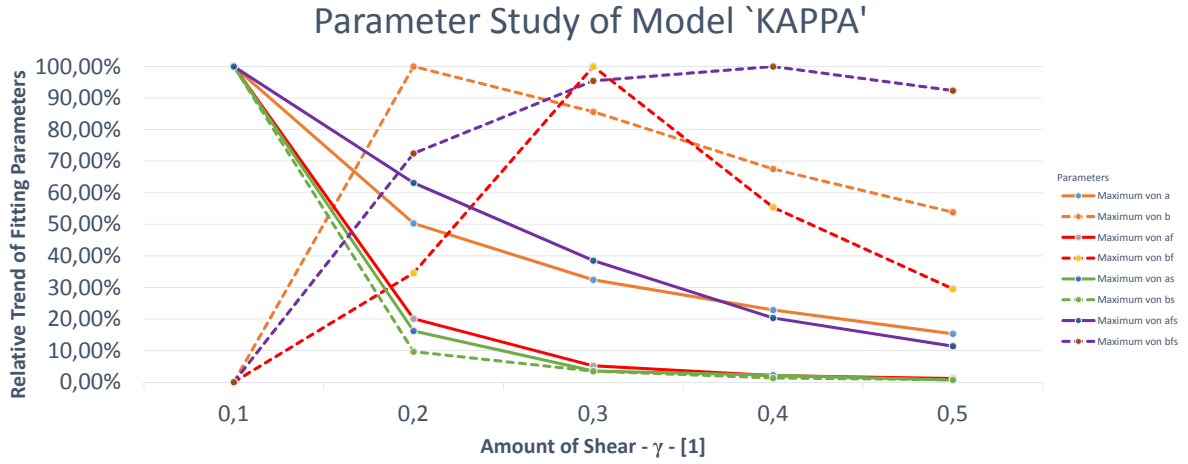
Figure 4.18.: Softening shown via trend analysis of fitting parameter of model 'KAPPA'.

Table 4.6.: Relative parameter changes for 'ALIGNED' related to 'KAPPA'.

Shear	$r_m^{(a)}$	$r_m^{(b)}$	$r_f^{(a)}$	$r_f^{(b)}$	$r_s^{(a)}$	$r_s^{(b)}$	$r_{fs}^{(a)}$	$r_{fs}^{(b)}$
$\hat{\gamma}$	%	%	%	%	%	%	%	%
10%	-0.015	-	3.033	-	9.736	9.698	0.009	-
20%	-0.001	-0.059	3.038	3.195	9.756	9.718	0.002	-0.009
30%	-0.003	-0.013	3.038	3.043	9.742	9.718	0.004	-0.006
40%	-0.005	-0.006	3.036	3.041	9.741	9.716	0.008	-0.008
50%	-0.005	-0.002	3.037	3.038	9.728	9.720	0.009	-0.005
MEAN	-0.006	-0.020	3.036	3.079	9.741	9.714	0.007	-0.007

(a) Study of matrix stiffness parameter a.

(b) Study of matrix nonlinearity parameter b.

(c) Study of fiber stiffness parameter a_f.

(d) Study of fiber nonlinearity parameter b_f.
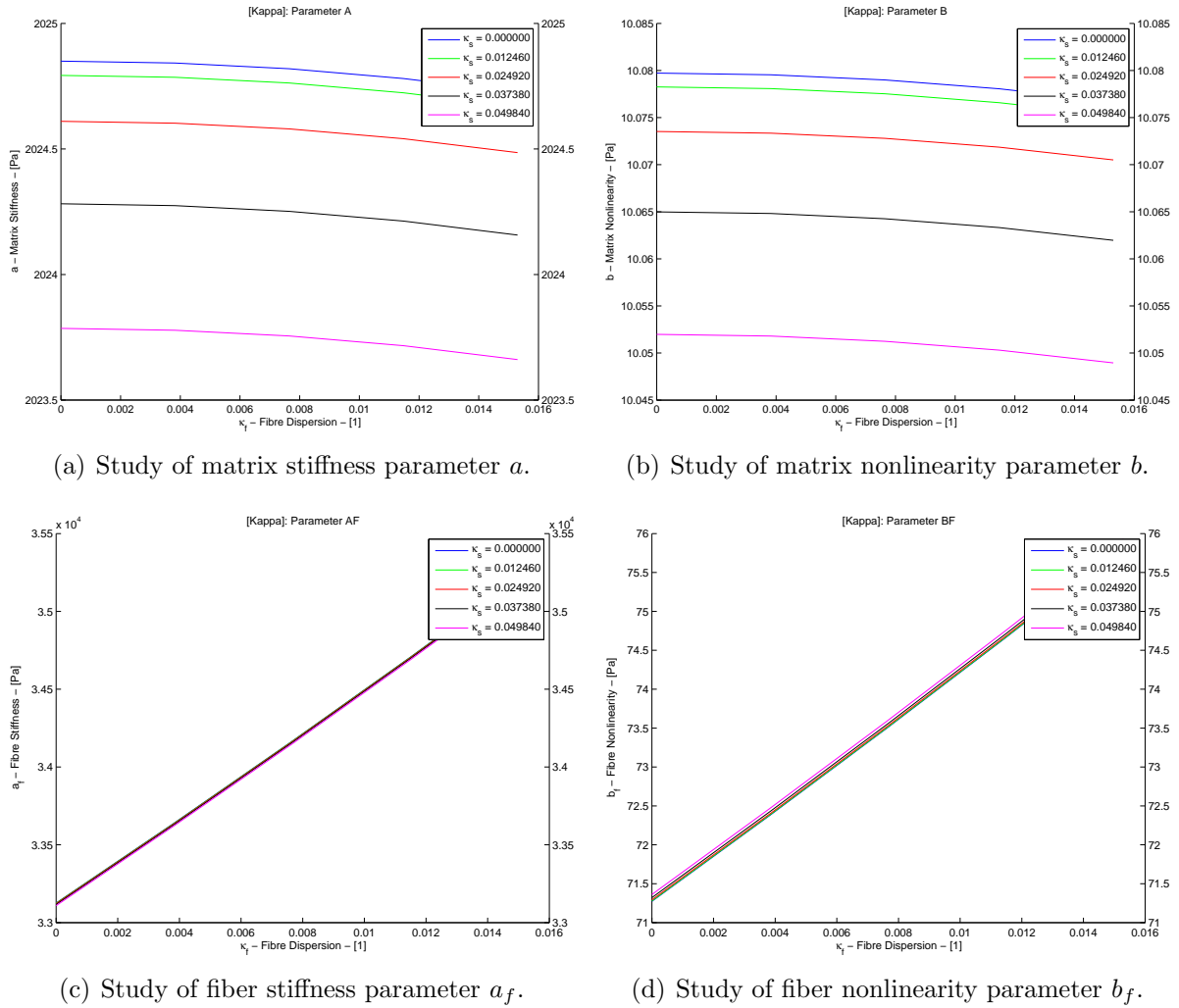
Figure 4.19.: Parameter study of model 'KAPPA' for varying fiber and sheet dispersion of parameters a, b, a_f and b_f.

and nonlinearity. Interestingly, coupling stiffness increases with higher fiber and sheet dispersion but nonlinearity decreases in this case. The reason for this is that higher dispersion also increases fiber and sheet nonlinearity so that coupling effects compensate this change in the same manner. Thus, higher dispersion directly influence stiffness and nonlinearity which can be compensated to some extent by coupling effects of fibers and sheets which can also be obtained when looking at Table 4.6 again.
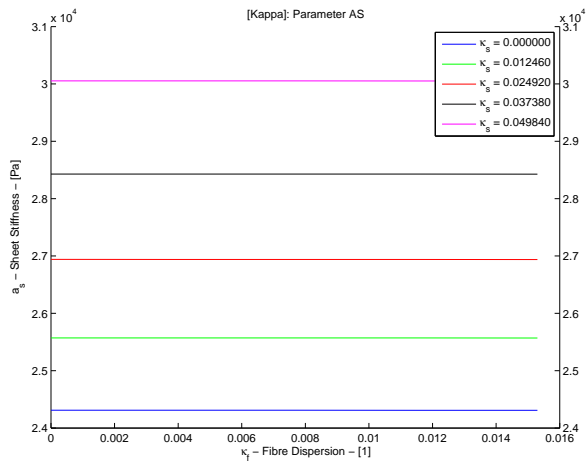
(a) Study of sheet stiffness parameter a_s.
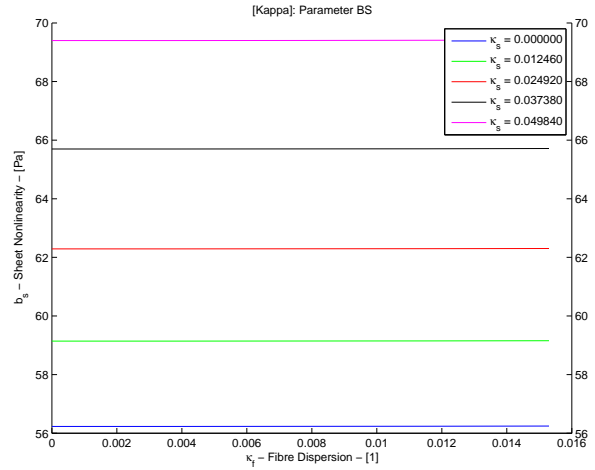
(b) Study of sheet nonlinearity parameter b_s.
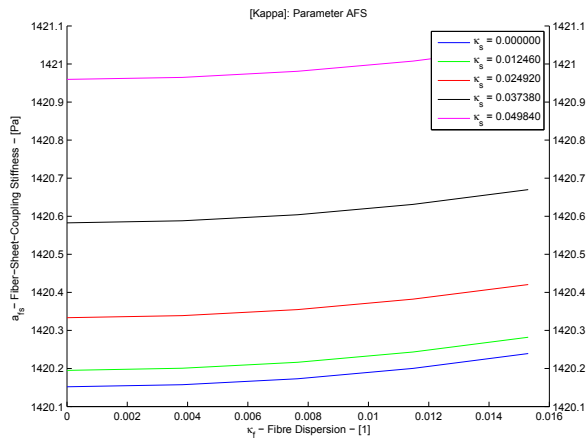
(c) Study of coupling stiffness parameter a_{fs}.
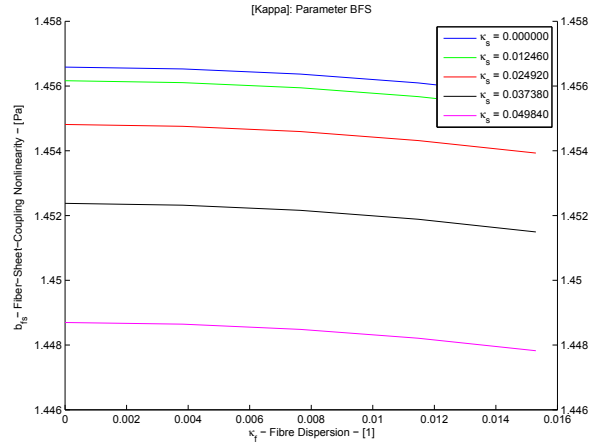
(d) Study of coupling nonlinearity parameter b_{fs}.

Figure 4.20.: Parameter study of model 'KAPPA' for varying fiber and sheet dispersion of parameters a_s, b_s, a_{fs} and b_{fs}.

Table 4.7.: Mean viscoelastic/inelastic stress-shear data fit for model
'Simple-Damping'.

Shear	R^2	Damping			
		$\mu_m^{(D)}$	$\mu_f^{(D)}$	$\mu_s^{(D)}$	$\mu_{fs}^{(D)}$
$\hat{\gamma}$	[%]	[kPa s]	[kPa s]	[kPa s]	[kPa s]
10%	47.09	12.02	15.74	5.305	4.384
20%	-250.0	15.52	22.55	6.884	8.161
30%	-311.2	19.03	25.86	7.309	9.943
40%	-225.2	21.65	27.80	11.66	11.05
50%	-166.6	22.84	25.03	8.591	11.57
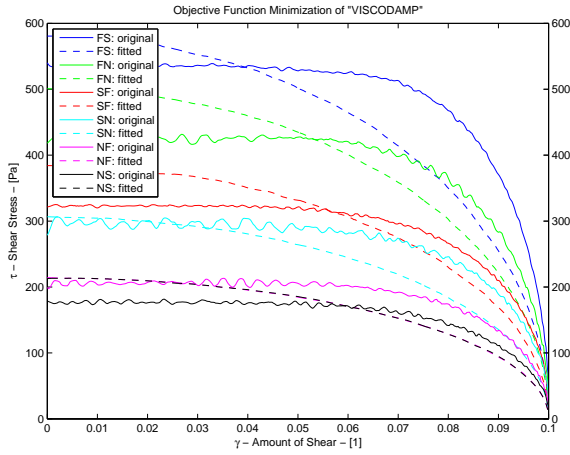
(a) Viscoelastic/inelastic parameter fitting for model 'SIMPLE-DAMPING' at $\gamma = 0.1$.
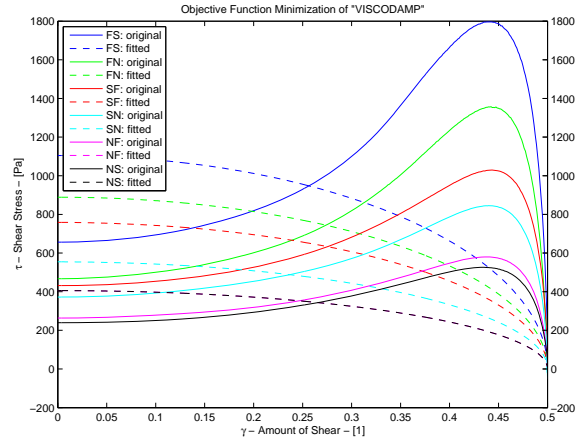
(b) Viscoelastic/inelastic parameter fitting for model 'SIMPLE-DAMPING' at $\gamma = 0.5$.

Figure 4.21.: Data fit for all loading modes with inelastic model 'SIMPLE-DAMPING'.

4.3. Parameter Fits for Proposed Models

4.3.1. Viscoelastic/Inelastic Model: 'Simple-Damping'

In Table 4.7 the fitted parameters for model 'SIMPLE-DAMPING' are listed. As a matter of fact, the model is not appropriate for higher amounts of shear (see column 'Confidence' in Table 4.7). In Figs. 4.21(a) and 4.21(b) the regression for $\gamma = 0.1$ and $\gamma = 0.5$ is shown, respectively. It is obvious that this simple model cannot describe the inelastic stress response of myocardial tissue in an acceptable manner as R^2 is negative for higher amounts of shear. Whenever R^2 is negative the proposed model is worse than a simple linear fit.

Nevertheless, a closer look at the determined parameters allows first estimations about dependencies of damping viscosity parameters $\mu_i^{(D)}$ and peak value of amount of shear. In Fig. 4.22(a) the fibers contribute most in terms of highest viscosity parameters. The
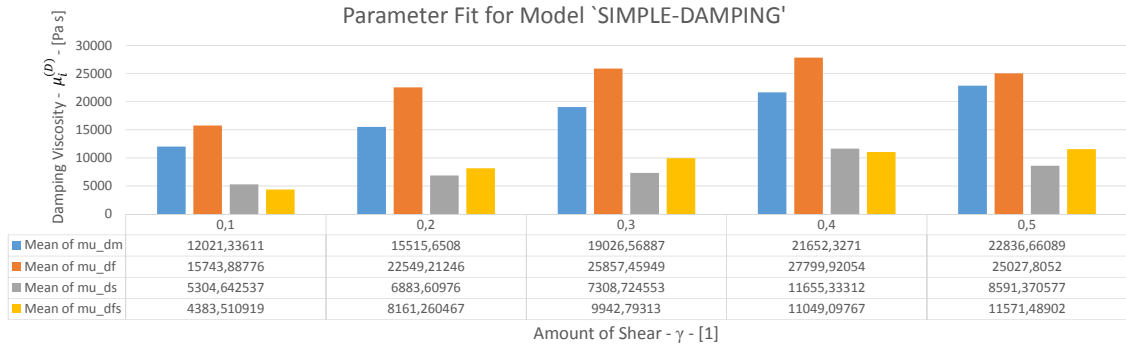
(a) Viscoelastic/inelastic parameter fit study of absolute values $\mu_i^{(D)}$.
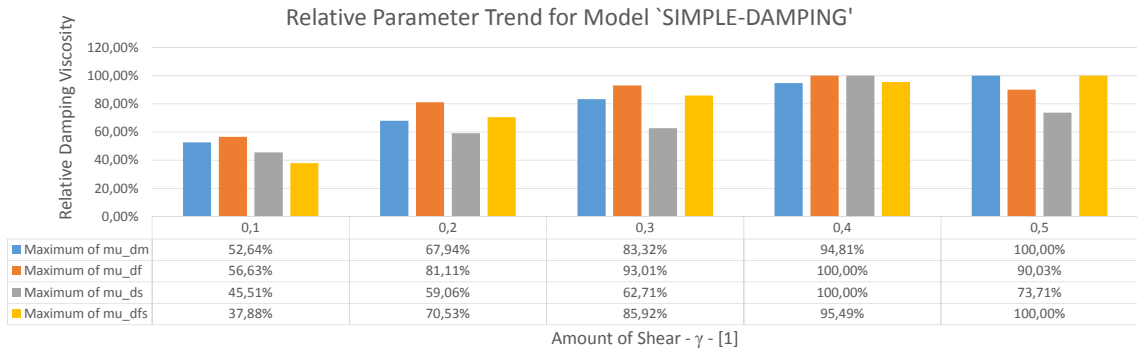
(b) Viscoelastic/inelastic parameter fit study of relative parameters values with respect to maximum.

Figure 4.22.: Complete data fit for all loading modes with inelastic model 'SIMPLE-DAMPING'.

trend given in Fig. 4.22(b) shows that matrix, fibers, sheets and coupling constants increase steadily for increasing amount of shear which proves that hysteresis increases for additional loading cycles at higher amount of shear.

Note. Higher amounts of shear are coupled with lower rates of shear as $\gamma = \hat{\gamma}\sin(2\pi f t)$. Due to quasistatic loading, the transient effects can be neglected, and thus history dependency caused by previous loading cycles cause bigger stress hysteresis. Therefore, some type of restructuring during loading must be present. This type of model is discussed in Sec. 3.4.3.

The simulation of a complete loading cycle is shown for all loading types in Fig. 4.23. All six loading modes show same peak residuals at higher amounts of shear. Another lack of this model is that it cannot describe the increase of viscous shear stress during loading but only a degressive decrease of viscous shear stress for lower rates of shear.

(a) Simulation for FS-mode.

(b) Simulation for FN-mode.

(c) Simulation for SF-mode.

(d) Simulation for SN-mode.

(e) Simulation for NF-mode.

(f) Simulation for NS-mode.
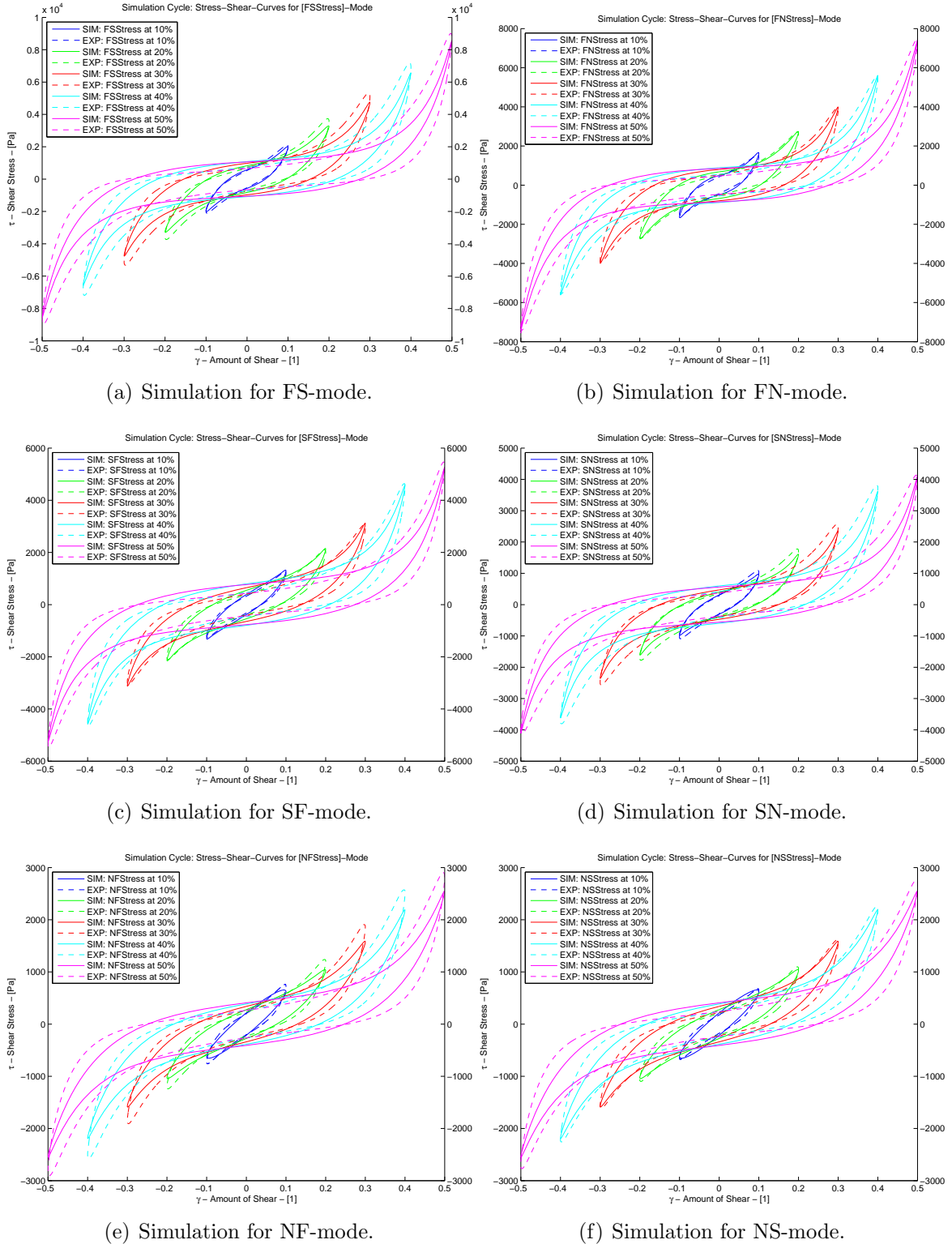
Figure 4.23.: Complete simulation cycle for [FS-FN/SF-SN/NF-NS]-modes with elastic model 'KAPPA' and inelastic model 'SIMPLE-DAMPING'.
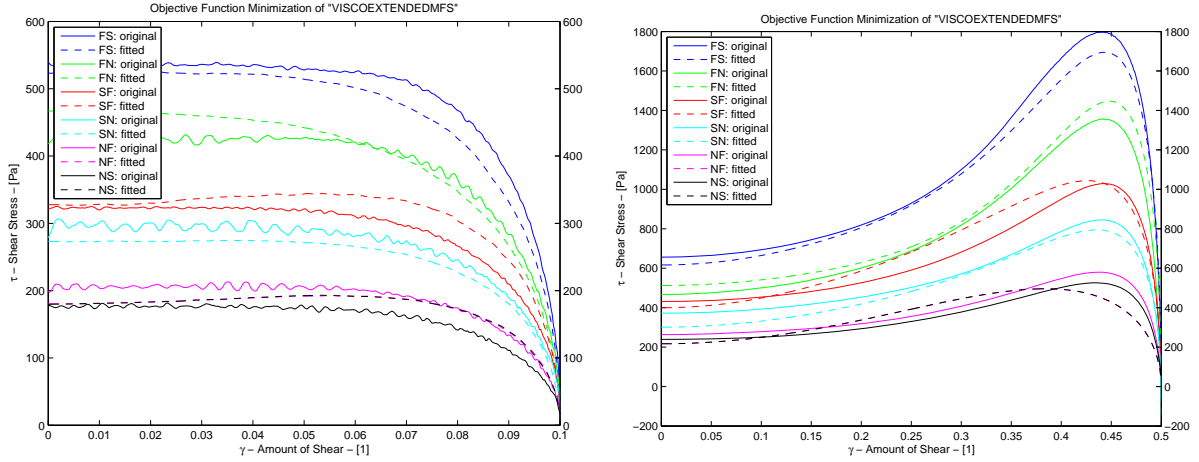
(a) Viscoelastic/inelastic parameter fitting compared to mean of experimental data for $\hat{\gamma} = 0.1$.

(b) Viscoelastic/inelastic parameter fitting compared to mean of experimental data for $\hat{\gamma} = 0.5$.

Figure 4.24.: Data fit of visoelastic/inelastic model 'RESDAMP-MAFISH' for FS-mode.

Table 4.8.: Mean viscoelastic/inelastic stress-shear data fit for model 'ResDamp-MaFiSh'.

Shear	R^2	Restructuring				Damping			
		$\mu_m^{(R)}$	$\mu_f^{(R)}$	$\mu_s^{(R)}$	$\mu_{fs}^{(R)}$	$\mu_m^{(D)}$	$\mu_f^{(D)}$	$\mu_s^{(D)}$	$\mu_{fs}^{(D)}$
$\hat{\gamma}$	[%]	[kPa s]	[MPa s]	[MPa s]	[kPa s]	[kPa s]	[kPa s]	[kPa s]	[kPa s]
10%	86.40	937.3	0	0	436.6	10.14	15.74	5.303	3.072
20%	65.24	519.6	131.2	8.382	283.0	11.36	20.15	6.731	4.767
30%	77.42	378.9	21.60	4.879	181.6	12.22	21.36	6.294	5.047
40%	91.31	288.6	6.294	2.738	127.2	12.43	20.44	8.454	4.958
50%	94.31	212.8	2.166	0.837	79.95	12.22	15.37	4.859	5.586

4.3.2. Viscoelastic/Inelastic Model: 'ResDamp-MaFiSh'

In Section 3.4.3 we introduced a new approach to model periodic response of viscoelastic/inelastic behavior of myocardium to sinusoidal simple shear deformation. In Figure 4.24 an example elastic and viscoelastic fit is performed. The extended model is capable of fitting the mean of data in an acceptable manner for all given $\hat{\gamma}$.

In Table 4.8 all fitted parameters are listed and performs with higher confidence than the 'SIMPLE-DAMPING' model. Interestingly, when comparing the relative changes of the parameter shown in Figs. 4.25 and 4.26 the tissue shows decreasing restructuring effects with higher amounts of shear whereas the damping effects remain nearly unchanged. This may be due to realignment, rotation or sliding of fibers and sheets so that restructuring leads to rearrangement of tissue.

Finally, we combine the 'KAPPA' and 'RESDAMP-MAFISH' models and reproduce the complete hysteresis. Figures 4.27(a)–4.27(f) present the performance of all models which

(a) Restructuring.

(b) Damping.
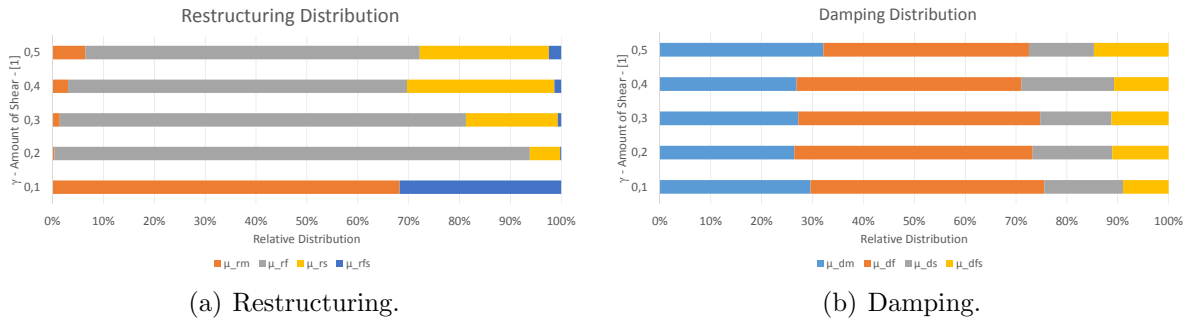
Figure 4.25.: Comparison of parameter distribution referred to parameter maximum for $\gamma = 0.1 - 0.5$.
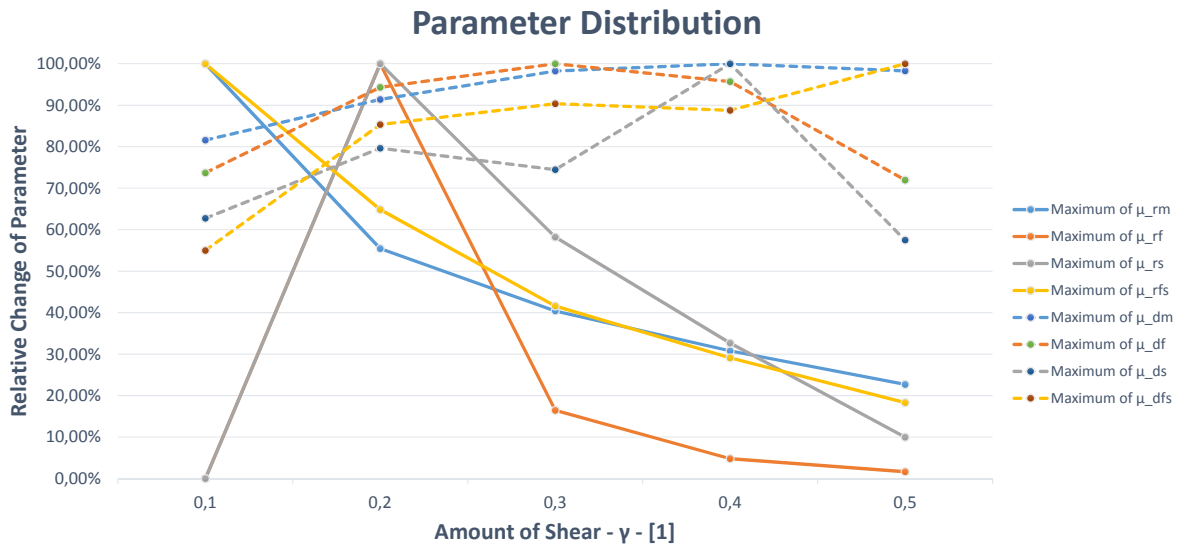
Figure 4.26.: Parameter distribution vs. increasing shear.

Table 4.9.: Relative tissue softening for consequent loading cycles.

$\hat{\gamma}_i \rightarrow \hat{\gamma}_{i+1}$	$\zeta_{iso,FS}^{(R)}$	$\zeta_{iso,FN}^{(R)}$	$\zeta_{iso,SF}^{(R)}$	$\zeta_{iso,SN}^{(R)}$	$\zeta_{iso,NF}^{(R)}$	$\zeta_{iso,NS}^{(R)}$	MEAN
Units	[%]	[%]	[%]	[%]	[%]	[%]	[%]
$0.1 \rightarrow 0.2$	54.14	59.78	48.02	53.65	46.43	46.43	51.41
$0.2 \rightarrow 0.3$	42.43	44.11	38.29	38.11	36.13	36.13	39.20
$0.3 \rightarrow 0.4$	38.38	33.31	36.89	30.47	30.33	30.33	33.29
$0.4 \rightarrow 0.5$	37.40	34.29	37.38	34.11	33.57	33.57	35.06
MEAN	43.09	42.88	40.15	39.09	36.61	36.61	-

represent the experimental data very well. FS and FN modes are described best followed by SF and SN modes. NF and NS modes are modeled as one which cause their related fits to represent the average.

4.4. Softening of Myocardium

In the previous sections we have shown that for higher loading cycles myocardium seems to soften in a mechanical point of view. In Table 4.5 all stiffness parameters a, a_f, a_s and a_{fs} decrease with increasing $\hat{\gamma}$ which is a strong evidence for presence of tissue softening. In fact, the softening effect may also occur in living tissue extending elasticity of myocardium, e.g. enabling extended wall thickening during systole and diastole as stated by LeGrice et al. [36].

In Fig. 4.28 the relative isotropic softening of tissue is shown based on the algorithm presented in Sec. 4.4. Obviously, softening effects reduce with increasing number of loading cycles (see Table 4.9). Interestingly, the relative softening referred to the previous loading cycle shows softening in the range of 50% and slightly decreasing with higher amount of shear. Consequently, softening seems to be an propagating effect with slight decrease for higher amount of shear.

Further investigation of relative changes of fitting parameters show that softening influences the stiffness parameters a at most (see Figs. 4.29 and 4.18). This knowledge enables us to model softening via reduction of unsoftened strain-energy functions.

The absolute isotropic softening model proposed in Sec. 4.4 gives information about softening in detail. We apply both elastic models 'ALIGNED' and 'KAPPA' on the experimental data provided and use the proposed algorithm with including the fourth step. Hereafter, softened model versions will be denoted with superscript 's', e.g. 'ALIGNED[S]'. Finally, we use the softening parameter s to represent softening for the complete myocardium. Based on fitting the mean of data with the 'ALIGNED[S]' model including absolute isotropic softening $\zeta_{iso}^{(A)}$ we can plot Fig. 4.30. Interestingly, the simulated cycles reach the peak stress pretty well but fail representing nonlinearity. The nonlinearity parameters b have much more influence on fiber stiffness and sheet stiffness but those are not influenced by softening. In fact, the proposed softening model lowers the overall

(a) Simulation for FS-mode.

(b) Simulation for FN-mode.

(c) Simulation for SF-mode.

(d) Simulation for SN-mode.

(e) Simulation for NF-mode.

(f) Simulation for NS-mode.
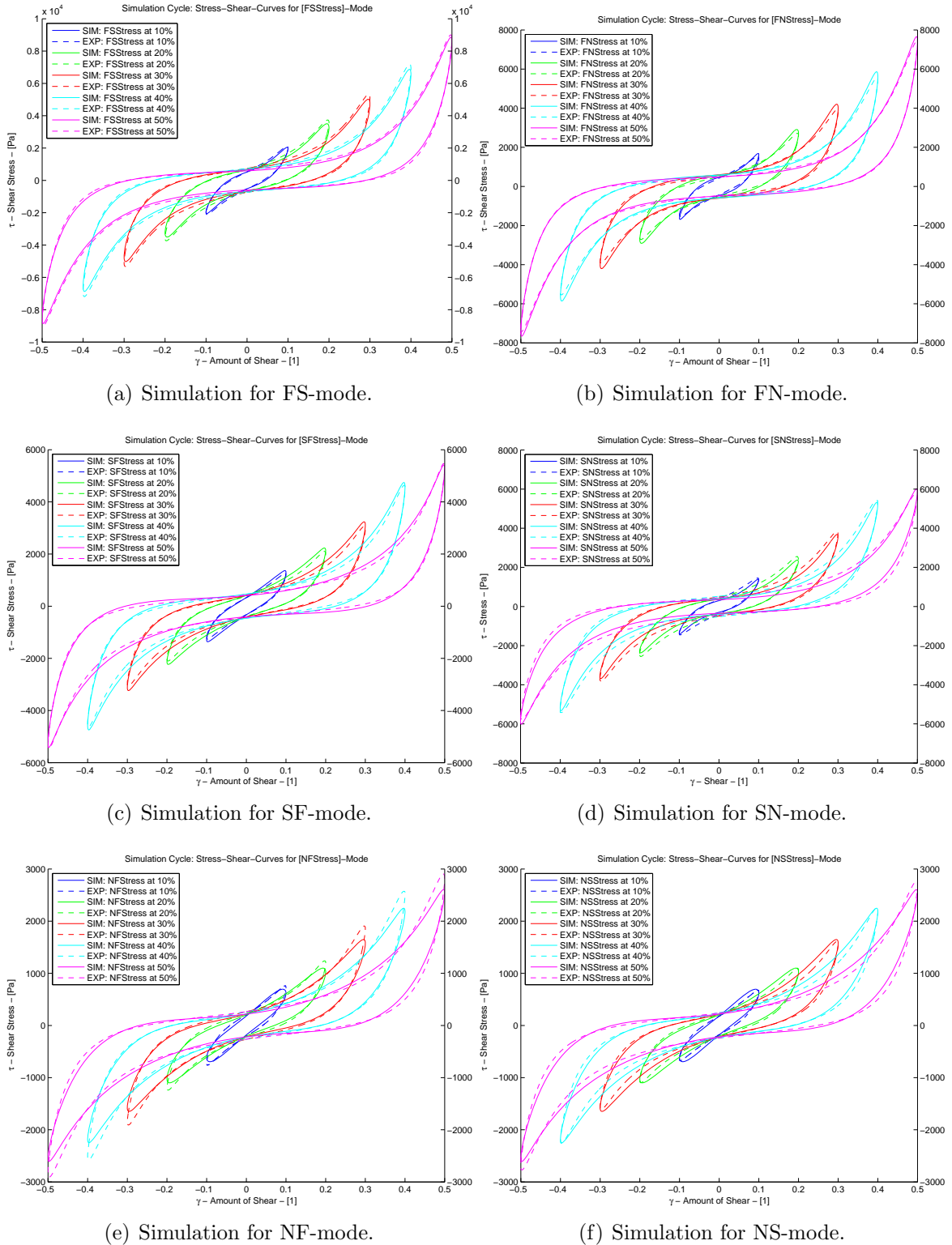
Figure 4.27.: Complete simulation cycle for [FS-FN/SF-SN/NF-NS]-modes with elastic model 'KAPPA' and inelastic model 'RESDAMP-MAFISH'.

(a) Relative softening of myocardial tissue referred to previous loading cycle.

(b) Cumulative relative softening of myocardial tissue referred to first loading cycle at $\gamma = 0.1$.
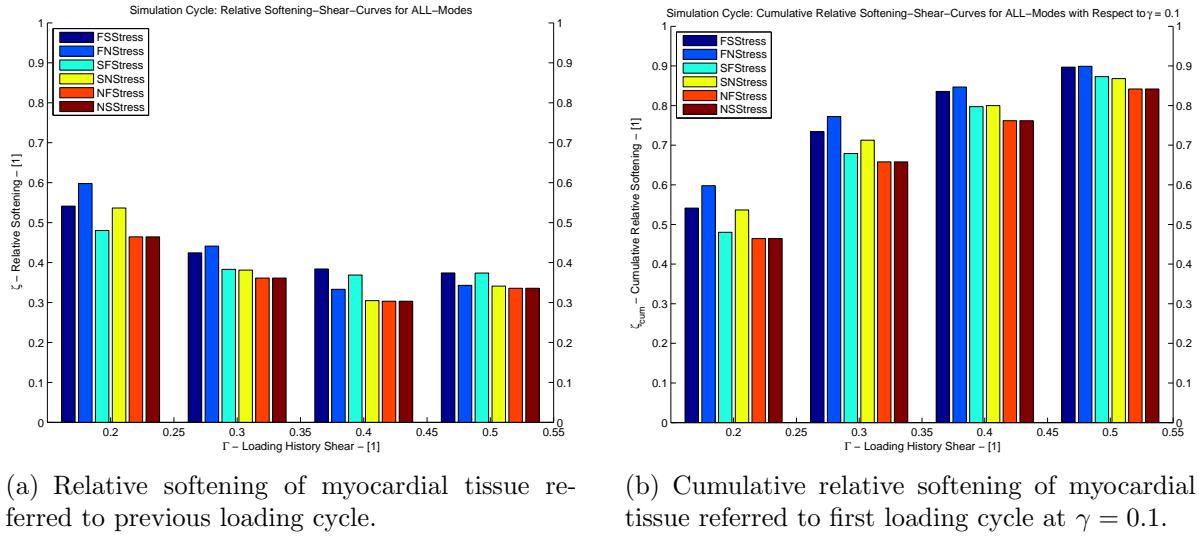
Figure 4.28.: Relative and cumulative tissue softening after first loading cycle at $\gamma = 0.1$ for consequent cycles with increment $\Delta\gamma = 0.1$.
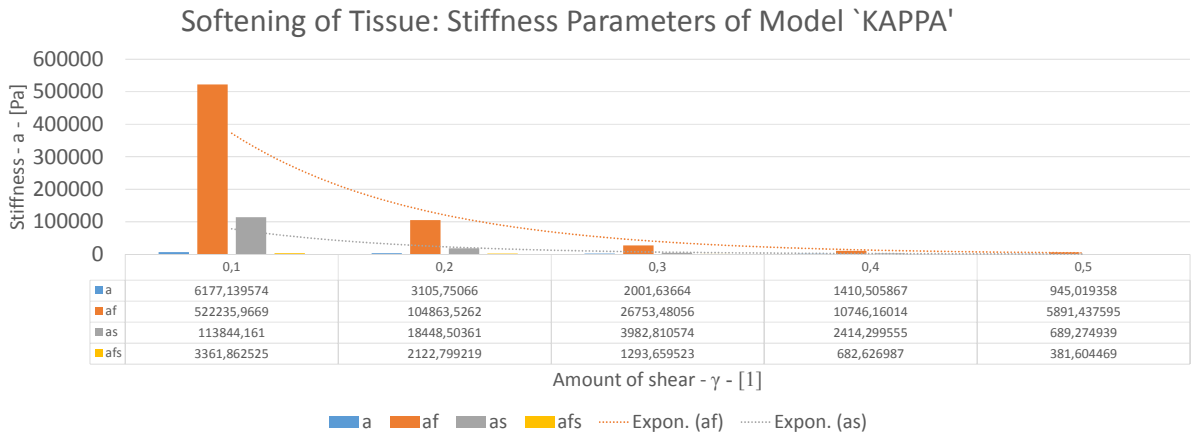
Figure 4.29.: Softening shown via trend analysis of fitting parameter of model 'KAPPA'.

Table 4.10.: Fit of absolute softening function $\zeta_{iso}^{(A)}$ where 'MEAN' refers to a separate fit of all loading modes united.

Loading Mode	$\bar{\tau}(\Gamma = 0)$	s
Unit	[kPa]	[1]
FS	1.436583	6.897547
FN	1.230139	7.964840
SF	0.941679	5.635320
SN	0.676345	6.115662
NF	0.504783	5.133939
NS	0.504783	5.133939
MEAN	-	6.246303

Table 4.11.: Fit of model 'ALIGNED^S' and 'KAPPA^S' with $\kappa_f = 0.00765$ and $\kappa_s = 0.02492$ including softening with softening parameter $s = 6.246303$. 'KAPPA' refers to an unsoftened data fit with parameters taken from Table 4.5.

Model	Shear	R^2	a	b	a_f	b_f	a_s	b_s	a_{fs}	b_{fs}
-	$\hat{\gamma}$	[%]	[kPa]	[1]	[kPa]	[1]	[kPa]	[1]	[kPa]	[1]
ALIGNED^S	50%	99.82	21.47	6.733	129.8	19.59	14.14	36.85	8.668	7.226
KAPPA^S	50%	99.82	21.47	6.733	133.8	20.21	15.66	40.82	8.669	7.226
KAPPA	50%	99.82	0.950	6.733	5.891	20.21	0.689	40.82	0.382	7.226
$1 - \frac{\text{KAPPA}}{\text{KAPPA}^S}$	50%	-	0.956	0	0.956	0	0.956	0	0.956	0

strain-energy but keeps morphology identical which may be a shortcoming. In Table 4.10 all softening parameters are listed referred to their corresponding loading modes and history shears Γ.

The underlying fits of models 'ALIGNED^S' and 'KAPPA^S' are applied to the last cycle at $\hat{\gamma} = 0.5$ and their parameter sets are given in Table 4.11. Both models show drastically increased stiffness parameters whereas nonlinearity parameters b remain unchanged when observing Table 4.5. Another interesting fact is that the goodness of fit represented by R^2 is identical for all three fits. The softened models do not change the morphology of the functions themselves and, therefore, neither improve nor deteriorate the goodness of fit R^2 for the underlying experimental data.

Another interesting fact is that the overall softening shown in Fig. 4.31 is different for different loading modes FS, FN, SF, SN, NF and NS. Hence, softening seems to be an anisotropic effect which needs to be investigated in detail regarding different tissue compounds and directions.
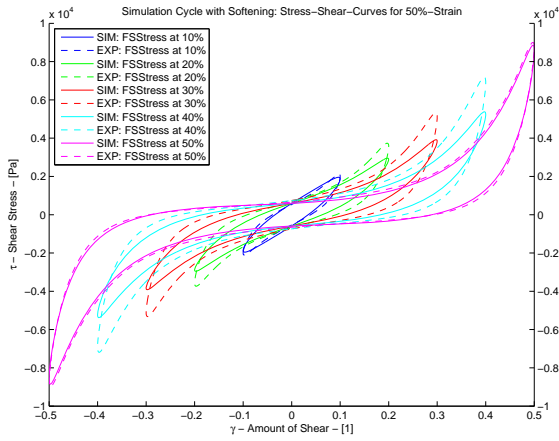
(a) Simulation for FS-mode.
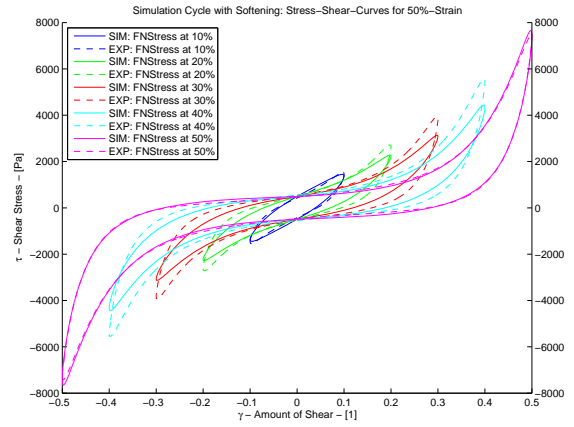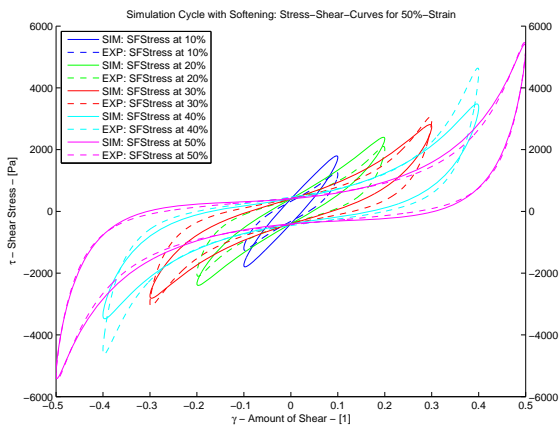
(b) Simulation for FN-mode.

(c) Simulation for SF-mode.
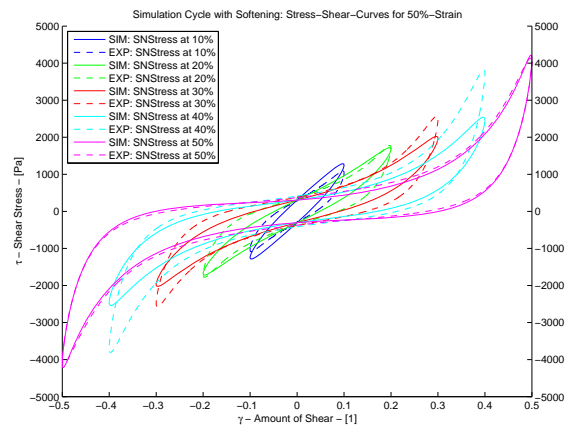
(d) Simulation for SN-mode.
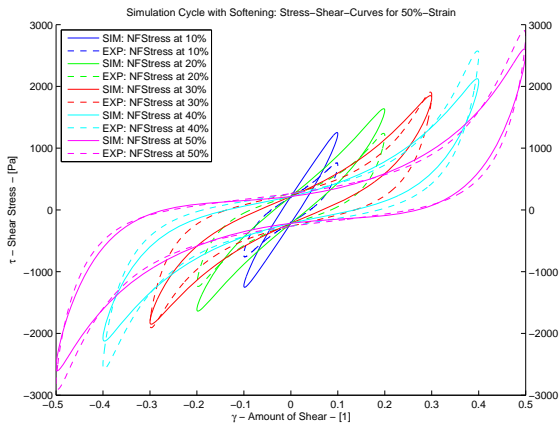
(e) Simulation for NF-mode.
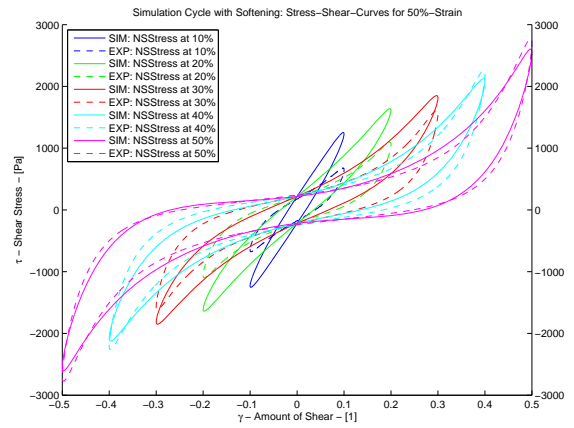
(f) Simulation for NS-mode.

Figure 4.30.: Complete simulation cycle for [FS-FN/SF-SN/NF-NS]-modes with elastic model 'KAPPA' with $\kappa_f = 0.00765$ and $\kappa_s = 0.02492$ including softening with softening parameter $s = 6.246303$ and inelastic model 'RESDAMP-MAFISH' based on $\hat{\gamma} = 0.5$.
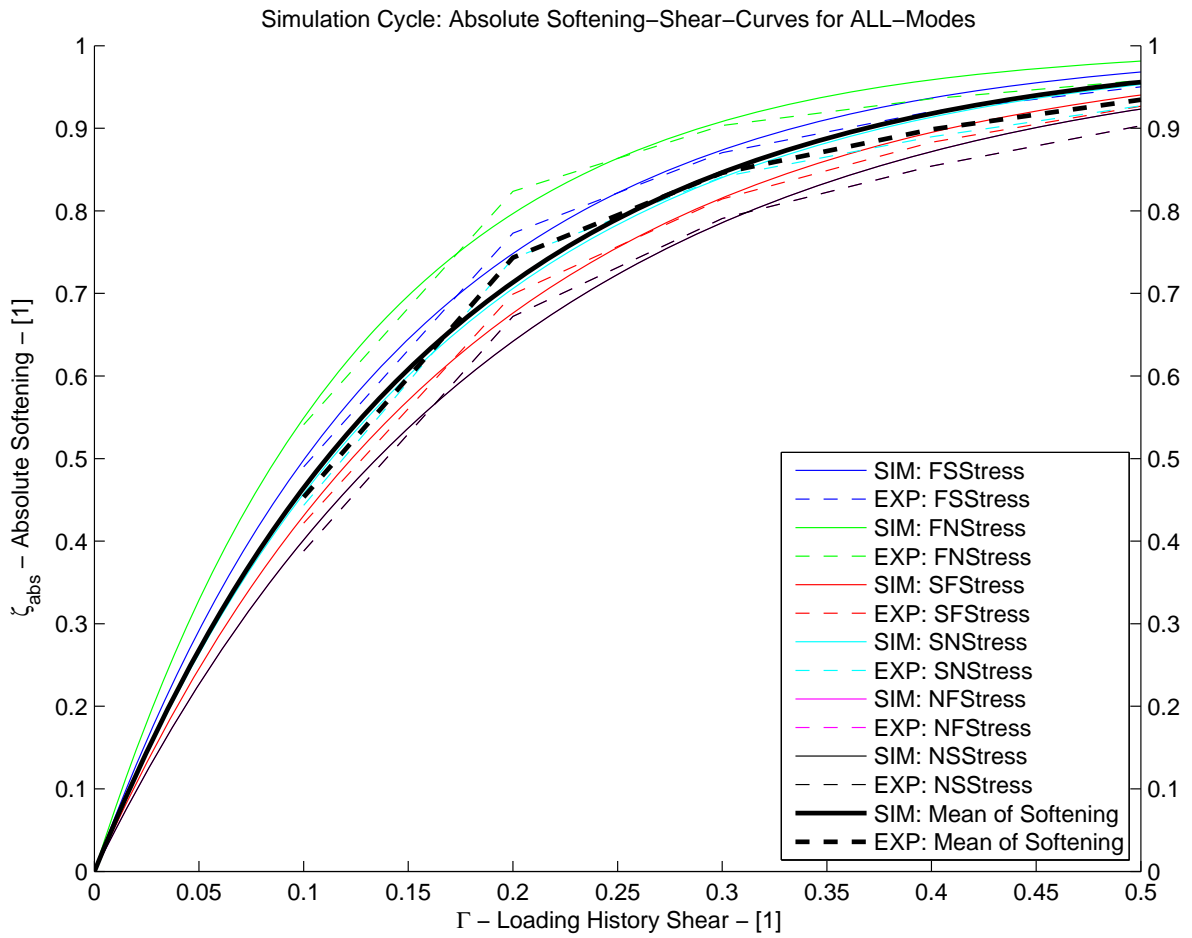
Figure 4.31.: Absolute softening for [FS-FN/SF-SN/NF-NS]-modes (NF and NS are congruent).

4.5. Using Triaxial Data for Simulating Biaxial Behavior

By now, we discussed results from analyzing triaxial shear data. The triaxial shearing is characterized by nonlinear hyperelastic elastic stress terms in combination with restructuring and damping effects determining the viscous stress terms.

In biaxial tensile testing the tissue can be equally stretched which theoretically should cause principle stresses only lacking of shear stresses when the main loading directions are oriented in parallel to the main and cross fiber directions. Recollecting the information about myocardium from the previous sections sliding of sheets should be prevented for biaxial tensile testing as we assume homogeneous application of stretch in both directions. Hence, the underlying mechanics should be a composition of hyperelasticity combined with damping effects only.

The deformation gradient $\mathbf{F}$ for equally applied stretch λ is obtain through

$$\mathbf{F} = \begin{pmatrix} \lambda & 0 & 0 \\ 0 & \lambda & 0 \\ 0 & 0 & \frac{1}{\lambda^2} \end{pmatrix} . \tag{4.4}$$

Using the 'KAPPA' in combination with the 'SIMPLE-DAMPING' model we can derive the main-fiber σ_{ff} and cross-fiber σ_{ss} stress vectors. As we use the parameters from Tables 4.5 and 4.8, we need to refer to the original fiber stretch. The relationship between simple shear γ and corresponding stretch λ is given with

$$\lambda = \sqrt{1 + \gamma^2} . \tag{4.5}$$

Finally, we need to reduce the damping effect to the matrix compound only as both fibers and sheets are separated and elongated along their main axis by not moved relatively to each other. Therefore, we set $\mu_f^{(D)} = \mu_s^{(D)} = \mu_{fs}^{(D)} = 0$. Figure 4.32(a) is showing the loading pattern for cosinusoidal applied shear and the resulting stretch pattern for the biaxial simulation. Finally, the resulting biaxial simulation is shown in Figs. 4.32(b)–4.32(f).

The resulting biaxial curves are similar to those provided in the literature [12, 41]. This proves that myocardium shows light damping effects during tensile testing. In contrast, there are no restructuring effects present as long as no shear is applied. Therefore, it seems that sheet sliding is an effect dominantly observed during filling and ejection phases of the cycle of the heart.
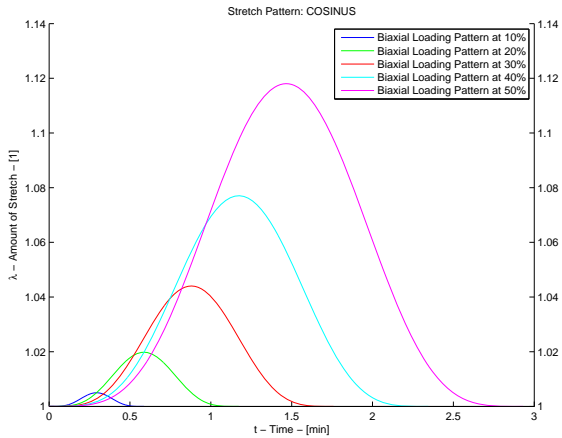
(a) Stretch pattern for the biaxial simulation.
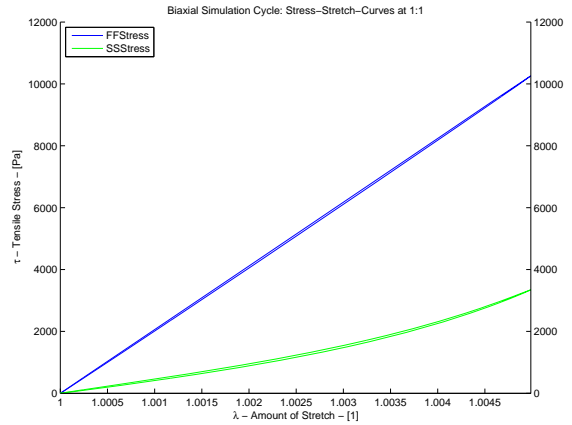
(b) Biaxial simulation using parameters from fit of $\gamma = 0.1$.
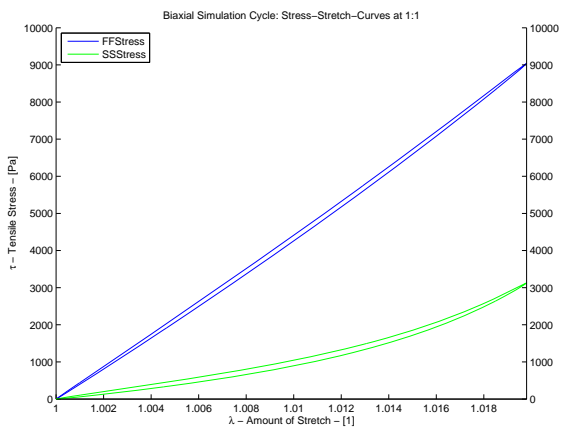
(c) Biaxial simulation using parameters from fit of $\gamma = 0.2$.
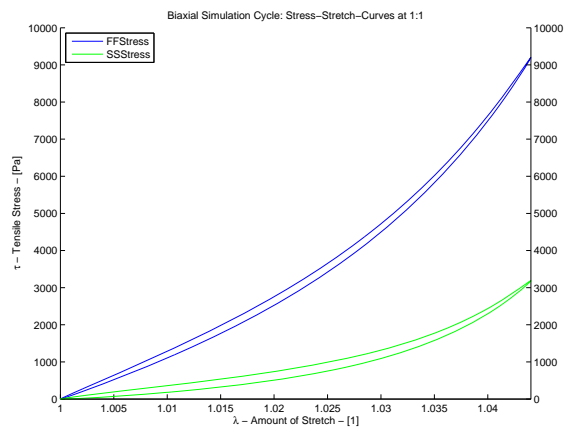
(d) Biaxial simulation using parameters from fit of $\gamma = 0.3$.
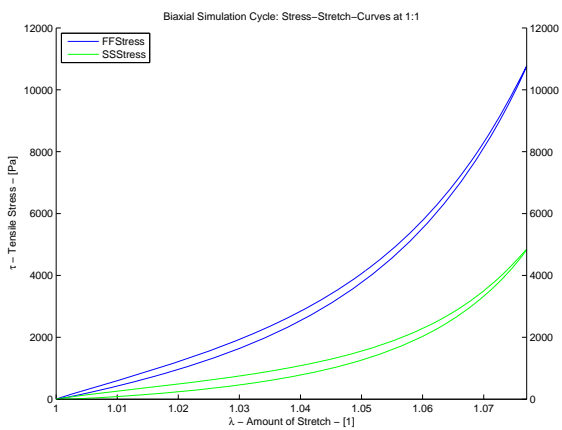
(e) Biaxial simulation using parameters from fit of $\gamma = 0.4$.
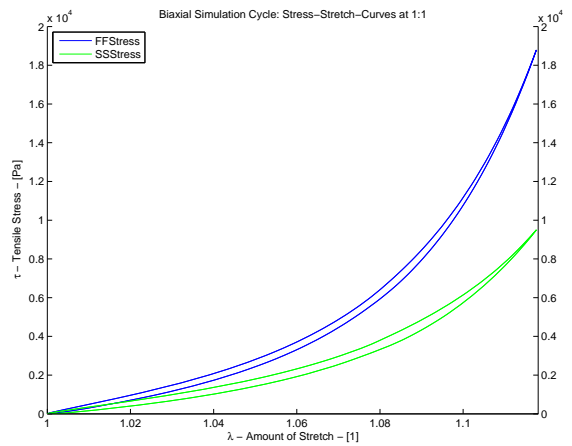
(f) Biaxial simulation using parameters from fit of $\gamma = 0.5$.

Figure 4.32.: Biaxial simulation for different loading stretches.

5. Discussion

5.1. General Findings and Myocardial Vitality

The human ventricular wall mechanics show several special findings. During the last couple of years several tests have proved that myocardium shows hysteresis during shear loading [9, 13, 35, 54]. First tests without usage of BDM proved that activation of specimens due to cutting injury create stiffer and higher hysteresis than inactivated tissue does. As we focus on modeling passive myocardial tissue and the fact that activated myocardial muscle tissue can hardly be kept under repeatedly constant experimental conditions, BDM usage is obligatory for data redundancy. A histological diagnose of myocardium indicates that a series of structural elements and their interconnection give myocardial tissue its special biomechanical properties. In short, all known characteristics are listed in Table 5.1 including their simplifications for modeling.

Elasticity. Based on these model simplifications a list of proposed models have been presented in Sec. 1.3. In summary, the myocardium shows hysteresis at all times even for quasistatic tests. Experiments held under dry conditions also proved this thesis true and therefore hysteresis does not exclusively arise from a fluid flow phase, although the water content in the heart consumes about eighty percent of the total volume which hardly can permeate leading to incompressibility [59]. Hence, the conducted experimental stress curves have been decoupled into an elastic and an inelastic/viscoelastic stress part. The elastic data has been modeled with known models from Holzapfel et al. [25] and Eriksson et al. [15]. Data analysis of parameters proved that the human heart has two main load carrying elements being fibers and sheets. Fibers are the stiffest compound within the human heart and about 1.2 to 1.5 times stiffer than sheet structures (compare stiffness parameters in Table 4.4).

Table 5.1.: Biomechanical characteristics of myocardium (see [25, 17, 27, 43, 46, 55]).

Ideally	Structural Element	Model Simplification
Anisotropy	Matrix, Fiber, Sheet, Coupling [5, 46]	Orthotropy
Inhomogeneity	Endo-/Myo-/Epicardium, Collagen	Homogeneous
Compressibility	H_2O [43], Low Permeability	Incompressibility [59]
Nonlinearity	Reorientation and Reformation [18]	Exponential
Multiphasic	Solid, Fluid, Physicochemical [43, 46]	Solid

Dispersion. In addition, including dispersion to the perfectly aligned model gives even more information about structural components but does not improve modeling confidence as function morphology remains unchanged. Higher dispersion may arise from injury or disease [6, 15, 49] and cause fiber and sheet stiffness to be increased but matrix and coupling stiffness to be decreased.

Softening. Furthermore, softening has been established through an reduction term for the elastic strain-energy function in order to implement strain-softening of myocardial tissue. For sake of simplification the softening has been made generally identical for all loading modes although this might be a shortcoming when comparing softening terms in Table 4.11. FS, FN, SF and SN-modes have approximately identical softening parameters whereas NF and NS modes show lower affection to softening. Thus, it is assumed that softening arises from fiber and sheets softening and not directly on complete myocardial softening of interconnections and matrix compounds. This has already been postulated by Emery et al. [11] and may be substantiated within the scope of this thesis. Furthermore, softening influences also nonlinearity behavior of tissue as the initial decrease of stiffness is in some way compensated by higher nonlinearity. For higher amounts of shear $\hat{\gamma} > 0.3$ stiffness and nonlinearity of tissue decrease simultaneously possibly indicating the beginning of irreversible tissue damage.

Note. Softening is a reversible process whereas damaging is irreversible induced by rupture of perimysial fibers and coupling destruction [11].

Viscoelasticity. In addition, the viscoelastic/inelastic stress response has been modeled by introduction of time pseudo-invariants and a postulate on how to include dissipation in modeling viscous stress responses. The key for doing so is to reduce complexity of the viscoelastic response problem to the periodic solution range and disregard transient effects. As every test cycle has ongoing preceding preconditioning cycles (at least two) and that experiments are held under quasistatic conditions, the transient effects are negligible. Although, this might be a shortcoming of the proposed model. The developed model is capable of describing a couple of interesting effects happening within myocardial tissue during shear loading. These effects are stated to be 'damping' and 'restructuring' effects. Damping describes how myocardial tissue tries to limit circumferential deformation for higher rates of shear which is favorable as the fast contraction of the heart shall be as effective as possible with maximum radial contraction. Restructuring effects occur due to circumferential sliding of sheets and reorientation of fibers after a couple of identical loadings. Interestingly, restructuring effects also show a diminishing trend for higher shear peaks whereas damping effects stay mostly constant throughout different loading peaks, directions and components of tissue.

In summary, the myocardial vitality seems to be dependent on stiffness, nonlinearity, dispersion, damping and restructuring viscosity of tissue besides geometry, wall thickness and composition. Ashikaga et al. [1] have demonstrated how abnormal shearing of myolaminar sheets influence relaxation behavior of hypertrophic myocardium. It has been reported that filling, contraction and exhausting phases are not significantly affected by

hypertrophy. In contrast, hypertrophic myocardium seem to show elongated phases of diastolic isovolumetric relaxation. In addition, sheet shear is drastically increased due to hypertrophy [1]. This proves the importance of simple shear test on myocardial tissue as it is a marker for myocardial isovolumetric shear stresses during contraction and ejection.

Finally, the presented models and parameter estimations are useful for application in finite element modeling (FEM). FEM analysis requires exact constitutive models on the one hand and precise geometrical models on the other. Pravdin et al. [44] presents approaches for modeling anisotropy, sheet layers and fiber reorientation throughout the ventricle wall. The combination of present 3-D magnetic resonance imaging (MRI), mapped FEM-models and constitutive models may be the aim of automated non-invasive screening of ventricular vitality.

High vitality of myocardium may be linked with

- low stiffness and high nonlinearity (i.e. efficient adaption),
- low restructuring viscosity and, therefore, easy sliding of sheets,
- low fiber and sheet dispersions (in and out of plane),
- reversible low softening parameter,

which eventually leads to lower shear stresses and, therefore, facilitated relative movement of sheets during isovolumetric phases. Thus, we postulate that hypertrophy increases shear and relaxation times which may be attributed to higher shear stresses caused by higher dispersion and stiffness of fibers and sheets.

5.2. Possible Improvements on Testing

During analysis of data a series of heart specimen test could not be used due to missing data, failures of tissues or difficulties for determining orientation of fibers and sheets as well as machine calibration errors. In total, 32 hearts have been investigated of which six have not been inactivated and, thus, being useless for passive myocardial data analysis. In fact, only eleven out of 37 BDM-heart specimens could be used for data analysis. The remaining 26 samples showed incorrect data , i.e. NF/NS stresses have been several times higher than FS/FN or SF/SN stresses, partial splice rupture or errors in machine calibration. Furthermore, imperfections of sample cubes lead to extreme forms of skew hysteresis curves causing initial prestretch and strong directional dependencies. Therefore, a couple of improvements on testing and possible pitfalls are summarized in Table 5.2.

Table 5.2.: Suggested improvements on triaxial shear testing.

Pitfall	Problem	Suggested Improvement
Cube geometry	Imperfection causing directional dependencies	Machine controlled cutting or using cutting masks
Glue positioning	Glue amount, connection of glue increasing stiffness	Check for lateral flow of glue after mounting
Fiber direction	Directional misalignment	Position markers or add comments in documentation
Cube size	e.g. ± 0.1mm/5mm $= \pm 10\%$ error in amount of shear	Examine cube size precisely, use cutting masks
Rate of shear	Changing rate of shear because of constant velocity approach	Constant rate of shear approach for independence of geometry

5.3. Conclusion

Conclusions. Summed up, eleven hearts have been analyzed in detail. All in all, 278 experiments were used for data fitting of elastic and viscoelastic/inelastic models. Myocardium shows strong anisotropic and nonlinear behavior which is history dependent causing softening. Elastic and viscous stress terms have been decoupled. It is shown that mean peaks of elastic stress increase with higher amounts of peak shear whereas peaks of viscous stress terms remain nearly unaffected by higher peak shear. Structural discrimination proves that matrix and coupling effects are nearly untouched by softening whereas sheet and fiber stiffnesses decrease significantly. Furthermore, a new approach for modeling has been presented by using not only energetic terms but also an dissipative terms. Thus, the viscous stress terms can be described by an history dependent energetic term describing the restructuring in tissue and an dissipative term describing the damping in tissue. The restructuring actually considers a change of referential configuration which has been modeled via history variables. Restructuring reduces with increased loading history whereas damping remains relatively unchanged. Finally, softening effects are present in myocardium in passive testing conditions. The relative softening effect is reported being approximately 51.41% of reduction of tissue strength in terms of stiffness for the first to second loading cycle. Consequent loading cycles show reduced relative softening with a slight increase for the last cycle $0.4 \to 0.5$. Notably, NF/NS-softening is lower than for all other loading modes may indicating that softening arises from fiber and sheet softening mainly.

Eventually, we could reproduce 99.82% of the dispersed elastic and 94.31% of the viscous experimental data including 95.6% of absolute softening at $\hat{\gamma} = 0.5$.

Limitations. The fundamental assumptions on modeling are that myocardium is incompressible and that quasistatic loading conditions lead to periodically redundant shear curves. Thus, all proposed models lack the effects of transient processes like stress relaxation or creeping in tissue which may be a shortcoming of the viscoelastic/inelastic

models. Furthermore, determination of fiber directions in tissue is a hard task precisely because fibers show dispersion on the one hand and may have curly structure on the other. Thus, residual stresses may arise from structural differences at different locations that neither have been considered. Finally, the number of analyzed hearts is little which may cause bias and in addition sometimes determination of fibers seemed incorrect. Therefore, loading mode switching has been necessary to fulfill Dokos theorem.

Bibliography

[1] H. Ashikaga, J.W. Covell, and J.H. Omens. Diastolic dysfunction in volume-overload hypertrophy is associated with abnormal shearing of myolaminar sheets. *Am. J. Physiol. Heart Circ. Physiol.*, 288:2603–2610, 2005.

[2] Statistik Austria. Todesursachenstatistik. `http://www.statistik.at/web_de/statistiken/gesundheit/todesursachen/todesursachen_im_ueberblick/index.html`, June 03rd, 2014.

[3] K.D. Costa, J.W. Holmes, and A.D. Mcculloch. Modelling cardiac mechanical properties in three dimensions. *Phil. Trans. R. Soc. Lond. A*, 359:1233–1250, 2001.

[4] K.D. Costa, P.J. Hunter, J.S. Wayne, L.K. Waldman, J.M. Guccione, and A.D. McCulloch. A three-dimensional finite element method for large elastic deformations of ventricular myocardium, part ii: prolate spheroidal coordinates. *J. Biomech. Eng.*, 118:464–472, 1996.

[5] K.D. Costa, Y. Takayama, A.D. McCulloch, and J.W. Covell. Laminar fiber architecture and three-dimensional systolic mechanics in canine ventricular myocardium. *Am. J. Physiol.*, 276:595–607, 1999.

[6] J.W. Covell. Tissue structure and ventricular wall mechanics. *Circulation*, 118:699–701, 2008.

[7] L.L. Demer and F.C.P. Yin. Passive biaxial mechanical properties of isolated canine myocardium. *J. Physiol.*, 339:615–630, 1983.

[8] H. Demiray. Stresses in ventricular wall. *J. Appl. Mech.*, 98:194–197, 1976.

[9] S. Dokos, B.H. Smaill, A.A. Young, and I.J. LeGrice. Shear properties of passive ventricular myocardium. *Am. J. Physiol. Heart Circ. Physiol.*, 283:2650–2659, 2002.

[10] J.P. Ebus and G.J. Stienen. Effects of 2,3-butanedione monoxime on cross-bridge kinetics in rat cardiac muscle. *Eur. J. Physiol.*, 432:921–929, 1996.

[11] J.L. Emery, J.H Omens, O.A. Mathieu-Costello, and A.D. McCulloch. Structural mechanisms of acute ventricular strain softening. *Int. J. Cardiovasc. Med. Sci.*, 1:241–250, 1998.

[12] J.L. Emery, J.H. Omens, and A.D. McCulloch. Biaxial mechanics of the passively overstretched left ventricle. *Am. J. Physiol.*, 272:2299–2305, 1997.

[13] T.S.E. Eriksson. *Cardiovascular Mechanics: The Biomechanics of Arteries and the Human Heart.* PhD Thesis, Graz University of Technology, 2012.

[14] T.S.E. Eriksson, A.J. Prassl, G. Plank, and G.A. Holzapfel. Influence of myocardial fiber/sheet orientations on left ventricular mechanical contraction. *Math. Mech. Solids*, 18:592–606, 2013.

[15] T.S.E. Eriksson, A.J. Prassl, G. Plank, and G.A. Holzapfel. Modeling the dispersion in electro-mechanically coupled myocardium. *Int. J. Numer. Meth. Biomed. Engng.*, 29:1267–1284, 2013.

[16] European Comission Eurostat. Causes of death statistics (hlth_cd_asdr). `http://epp.eurostat.ec.europa.eu/statistics_explained/index.php/Causes_of_death_statistics`, June 10th, 2014.

[17] G.M. Fomovsky, S. Thomopoulos, and J.W. Holmes. Contribution of extracellular matrix to the mechanical properties of the heart. *J. Mol. Cell. Cardiol.*, 48:490–496, 2010.

[18] Y.C. Fung. Elasticity of soft tissues in simple elongation. *Am. J. Physiol.*, 213:1532–1544, 1967.

[19] T.C. Gasser and G.A. Holzapfel. A numerical framework to model 3-d fracture in bone tissue with application to failure of the proximal femur. In A. Combescure, R. de Borst, and T. Belytschko, editors, *Discretization Methods for Evolving Discontinuities*, pages 199–211. Springer, Dordrecht, The Netherlands, 2007.

[20] T.C. Gasser, R.W. Ogden, and G.A. Holzapfel. Hyperelastic modelling of arterial layers with distributed collagen fibre orientations. *J. R. Soc. Interface*, 3:15–35, 2006.

[21] J.M. Guccione, A.D. McCulloch, and L.K. Waldman. Passive material properties of intact ventricular myocardium determined from a cylindrical model. *J. Biomech. Eng.*, 113:42–55, 1991.

[22] W.C. Hayes and L. F. Mochros. Viscoelastic properties of human articular cartilage. *Journal of Applied Physiology*, 31:562–568, 1971.

[23] G.A. Holzapfel. *Nonlinear Solid Mechanics: A Continuum Approach for Engineering.* John Wiley & Sons Ltd., 2000.

[24] G.A. Holzapfel and T.C. Gasser. A viscoelastic model for fiber-reinforced composites at finite strains: Continuum basis, computational aspects and applications. *Comput. Methods Appl. Mech. Engrg.*, 190:4379–4403, 2001.

[25] G.A. Holzapfel and R.W. Ogden. Constitutive modelling of passive myocardium: a structurally based framework for material characterization. *Phil. Trans. R. Soc. A*, 367:3445–3475, 2009.

[26] G.A. Holzapfel, J. Tong, and T.U. Cohnert. Biomechanical behavior of diseased arteries: tissue dissection, gender difference and mass fraction in abdominal aortic aneurysms. In N. Chakf, B. Durand, and W. Meichelboeck, editors, *ESVB 2013 New Endovascular Technologies From Bench Test to Clinical Practice*, chapter 31, pages 299–316. Geprovas, Strasbourg, France, 2013.

[27] J.D. Humphrey. *Cardiovascular Solid Mechanics.* Springer, 2002.

[28] J.D. Humphrey, R.K. Strumpf, and F.C.P. Yin. Determination of constitutive relation for passive myocardium. *J. Biomech. Eng.*, 112:333–339, 1990.

[29] J.D. Humphrey and F.C.P. Yin. On constitutive relations and finite deformations of passive cardiac tissue, part i: a pseudo-strain energy function. *J. Biomech. Eng.*, 109:298–304, 1987.

[30] J.D. Humphrey and F.C.P. Yin. Biaxial mechanical behavior of excised epicardium. *J. Biomech. Eng.*, 110:349–351, 1988.

[31] P.J. Hunter, M.P. Nash, and G.B. Sands. Computational electromechanics of the heart. In A.V. Panfilov and A.V. Holden, editors, *Computational Biology of the Heart*, pages 345–407. Chichester, Wiley, UK, 1997.

[32] J.M. Huyghe, D.H. van Campen, T. Arts, and R.M. Heethaar. The constitutive behaviour of passive heart muscle tissue. a quasi-linear viscoelastic formulation. *J. Biomech.*, 24:841–849, 1991.

[33] P.A. Iaizzo. *Handbook of Cardiac Anatomy, Physiology, and Devices.* Springer, New York, USA, 2 edition, 2009.

[34] W.J. Karlon, J.W. Covell, A.D. McCulloch, J.J. Hunter, and J.H. Omens. Automated measurement of myofiber disarray in transgenic mice with ventricular expression of ras. *Anat. Rec.*, 252:612–625, 1998.

[35] M. Kutschera. Shear properties of passive ventricular porcine and human myocardium. Master's thesis, Graz University of Technology, 2012.

[36] I.J. LeGrice, Y. Takayama, and J.W. Covell. Transverse shear along myocardial cleavage planes provides a mechanism for normal systolic wall thickening. *Circ. Res.*, 77:182–193, 1995.

[37] Z. Liu and K. Yeung. The preconditioning and stress relaxation of skin tissue. *J. Biomech. Pharm. Engng.*, 2:22–28, 2008.

[38] H. Lodish, A. Berk, P. Matsudaira, C.A. Kaiser, M. Krieger, M.P. Scott, S.L. Zipursky, and J. Darnell. *Molecular Cell Biology.* W.H. Freeman and Company, New York, 2003.

[39] L.A. Mulieri, G. Hasenfuss, F. Ittleman, E.M. Blanchard, and N.R. Alpert. Protection of human left ventricular myocardium from cutting injury with 2,3-butanedione monoxime. *Circ. Res.*, 65:1441–1449, 1989.

[40] E.M. Ostap. 2,3-butanedione monoxime (bdm) as a myosin inhibitor. *J. Muscle Res. Cell. Motil.*, 23:305–308, 2002.

[41] I. Peterson and R. Donald. Resting myocardial properties. In D.R. Peterson and J.D. Bronzino, editors, *Biomechanics: Principles and Applications*, pages 8–15–8–18. CRC Press Taylor & Francis Group, 2 edition, 2008.

[42] D.M. Pierce, T. Ricken, and G.A. Holzapfel. Modeling sample/patient-specific structural and diffusional responses of cartilage using dt-mri. *International Journal for Numerical Methods in Biomedical Engineering*, 2012.

[43] G. Pogtsa, M.Z. Koltai, and G. Grsz. The role of the myocardial water content in heart function. *Acta Physio. Acad. Sci. Hung.*, 59:305–309, 1982.

[44] S.F. Pravdin, V.I. Berdyshev, A.V. Panfilov, L.B. Katsnelson, O. Solovyova, and V.S. Markhasin. Mathematical model of the anatomy and fibre orientation field of the left ventricle of the heart. *Biomed. Engng. Online*, 12:54, 2013.

[45] A.J. Reinisch. Constitutive modeling of collagen fiber dispersion with application to the arterial wall. Master's thesis, Graz University of Technology, 2013.

[46] D. Rohmer, A. Sitek, and G.T. Gullberg. Reconstruction and visualization of fiber and laminar structure in the normal human heart from ex vivo diffusion tensor magnetic resonance imaging (dtmri) data. *Invest. Radiol.*, 42:777–789, 2007.

[47] F.B. Sachse, G. Seemann, K. Ghaisaowong, and D. Wei. Quantitative reconstruction of cardiac electromechanics in human myocardium: assembly of electrophysiological and tension generation models. *J. Cardiovasc. Electrophysiol.*, 14:210–218, 2003.

[48] H. Schmid, M.P. Nash, A.A. Young, and P.J. Hunter. Myocardial material parameter estimation - a comparative study for simple shear. *J. Biomech. Eng.*, 128:742–750, 2006.

[49] A.J. Schriefl, H. Wolinski, S.D. Kohlwein, and G.A. Holzapfel, editors. *Structural differences in collagen morphologies between healthy and AAA tissues*, The 4th Canadian Conference on Nonlinear Solid Mechanics (CanCNSM 2013), 2013.

[50] G. Seemann, F.B. Sachse, D.L. Wei, and O. Dössel. Quantitative reconstruction of cardiac electromechanics in human myocardium: regional heterogeneity. *J. Cardiovasc. Electrophysiol.*, 14:219–228, 2003.

[51] B. Smaill and P. Hunter. Structure and function of the diastolic heart: material properties of passive myocardium. In L. Glass, P. Hunter, and A. McCulloch, editors, *Theory of Heart*, pages 1–29. Springer, New York, USA, 1991.

[52] Y. Soeno, Y Shimada, and T. Obinata. Bdm (2,3-butanedione monoxime), an inhibitor of myosin-actin interaction, suppresses myofibrillogenesis in skeletal muscle cells in culture. *Cell. Tissue Res.*, 295:307–316, 1999.

[53] G. Sommer and G.A. Holzapfel. Constitutive modeling of the biaxial mechanical response of intact and layer-dissected human carotid arteries. *J. Mech. Behav. Biomed. Mater.*, 5:116–128, 2012.

[54] G. Sommer, M. Schwarz, M. Kutschera, R. Kresnik, A. Schriefl, H. Wolinski, S. Kohlwein, P. Regitnig, and G.A. Holzapfel. Biomechanical properties of the human ventricular myocardium. *Biomed. Tech.*, 58, 2013.

[55] H.M. Spotnitz, W.D. Spotnitz, T.S. Cottrell, D. Spiro, and E.H. Sonnenblick. Cellular basis for volume-related wall thickness changes in the rat left ventricle. *J. Mol. Cell. Cardiol.*, 6:317–331, 1974.

[56] D.D.Jr. Streeter, H.M. Spotnitz, D.P. Patel, J.Jr. Ross, and E.H. Sonnenblick. Fiber orientation in the canine left ventricle during diastole and systole. *Circ. Res.*, 24:339–347, 1969.

[57] J.M. Ticar. The human myocardium: Determination of its muscle fiber and sheet orientations. Master's thesis, Graz University of Technology, 2014.

[58] C. Truesdell. *The Elements of Continuum Mechanics.* Springer, New York, NY, 1966.

[59] K. Tsuiki and E.L. Ritman. Direct evidence that left ventricular myocardium is incompressible throughout systole and diastole. *Tohoku J. Exp. Med.*, 132:119–120, 1980.

[60] K.H.T. Tusscher, D. Noble, P.J. Noble, and A.V. Panfilov. A model for human ventricular tissue. *Am. J. Physiol. Heart Circ. Physiol.*, 286:1573–1589, 2004.

[61] Y.J. Zeng, Y.H. Liu, C.Q. Xu, X.H. Xu, H. Xu, and G.C. Sun. Biomechanical properties of skin in vitro for different expansion methods. *Clin. Biomech.*, 19:853–857, 2004.

A. Matlab Output

A.1. Function Output of 'readTraData()'

```
1  d = readTraData('...\HH10_HH7\..._HH10_LV_FN_FS..._50p... .tra',opts)
2  Selected file: "07-05-2012_HH10_LV_FN_FS_cardiopleg_patchwork_50p_mitte_mitte1"
3  Opening file... Done!
4  Checking loading type... Done!
5  Checking file... Header found!
6  Setting data and correcting units... Done!
7  [INFO]: Found 12 header lines
8  Searching column data... Done!
9  [INFO]: Found 5 columns
10  "pruefzeit" "shear displace" "shear stress" "shear displace" "shear stress"
11 Searching shear-x zero-crossings... Done!
12 [INFO]: Found zero crossings with confidence: 98.88%
13 Searching shear-x peaks... Done!
14 [WARNING]: Set and conducted shear-x differ by max: 0.04%
15 Searching relaxation segments for x-data... Done!
16 [INFO]: Relaxation signal loss due to smoothing: 0.19%
17 Searching shear-y zero-crossings... Done!
18 [INFO]: Found zero crossings with confidence: 98.88%
19 Searching shear-y peaks... Done!
20 [WARNING]: Set and conducted shear-y differ by max: 0.04%
21 Searching relaxation segments for y-data... Done!
22 [INFO]: Relaxation signal loss due to smoothing: 0.10%
23 Smoothing, applying offset and overwriting data-x... Done!
24 [INFO]: Data loss due to smoothing: 0.46%
25 Smoothing, applying offset and overwriting data-y... Done!
26 [INFO]: Data loss due to smoothing: 0.83%
27 Finding data-x elastic term...
28 [INFO]: Symmetry rating: 99.10%
29 Done!
30 Finding data-y elastic term...
31 [INFO]: Symmetry rating: 60.52%
32 Done!
33 Closing file... Done!
34
35 d =
36
37                        name: [1x62 char]
38                        path: 'DATA\DATA_BDM_SWITCHED\HH10_HH7'
39                loading_mode: 'shearing'
```

```
40                        tissue: 'HH10'
41                      location: 'LV'
42               loading_type_x: 'FN'
43               loading_type_y: 'FS'
44                        height: 0.0050
45                         width: 0.0040
46                 zyklen_main_x: 1
47                 zyklen_main_y: 1
48                  zyklen_pre_x: 2
49                  zyklen_pre_y: 2
50         geschwindigkeit_main: 2
51    geschwindigkeit_step_test: 150
52                      strain_x: 0.5000
53                 strain_x_step: 0.5000
54                      strain_y: 0.5000
55                 strain_y_step: 0.5000
56                          time: [39300x1 double]
57                       shear_x: [39300x1 double]
58                      stress_x: [39300x1 double]
59                       shear_y: [39300x1 double]
60                      stress_y: [39300x1 double]
61                        tcross: [13x1 double]
62                        time_c: [39300x1 double]
63                      zcross_x: [7x1 double]
64                 zcross_x_conf: 0.9888
65                        peak_x: [6x1 double]
66                       relax_x: [1x1 struct]
67                      zcross_y: [7x1 double]
68                 zcross_y_conf: 0.9888
69                        peak_y: [6x1 double]
70                       relax_y: [1x1 struct]
71                        freq_x: 0.0067
72                        freq_y: 0.0067
73                         res_x: 0.0046
74                         res_y: 0.0083
75                     elastic_x: [1x1 struct]
76                       visco_x: [1x1 struct]
77                    selastic_x: [1x1 struct]
78                      svisco_x: []
79                     elastic_y: [1x1 struct]
80                       visco_y: [1x1 struct]
81                    selastic_y: [1x1 struct]
82                      svisco_y: []
83                    lelastic_x: [1x1 struct]
84                    lelastic_y: [1x1 struct]
```

B. Matlab Code Structure

Figure B.1.: Dependency graph.

STATUTORY DECLARATION

I declare that I have authored this thesis independently, that I have not used other than the declared sources / resources, and that I have explicitly marked all material which has been quoted either literally or by content from the used sources.

_____
date

_____
(signature)